DOE Final Technical Report

Award Number: DE-EE0003778

Project Title: TECHBELT ENERGY INNOVATION CENTER

Awardee: YOUNGSTOWN STATE UNIVERSITY

Partners: Tech Belt Energy Innovation Center (TBEIC)

Principle Investigator: Hazel Marie (hmarie@ysu.edu)

Project Period: 10/1/2010 – 12/31/2016

Acknowledgment: "This material is based upon work supported by the U.S. Department of Energy's Office of Energy Efficiency and Renewable Energy (EERE) under Award Number DE-EE0003778."

1. Introduction and Summary

This project consisted of three main components:

1) The primary goal of the project was to renovate and upgrade an existing commercial building to the highest possible environmentally sustainable level for the purpose of creating an energy incubator. This initiative was part of the Infrastructure Technologies Program, through which a sustainable energy demonstration facility was to be created and used as a research and community outreach base for sustainable energy product and process incubation.
2) In addition, fundamental energy related research on wind energy was performed; a shrouded wind turbine on the Youngstown State University campus was commissioned; and educational initiatives were implemented.
3) The project also included an education and outreach component to inform and educate the public in sustainable energy production and career opportunities.

Youngstown State University and the Tech Belt Energy Innovation Center (TBEIC) renovated a 37,000 square foot urban building which is now being used as a research and development hub for the region's energy technology innovation industry. The building houses basic research facilities and business development in an incubator format. In addition, the TBEIC performs community outreach and education initiatives in advanced and sustainable energy. The building is linked to a back warehouse which will eventually be used as a build-out for energy laboratory facilities.

The projects research component investigated shrouded wind turbines, and specifically the "Windcube" which was renamed the "Wind Sphere" during the course of the project. There was a specific focus on the development in the theory of shrouded wind turbines. The goal of this work was to increase the potential efficiency of wind turbines by improving the lift and drag characteristics. The work included computational modeling, scale models and full-sized design and construction of a test turbine. The full-sized turbine was built on the YSU campus as a grid-tie system that supplies the YSU research facility. Electrical power meters and weather monitors were installed to record the power generated and aid in continued study.

In addition, an education/outreach component to help elicit creative engineering and design from amongst area students, faculty, entrepreneurs, and small business in the energy related fields was performed.

2. TechBelt Energy Innovation Center

The City of Warren and the entire Mahoning Valley had experienced significant economic decline and job loss over the decade prior to this Department of Energy (DOE) grant. The establishment of the TechBelt Energy Innovation Center created a model "green" facility which is being used to help catapult the region into a new era of advanced energy research, development, and commercialization, leveraging the technical expertise and resources still prevalent in the region. A renovated facility in Warren, Ohio is the home of the TechBelt Energy Innovation Center, a mixed-use laboratory, meeting space, educational center and business incubator designed to advance and commercialize sustainable energy-related technologies.

2.1. TBEIC Facility Leadership

In order to make the TechBelt Energy Innovation Center (TBEIC) a reality, planning and design for the renovation of a facility was of prime importance. An independent Board was created to support the development of the Center, to raise funds required to match those available from DOE for construction, and ultimately to manage the operations of the Center. Martin Abraham, Provost of Youngstown State University (YSU) sits on this Board as a representative of YSU, and ensures smooth flow of information between YSU and the TBEIC Board. The TBEIC board assembled a Design Committee for the TBEIC building when the commercial building was identified and the acquisition process was underway. The Design Committee produced design guidelines for the renovation of the space. The committee consisted of engineers from NASA, AEP, and First Energy along with representatives from the engineering schools of YSU and Kent State. Members of the Design Committee visited a number of technology business incubators and technology centers and interviewed operators of those facilities to learn from their experiences. Chairing the committee was Dave Nestic, a technology business development consultant with more than 20 years experience with start-up technology companies and technology business incubators. Under Mr. Nestic's leadership the committee developed a set of design guidelines for consideration in renovation of the building to the intended purpose of an energy technology business incubator/accelerator and shared resource technology facility.

Mr. Nestic was later engaged as co-chief executive of TBEIC along with Chris Mather in September of 2011. Both Mr. Nestic and Mr. Mather had previously worked with regional technology venture and economic development organizations, JumpStart and NorTech. Both also had recent experiences with the development of shared resource centers. Upon the hiring of the executive team for TBEIC, it was determined that an owner's agent be selected to help guide the Request For Proposal (RFP) process for the Design-Build bids for building design and

renovation. After obtaining multiple proposals, MS Consultants, a regional engineering and architectural firm, was chosen as owner's agent.

Continuity in leadership has continued as the TBEIC management team is currently managed by Dave Nestic, Regional Chief Executive Officer, Chris Mather, National Initiatives, Ted Theofrastous Chief Legal Counsel, and Board President John Pogue. The management team works closely with the TBEIC Board of Directors, a Technical Advisory Committee, and Steering Committee to create and implement the business strategy for TBEIC.

2.2. Facility Inspection

The building at 125 West Market Street Warren, Trumbull County, Ohio was purchased by the Wean Foundation on behalf of TBEIC, who became the owners for the facility upon release of State funding. A structural inspection was completed in December 2010 and revealed the building to be structurally sound, but in need of a comprehensive renovation to meet use requirements. The plumbing, electrical, HVAC, and hot water systems were all in need of complete rehabilitation in order to make the facility useful. The roof was evaluated and shown to be in need of minor repair, which was completed first in order to retain the integrity of the interior of the facility. A preliminary environmental analysis was also completed and showed no recognized environmental conditions in reference to the property. There was some evidence of asbestos containment within the property, particularly in regard to tiles in certain areas of the building. Thus a more thorough asbestos test was conducted. No other concerns were noted. Based on the analyses completed, it was determined that the facility would meet the requirements of the proposed use. Submitted reports, with accompanying assessment standards where applicable, were as follows:

- Property Condition Assessment (ASTM Standard E2018-08)
- Phase 1 Environmental Site Assessment (ASTM Standard E 1527-05 and in accordance with all applicable state and local laws and regulations)
- Structural Analysis of Existing Conditions (Floor load analysis)
- Asbestos Sampling and Analysis (EPA NESHAP – 40CFR, Part 61)
- Land and Title Survey

2.3. LEED Building Design, Bidding, and Sourcing

Two RFP processes were executed before a Design and Build Team was selected. The first RFP process yielded bids that were too diverse and the TBEIC Board did not have confidence that the lowest bidder was responsive to the design guidelines created by the Design Committee

and published in the RFP. Under advisement of MS Consultants the project was rebid. Working with the TBEIC Chief Executive Dave Nestic, MS Consultants managed the second RFP process that included schematic drawings to which bidders developed their estimates and also focused more on experience with historic tax credit financing which is an important element of the TBEIC funding plan. The second RFP cycle elicited four (4) bids. A review team of five (5) TBIEC board members, two (2) TBEIC executives and the TBEIC general counsel, using a rigorous evaluation scheme, selected Phillips|Sekanick Architects and DeSalvo Construction as the Design and Build Team in August of 2012. This team included a capable and qualified architectural/engineering firm with LEED experience, a construction contractor, and a consulting architectural firm that specializes in historic renovations. Due to the timing of the historic tax credit (HTC) process, it was necessary to focus initial efforts on completion of the State HTC application which was due October 1, 2012. Activity under this task included:

- Meeting with the Ohio Department of Development and teleconference with the State Historic Preservation Office to review the project and the current state of the building
- Numerous meetings with the DB Team to coordinate activity and responsibilities
- Development of conceptual drawings of building layout by the architects and review with TBEIC Chief Executive
- Collection of required support and commitment letters for project and program financing
- Assembly of all application materials and submission to the state office

Thus, the building renovation was conducted in accordance with guidelines approved by the State Historic Preservation Office. In addition, the building design and renovation was done with consideration to LEED standards. In an effort to highlight new energy efficiency products made in Ohio, the Chief Executive of Regional Operations solicited participation by Ohio building products manufacturers in the design phase of the work. This netted many meeting to ensure the intent of the building was preserved. These meeting included, among others:

- Meetings and correspondence with the Ohio State Historic Preservation Office to review the project and plans for renovation.
- Meeting in Columbus with the architect and TBEIC executive to review the Tech Columbus incubator and speak with the operations manager regarding building management experience.
- Meetings with the City of Warren, the Port Authority and One Community regarding siting of a communication center in the TBEIC building. The center would provide the

community with low-cost, broadband connectivity, and would provide TBEIC with hi-speed, broadband connectivity for client and partner communication and research data transfer.

- Development of conceptual drawings of building layout by the architects and review with TBEIC Chief Executive
- Meetings with Design-Build Team members and TBEIC executive for project review and design feedback.
- Ongoing communication with YSU, DOE-EERE and Design-Build Team for NEPA review requirements
- Weekly design review meetings with the Phillips|Sekanick Architects and DeSalvo Construction (Design-Build Team)
- Meeting with Roth Brothers regarding roof replacement contribution and new skylight system developed by Replex Plastics
- Meetings with original Design Committee and Board Members to review building designs and gain feedback.
- Management of documentation requests by State Historical Preservation Office and DOE-EERE for NEPA and project approvals.
- Preparation of project financing documentation.

By the beginning of 2013, the building layout was finalized between the TBEIC and the architects on the Design-Build Team. Figure 1 is the layout of the basement plans. Note that the area in yellow was planned as a basement flex space, the area in turquoise was the planned lavatory area, the dark grey was planned for office space, and the light grey areas was for future expansion. Figure 2 is the layout of the first floor plans. It is important to note that the first floor is the street level. In this figure the area in turquoise was the planned lavatory area, the light orange was the planned shared usage area (conference rooms and demonstration space), and the grey and brown areas were the areas open to the public (reception, cafe, etcetera). Figure 3 is the layout of the mezzanine floor. The area in torquoise was the planned lavatory area and the open grey area was the planned future laboratory area. Figures 4(a) and 4(b) are artistic renderings of the mezzanine level that were passed on to the demolition and renovation company (DeSalvo Construction). Figure 5 is the layout of the second floor plans. All colors were as stated previously except the light grey area near the middle was a planned outdoor courtyard area. Figures 6(a) and 6(b) are again artistic renderings, these of the second floor area that were passed on to DeSalvo Construction.

Figure 1. Original Basement Floor Plans

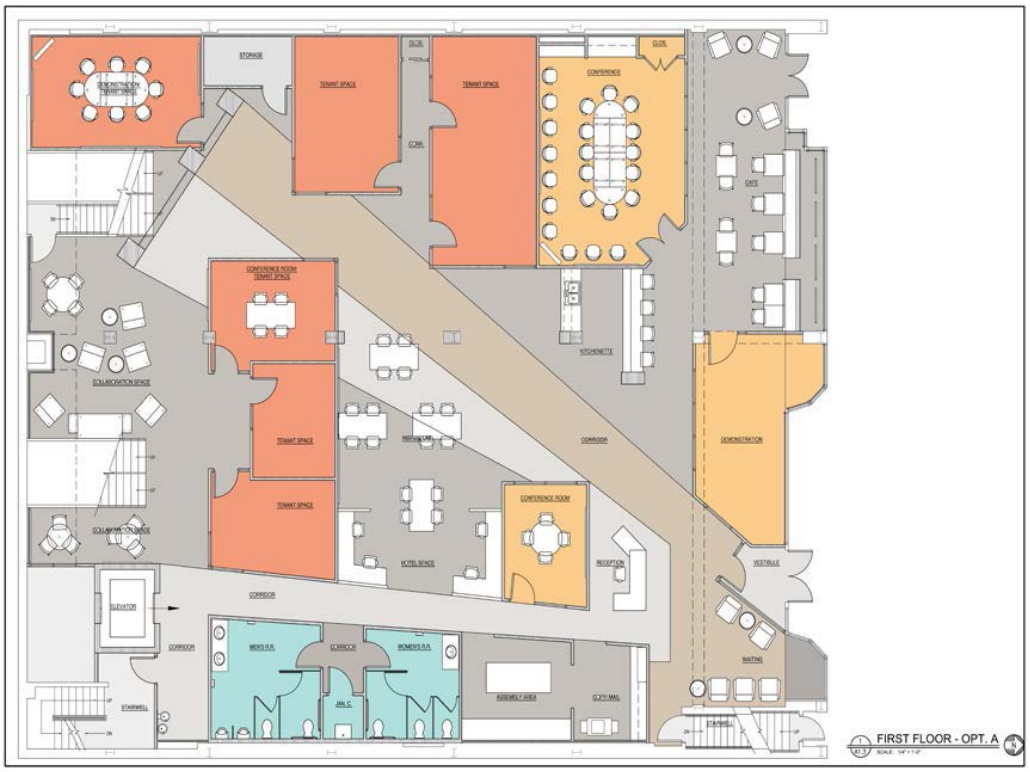

Figure 2. Original First Floor Plans

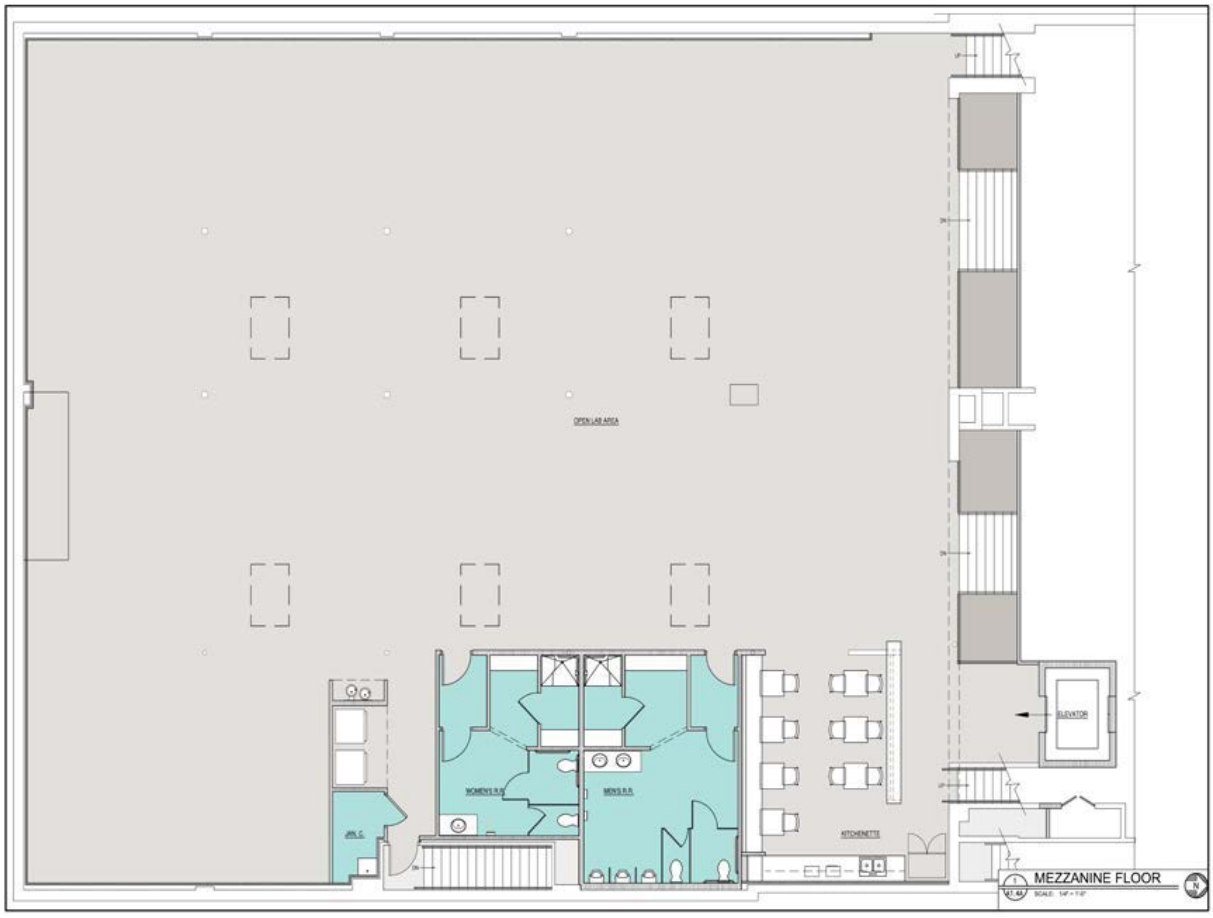

Figure 3. Original Mezzanine Floor Plans

(a) (b)

Figure 4. Artistic Rendering of Mezzanine: (a) from Kitchen Area, (b) from top of West Stairs

Figure 5. Original Second Floor Plans

(a) (b)

Figure 6. Artistic Rendering of 2nd Floor: (a) from Front Hall, (b) from Courtyard

2.4. Facility Renovations

From this point the project moved into engineering and construction drawings in preparation for selective demolition and renovation. With the release of the construction funds by the DOE, attention intensified on the financing close for the bridge loan and investor documentation. A close on the bridge loan occurred in August, 2014 and construction commenced shortly thereafter. Documentation requirements for the investor continued while construction proceeded with a target Certificate of Occupancy by December 31, 2014. By the end of September, demolition was complete, the masonry work for the roof was complete, the elevator shaft masonry, rough frame, HVAC, plumbing and electrical work was underway. The Gantt chart in Figure 7 provides an estimate of construction progress by the end of September 2014. Note that the chart spans from December 2013 to December 2014.

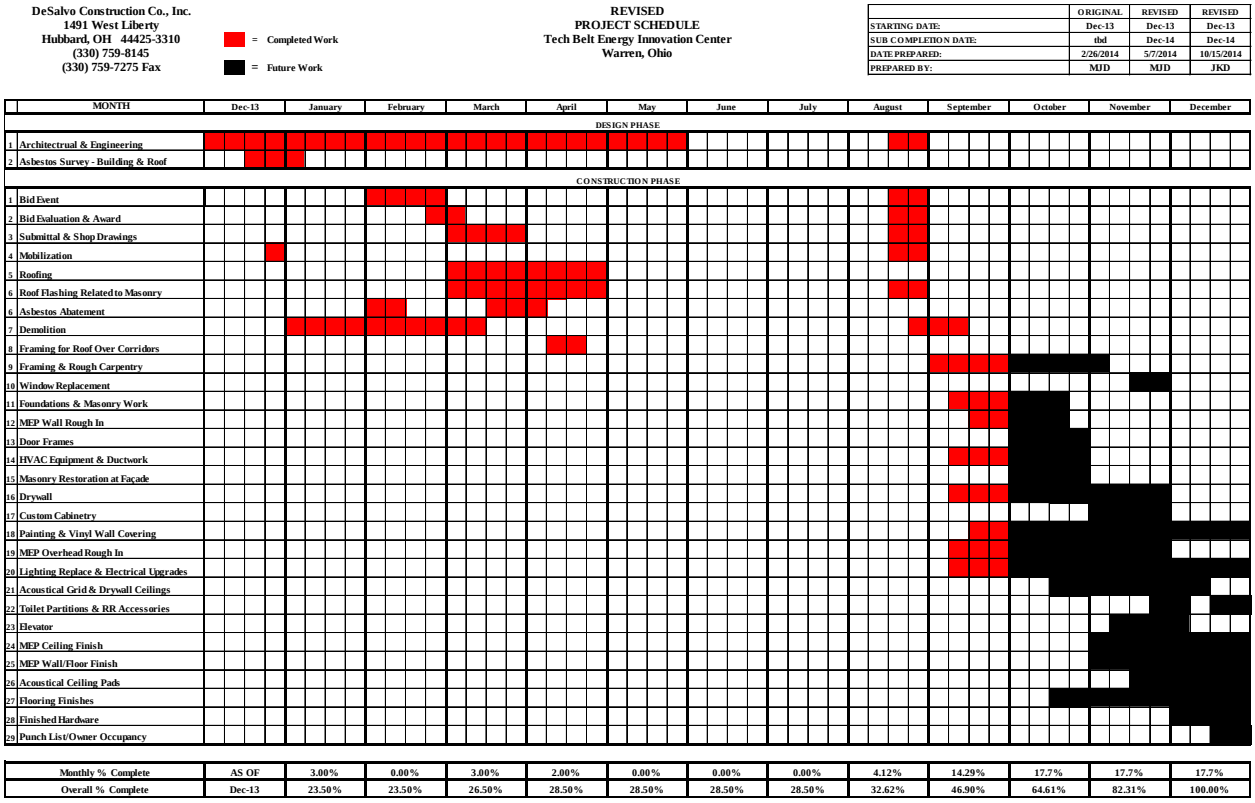

Figure 7. Gantt Chart of Construction from December 2013 to December 2014

In the final calendar quarter of 2014, construction accelerated on the TBEIC facility with a target of obtaining a Certificate of Occupancy by December 31, 2014. Major mechanical, electrical and plumbing work was coordinated throughout the quarter. Interior construction including walls, flooring and plaster work to renovate the historic aspects of the building occurred simultaneously. In the middle of the quarter TBEIC received a generous donation of IT and security infrastructure including CAT6A cable throughout the building, multiple wireless access

points, two IT racks, a video conferencing system, exterior security cameras and secure access entry hardware.

With nearly 40 people on site for much of the quarter, the Certificate of Occupancy was obtained before December 31, 2014. The building was ready to be put into service by the end of the year, with some finishing work left for January and February. Tours were conducted in December 2014 for potential tenants with leases expected to be sign in February 2015.

The following, Figures 8(a)-8(r), are some photos taken of the TBEIC facility during the construction time period of December 2013 to December 2014. The majority are at the end of this time period.

(a) Installation of new arch-top front windows

(b) New fixture in historic block

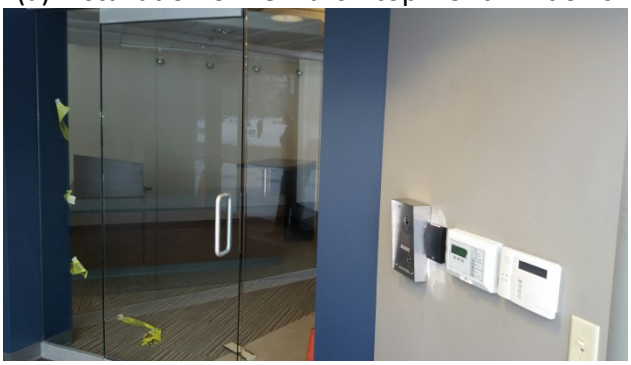

(c) Entry with secure access

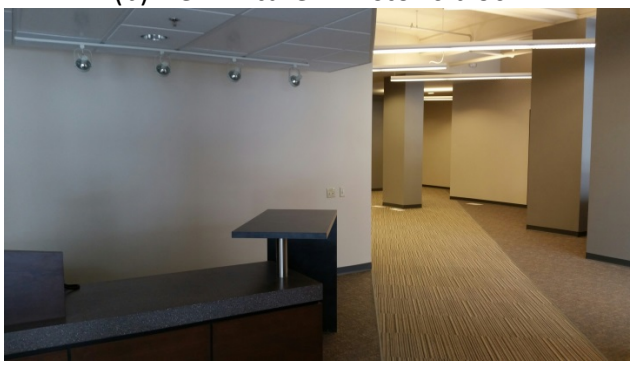

(d) Reception and first floor common area

(e) Demo room center, street level

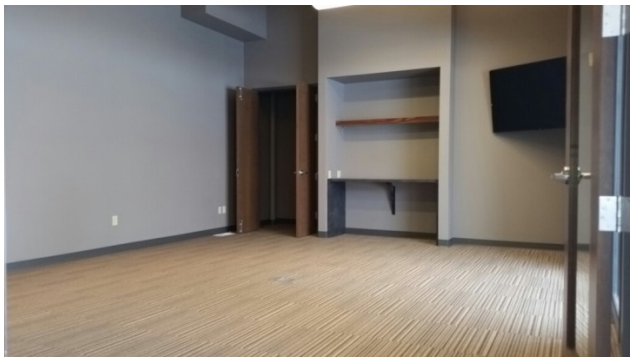

(f) Street level main conference room

(g) View to first floor street entrance

(h) Example of rentable space, street level

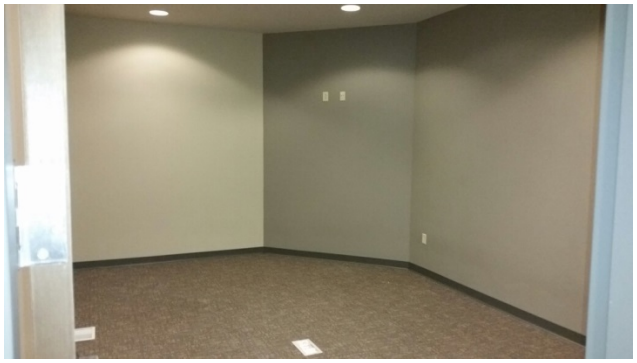

(i) Flex space – conference, rentable or demo

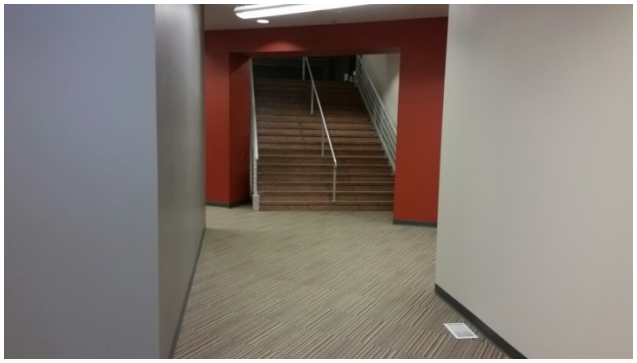

(j) Preserved staircase from street level to mezzanine

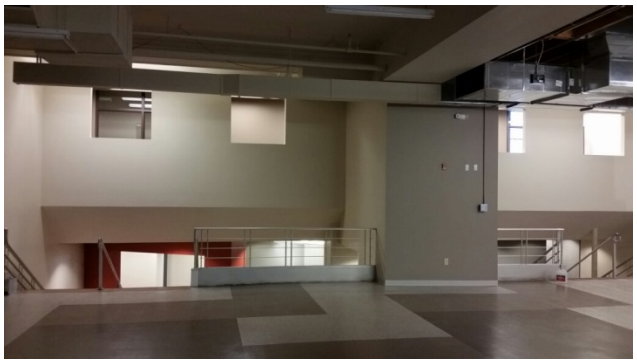

(k) Mezzanine level view of second floor management offices and stairs to street level

(l) Larger mezzanine view, site of future lab

(m) Example of rentable space, second floor

(n) Rental space or classroom, second floor

(o) Executive conference room, second floor

(p) Second floor outdoor future rooftop courtyard

(q) Basement flex space

(r) IT rack and infrastructure (donated)

Figure 8. Renovated Spaces, Ready for Occupancy

As of April 1, 2015 the TBEIC building was complete, two tenants had moved into the building and were actively growing their companies that have five employees. TBEIC also developed the Valley Alliance for Science and Technology program, two meetings had taken place and several partnerships between startups and local manufacturers had begun to develop. With the completed building, TBEIC was poised be able to grow its footprint in Northeast Ohio and to continue to grow its entrepreneurial services. Figures 9-12 show various areas of the first floor, both before and after the renovations.

(a) (b)

Figure 9. Street Front View of TBEIC Facility: (a) before and (b) after Renovation

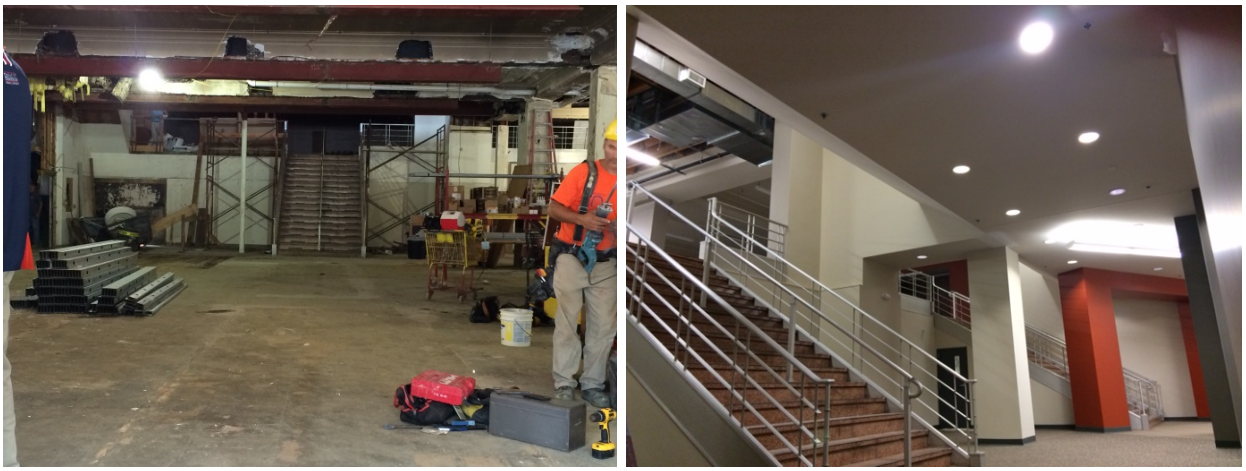

(a) (b)

Figure 10. View of Preserved Staircase: (a) before and (b) after Renovation

(a) (b)

Figure 11. View of Coffee Bar and Public Display Area: (a) before and (b) after Renovation

(a) (b)

Figure 12. View of Reception Area: (a) before and (b) after Renovation

During the third quarter in 2015, TBEIC had gained four tenant companies with an addition two that are actively reviewing the TBEIC Tenant License Agreement. TBEIC was indeed a fully furnished business incubator that has access to furniture and equipment for tenant use. Various shared spaces available to all TBIEC tenants are shown in Figures 13(a) through 13(f).

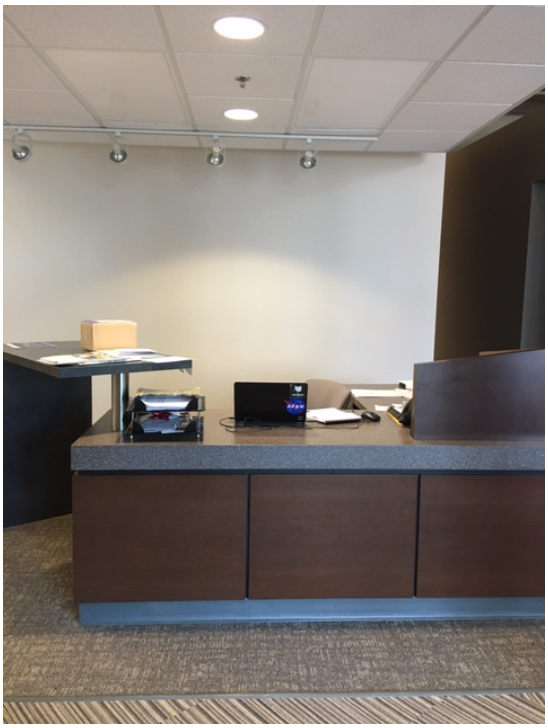

(a) Front Desk managed by TBEIC employee

(b) Waiting room area; plaques listing original founders and donors.

(c) Café Bar

(d) Lunch Area

(e) Fully furnished large conference room with teleconference capabilities

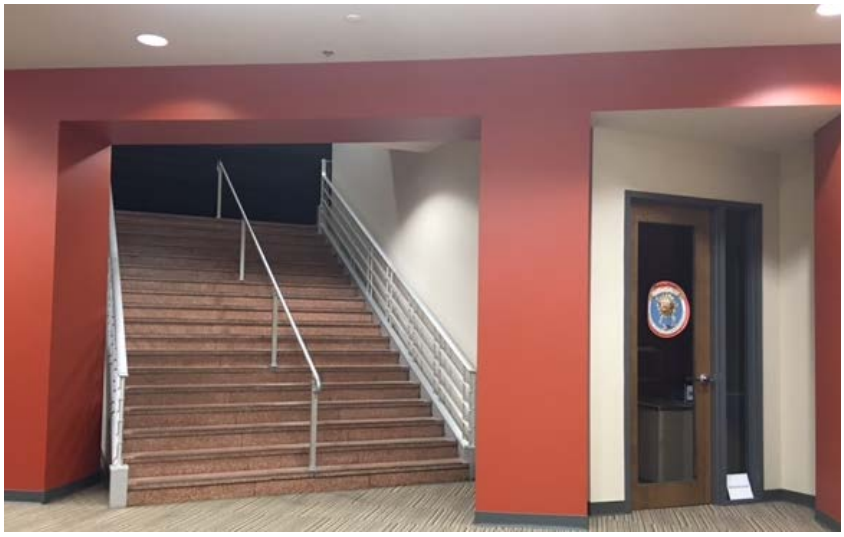

(f) Original staircase of the building that has been renovated, next to an occupied office space

Figure 13. Shared Spaces Available to TBIEC Tenants

Today, TBEIC has been operating nearly two and a half years. The center has worked with more than 100 portfolio companies and has nine tenants so far. Public outreach is a continual process and many entrepreneurial individuals have worked at the incubator on a short term basis. Services offered to the individuals and companies range from business-plan writing to searching for angel investors to venture capital. The incubator also helps with business development and access to testing for their services. These services are meant to address the challenge of working with energy entrepreneurs. Barriers to entry are high because of factors such as the amount of money needed for product development and getting people to try new sources of energy. Another aspect of TBEIC's mission is to work with local nonprofits in addition to energy-

based businesses, as such approximately 10% of the space is dedicated to non-energy enterprises. Figures 14(a) through 14(l) depict various events at the TBEIC facility.

(a) Ohio Ethics training with Susan Willeke from the State of Ohio Ethics Commission

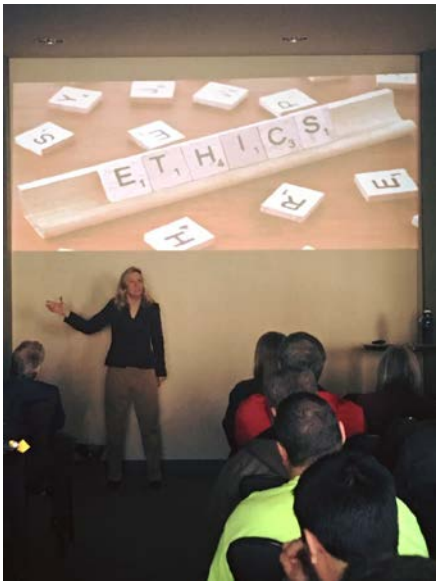

(b) The ethics training seminar with Susan Willeke was sponsored by the Western Reserve Port Authority

(c) The Valley Alliance for Science and Technology (VAST) Seminar

(d) Dr. Du talking fuel cell research with YSU Mike Hripko at a VAST Seminar

(e) Visit by Congressman Ryan: Introducing NASA Glenn Orion Project Director Tim Tyburski

(f) Frequent Visits by Congressman Ryan: TBEIC Founders Forum

(g) Presidential Inauguration Event

(h) Presidential Inauguration Event

(i) Tenants gathering for coffee break

(j) A “Warren Now!” Public event

(k) Tenants: Modern Methods Brewing Company

(l) Tenants: Modern Methods Brewing Company

Figure 14. Events at the TBEIC Facility

3. Evaluation of Venturi Shroud for Horizontal Axis Wind Turbine

As a research element, the project included development in the theory of shrouded turbines. First, fluid power derivation will be compared between the conventional, unshrouded turbines and shrouded turbine geometries. This theory assumes that a certain amount of air avoids the swept area of the turbine, causing a drop on velocity and therefore energy available to the machine. The effect of the shrouded turbine on this inlet effect needs developed. Second, the conventional theory assumes that the wind angle is at a constant 90° to the wind turbine rotation. In the shrouded turbine, the angle of the wind is changed, changing the lift and drag characteristics. This variable wind direction was included through experimental wind tunnel testing and validated computational fluid dynamics simulations.

Therefore, the focus of this research had been on the aerodynamic investigations for developing of the shrouded augmented wind turbine (SAWT) design. Past studies of the SAWT was represented with a remarkable advancement in output power performance compared to a bare wind turbine. In order to further enhance the augmented velocity and achieve even better distribution of the air velocity inside the shroud, an optimizing design was sought. However, the economic issues were underlying considerations. The computational analysis on six various full scale shroud models and experimental investigations had been undertaken in the achievement of this goal.

Section 3.1 explores the physics described in literature reviews showed the axial momentum theory developed for bare wind turbines by Hansen (2008), and followed some conclusions of other works on shrouded wind turbines. **Section 3.2** describes some methodology views behind the shroud design. The effect of various design parameters on the shroud performance may well be accepted as the most important issues, particularly drag force, area ratio, angle of attack, cost effect, and shroud geometric influences. **Section 3.3** describes the experimental installation and procedures. The task of the first experiment was to determine velocity distribution in the testing section, using low airspeed wind tunnel. In the second experiment, the optimized shroud design was selected according to computational and theoretical analysis and then printed with a 3D printer using PLA plastic material. This experiment consisted of creating and testing micro-empty shroud that would be used to verify the CFD results of air velocity distribution and argumentation factor. The third experiment included testing a micro-wind turbine with and without the shroud. The extracted power difference between shroud augmented wind turbine and bare wind turbine was determined. **Section 3.4** illustrates computational fluid dynamic techniques based on the solution of the Navier-Stokes equations using ANSYS-FLUENT 14&15. These techniques were applied to the configurations of shroud

geometries of six models created by using software SolidWorks13 based on airfoil E423 databases. Airfoil E423 is an Eppler high lift airfoil created by NACA. Each model was generated by revolving the airfoil E423 around an axis of symmetry. Models named M1, M2, M3, and M4 were created under different angle of attacks. While models M1, M5, and M6 were created under different length ratio. Model M1 was considered as optimum and the reference model. A model denoted M7_EX was the result of scaling down model M1 and was used for comparison to the experimental investigations. **Section 3.5** contains the validation results between computational and experimental work as well as the results of numerical calculations that were performed on the six various models and the experimental model. Finally, **Section 3.6** presents the information concerning the design, build, and installation of the full scale wind turbine at Youngstown State University. Since the data acquisition is ongoing, preliminary power curves are presented.

3.1.Introduction to Shrouded Wind Turbines

For at least 3000 years before using wind to generate electricity, wind power had been used in land windmills, mainly for grinding grain or pumping water. At sea, the wind has been an important source of power for sailing ships for a long time. Windmills, which were designed in a horizontal axis configuration, were an integral part of the rural economy. In addition over 2000 years ago, the Chinese invented vertical-axis windmills which are still used today. Over this long history of use, the wind has been strongly established as a means to create mechanical power.

Industrialization, first in Europe and later in America, led to mostly abandoning the windmill and replacing it with the stream engine for power operation. However, in 1888, Charles F. Brush, a famous engineer/inventor from Cleveland, Ohio, USA, had the idea to use large windmills to generate electricity; it is believed to be the first turbine operating automatically by using wind power. It was approximately 90 feet high from ground to rotor “blade” tip and weighed approximately 80,000 pounds, Figure 15. The wind rotor was a giant wheel 56 feet in diameter, composed of 144 wooden, propeller-like blades with a total “sail surface” of 1,800 square feet. The assembly also featured a 60-foot-long tail vain to turn the blades into oncoming wind. It reportedly supplied 12 KW of power, 350 glowing lights, 2 arc lights, and a number of motors at his home for 30 years (Righter, 1996).

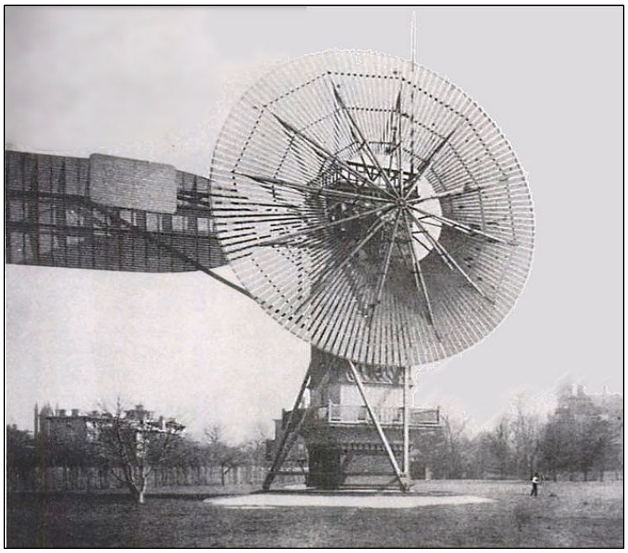

Figure 15. Charles Brush's windmill of 1888, used for generating electricity (Righter, 1996)

In relatively recent times, the usage of wind turbines has gained momentum. This is partially due to environmental threats from fossil fuel usage. It has become essential to look for energy sources which are renewable and clean to eliminate or reduce the environmental pollution and lower economic costs. In addition, expanding new economies from former third world countries have all contributed to an ever increasing need for energy and thus renewable energy technologies. According to Fuel Economy of the Official US Government Source (2012), highway vehicles release about 1.5 billion metric tons of greenhouse gases (GHGS) into the atmosphere each year-mostly in the form of carbon dioxide (CO_2) - contributing to global climate change. Each gallon of gasoline burned creates twenty pounds of CO_2; that is roughly five to nine tons of CO_2 each year for a typical vehicle.

Therefore, the wind turbine has been used as renewable and alternative energy in addition to other sources such as hydropower, solar energy, and biofuel. The fundamental application of wind turbines is to extract energy from the wind. Hence, the aerodynamics is a very important aspect of wind turbines. Like many machines, there are many different types, all based on different energy extraction concepts. In order to optimize the wind turbine as efficient as possible, two main considerations need addressed. First is the strategic positioning of the turbines within the wind farm, which have a suitable wind speed during the year, so that the wake effects are minimized and therefore the expected power production maximized. Second is the determination of turbine configurations so that loading and therefore the stresses on various parts of the wind turbine can be calculated in this state, to ensure long term operation.

Hansen (2008) stated a wind turbine transforms the kinetic energy in the wind to mechanical energy in a shaft and finally into electrical energy in a generator. The maximum available energy, P_{max}, is thus obtained if theoretically the wind speed could be reduced to zero.

$$P = \frac{1}{2}\,\dot{m}V_0^2 \tag{3.1}$$

$$P = \frac{1}{2}\,\rho A V_0^3 \tag{3.2}$$

Where $\dot{m}$ is the mass flow rate, V_0 is the wind speed, ρ the density of the air and *A* the area of the rotor plane. Notice that, the power extracted from the wind power is proportional to the wind speed cubed. If there is a slight increase in velocity approaching the rotor area of wind turbine, it leads to a significant increase in output power. In reality and practically, it is impossible to lower the wind speed to zero behind the rotor turbine plane. A power coefficient C_p, is therefore defined as the ratio between the actual power obtained and the maximum available power, which is known as Betz limit. In 1919, the German physicist, Albert Betz, derived a law from the principles of mass and momentum of the air stream flowing through an idealized "actuator disk" that extracts energy from the wind stream, called Betz's Law. It is approximately equal to 0.59 for many of the modern turbine (Hansen, 2008).

Wind power is an affordable, efficient and abundant source of domestic electricity. It's pollution-free and cost-competitive with energy from new coal-fired and gas-fired power plants in many regions. The wind industry has been growing rapidly in recent years. In 2011 alone, according to NRDC (Natural Resourced Defense Council), 3,464 turbines went up across the United States. Today, American wind energy generates enough electricity to power more than 11 million homes, creates steady income for investors and landowners, and provides manufacturing, construction and operation jobs for at least 75,000 Americans. A typical 250 MW wind farm (around 100 turbines) will create 1,073 jobs over the lifetime of the project. By generating additional local and state tax revenues from lease payments, wind farms also have the potential to support other community priorities, such as education, infrastructure, and economic development. In some months, wind energy provides more than six percent of our nation's electricity, and experts estimate that in the future, wind energy could realistically supply five times that amount, thirty percent or more of our electricity needs.

Ducted or shrouded wind turbines have been invented and developed throughout the 20th century. The shrouded wind turbines have led to an increase in the extracted power from the

wind as compared to conventional wind turbines. As mentioned, according to Betz Law, no wind turbine in open flow can capture more than 59% of the available power. However in computational simulations and in controlled experiments, the shrouded wind turbine has been shown to provide higher power coefficients about ($C_p = 2.5$), as compared to the power coefficient in conventional wind turbines.

Because of this significant difference in power coefficient, a review of previous numerical and experimental analysis of shrouded wind turbines was warranted. Hansen (2008) mentioned that by using the assumption of an ideal rotor, it is possible to derive simple relationships between the upstream wind speed V_0, axial velocity at rotor plane u, velocity in wake u_1, the thrust *T*, and the absorbed shaft power. These relationships can be obtained by using momentum theory on rotor plane analysis by applying Bernoulli's equation. Close upstream of the rotor is a small pressure rise from the atmosphere level p_0 to p before a discontinuous pressure drop Δp over the rotor. Downstream of the rotor, the pressure recovers continuously to the atmospheric level, as shown in Figure 16 (Hansen, 2008).

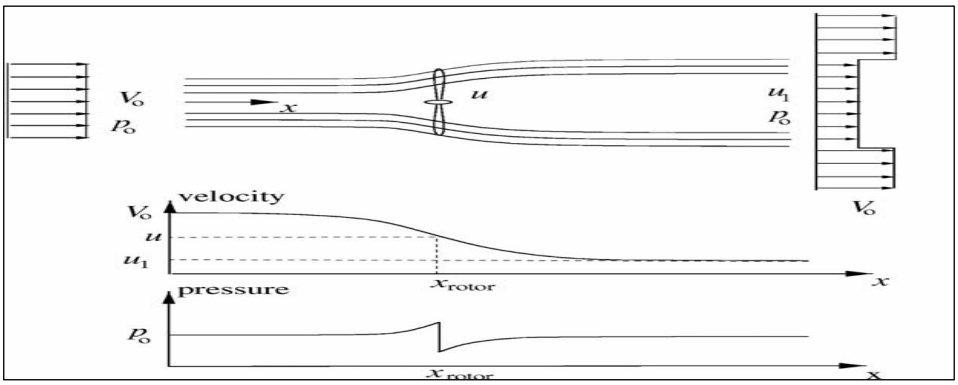

Figure 16. Illustration of Streamlines, Axial Velocity, and Pressure Up- and Down-stream of the rotor (Hansen, 2008)

The thrust, *T*, is the force in the streamwise direction resulting from the pressure drop over the rotor, and is used to reduce the wind speed from V_0 to u_1:

$$T = \Delta p A \tag{3.3}$$

Where $A = \pi R^2$ is the area of the rotor, and Δp is the pressure drop across the rotor. The flow is assumed steady state, incompressible and frictionless. Therefore, the Bernoulli equation is valid from far upstream to just in front of the rotor and just behind the rotor to far downstream in the wake, and combining together, one can derive the expression for pressure drop:

$$\Delta p = \frac{1}{2}\rho(V_0^2 - u_1^2) \tag{3.4}$$

Hansen conducted a control volume analysis as shown in Figure 17 of a bare wind turbine in order to establish power coefficient, C_p. The non-dimensional power coefficient C_p is represented by:

$$C_p = \frac{P_{shaft}}{P_{avail}} = \frac{T \cdot u}{P_{avail}} \tag{3.5}$$

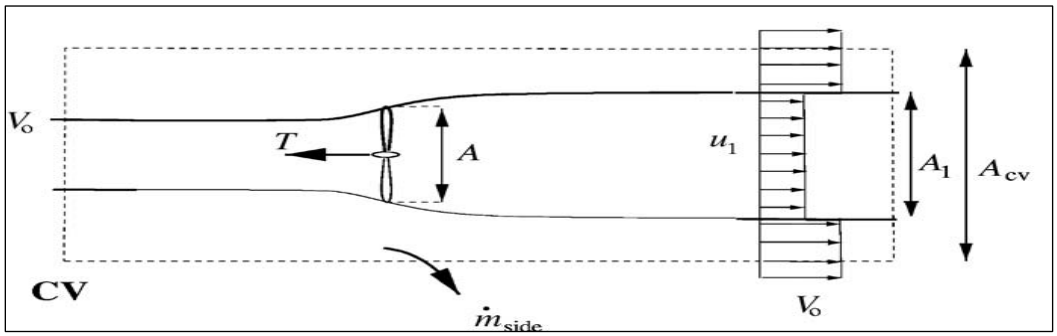

Figure 17. Circular control volumes around a wind turbine (Hansen, 2008)

The velocities in the rotor plane u, and the far wake u_1 are known in terms of induction factor a, and undisturbed velocity V_0 ,where a is fractional decrease in wind velocity between the free stream and energy extraction device; $u = (1-a)V_0$, and $u_1 = (1-2a)V_0$, respectively. The available power in a cross-section to the swept area A by the rotor is $P_{avail} = \frac{1}{2}\rho V_0^3 A$. Using these equations and substituting Equations 3.3 & 3.4 into Equation 3.5, the power coefficient C_p of a bare wind turbine can be simply defined as:

$$C_p = 4a(1-a)^2 \tag{3.6}$$

Similarly, a thrust coefficient C_T is defined as:

$$C_T = \frac{T}{\frac{1}{2}\rho V_0^2 A} = 4a(1-a) \tag{3.7}$$

Differentiating C_p with respect to a, yields:

$$\frac{dC_p}{da} = 4(1-a)(1-3a) \tag{3.8}$$

Then it can be found the $C_{p,max} = {}^{16}/_{27}$ for $a = {}^{1}/_{3}$. This theoretical maximum for an ideal wind turbine without shroud is known as the Betz limit (0.59). Hansen (2008) stated that it is possible to exceed the Betz limit by placing the wind turbine in a diffuser. If the cross-section of the diffuser is shaped like an airfoil, a lift force will be generated by the flow through the diffuser as seen in Figure 18.

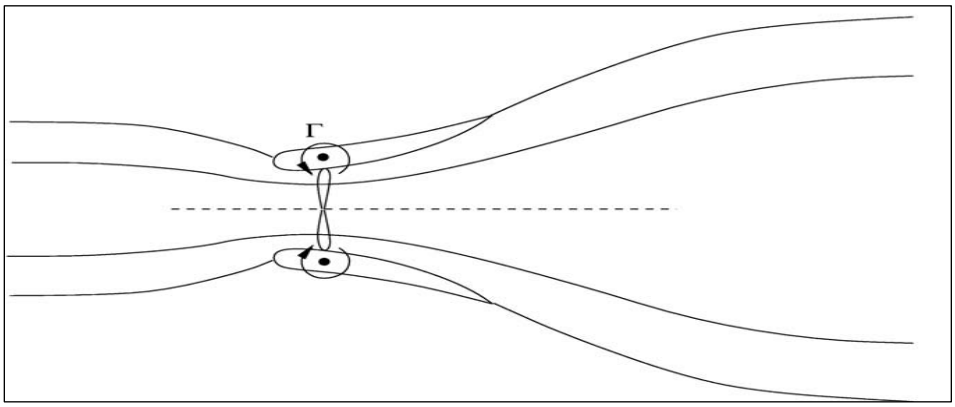

Figure 18. Ideal flows through a wind turbine in a diffuser (Hansen, 2008)

Now, the power coefficient in shrouded wind turbine $C_{p,s}$ becomes:

$$C_{p,s} = \frac{P}{\frac{1}{2}\rho V_0^3 A} = \frac{T.V_2}{\frac{1}{2}\rho V_0^2 \frac{V_0}{V_2} V_2 A} = C_T.\varepsilon \tag{3.9}$$

Where, ε is the augmentation defined as the ratio between the radial velocity in the rotor plane of ducted turbine V_2 and the upstream wind speed V_0 , that is $\varepsilon = V_2/V_0$. The power coefficient $C_{p,b}$ for an ideal bare wind turbine and thrust coefficient C_T from Equations 3.6 and 3.7 combining together give:

$$C_{p,b} = C_T(1 - a) \tag{3.10}$$

Combining Equations 3.9 and 3.10 yields:

$$\frac{C_{p,s}}{C_{p,b}} = \frac{\mathcal{E}}{(1 - a)} \tag{3.11}$$

From the mass flow through a turbine with a shroud $\dot{m}_s$ and the mass flow through a bare turbine $\dot{m}_b$, it can produce:

$$\frac{\dot{m}_s}{\rho V_0 A} = \frac{\rho V_2 A}{\rho V_0 A} = \varepsilon \tag{3.12}$$

$$\frac{\dot{m}_b}{\rho V_0 A} = \frac{\rho(1-a) V_0 A}{\rho V_0 A} = 1 - a \tag{3.13}$$

Hansen et al. (2000) found that the ratio of the power coefficient without shroud and with shroud is represented by the mass flow rate by combining Equations 3.11, 3.12, and 3.13:

$$\frac{C_{p,s}}{C_{p,b}} = \frac{\dot{m}_s}{\dot{m}_b} \tag{3.14}$$

Equation 3.14 states that the relative increase in the power coefficient for a shrouded turbine is proportional to the ratio between the mass flow through the turbine in the shroud and the same turbine without a shroud. The results are that the Betz limit can be exceeded if a device increases the mass flow through the rotor.

Jafari and Kosasih (2014) reported experimental and computational fluid dynamic (CFD) studies that have demonstrated significant power augmentation of a shrouded horizontal axis wind turbine compared to a bare one with the same swept area of the shroud. These studies also found the degree of the augmentation is strongly dependent on the shape and geometry of the shroud, such as the length and the expansion angle.

Jafari and Kosasih concluded in their investigation that the amount of wind energy of air passing the rotor area is proportional to its mass flow rate. There are some methods to increase this mass flow. One method mentioned is by shrouding the rotor with a diffuser, which has an outlet area larger than its inlet. However, an easier method is increasing the swept area of the rotor by enlarging its diameter. The computational results were validated by power output reported from the manufacturer in different wind speeds.

Grassmann, et al. (2003) made a comparison between a bare wind turbine and the shrouded wind turbine in their study on the physics of partially static turbines. The study used CFD simulation for both turbines, and by using specific boundary conditions, taking inlet wind speed 5 m/s, the result are shown in Table 1.

Table 1. Comparison between bare and shrouded propeller (Grassmann et al., 2003)

propeller	Bare propeller	Shrouded propeller
V_2	4.20 $\mathrm{m/s}$	7.95 $\mathrm{m/s}$
F	7.45 N	16.9 N
Available power	31.1 W	135 W
Useful power (P_{shaft})	20.9 W	108 W

Where V_2 is the wind velocity in the rotor plane and *F* is the force in horizontal axis caused by velocity V_2. Another perspective of the shrouded wind turbine, Ohya and Karasudani (2010) developed a shrouded wind turbine by creating a broad-ring brim (flange) at the exit periphery and a wind turbine inside it. Experimental prototype equipped with a brimmed shroud had a rated power of 500 W and the rotor diameter of 0.7 m. The shroud length of this model was 1.47 times as long as the diameter of the diffuser throat *D* ($L_t = 1.47\ D$), and the width the brim was *h* = 0.5 *D*. The shrouded wind turbine with a brimmed diffuser demonstrated power augmentation factors between 2 and 5 compared with a bare wind turbine for a given turbine diameter and wind speed. In addition to the increase in the output power, the experimental investigations showed significant features such as a significant reduction in wind turbine noise, better tracking of the turbine with wind direction, and less over all turbine damage from broken blades during high speed.

3.2. Geometric Consideration of the Shrouded Wind Turbine

The shroud analyzed in the numerical and experimental research was created from airfoil E423, so it has been denoted as shroud E423. Figure 19 shows the shroud E423 configurations. Referring to this figure, *L* is the shroud length, R_{throat} is throat radius, D_{out} is the diameter of outlet section, and α is the expansion angle (angle of attack).

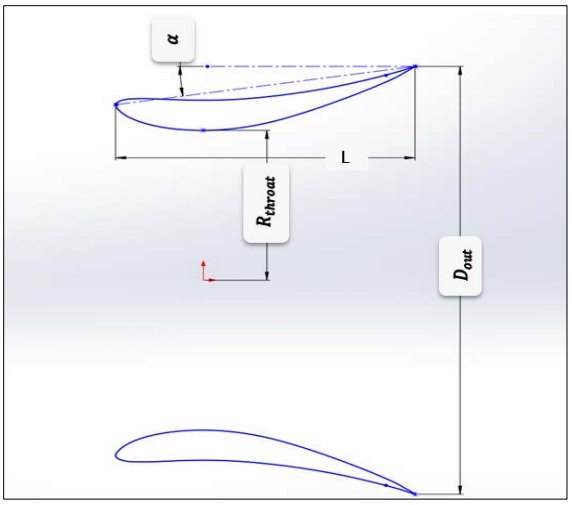

Figure 19. Shroud E423 configuration

As a result of fluid flow over the surface of an airfoil, the two forces exerted on it are denoted as lift and drag force. Lift force is the component of these forces which is perpendicular to the oncoming flow direction while the drag force is the component of the surface force parallel to the flow direction. The lift and drag coefficient C_l and C_d are defined as:

$$C_l = \frac{F_l}{0.5\,\rho\,V_\infty^2\,c} \tag{3.15}$$

$$C_d = \frac{F_d}{0.5\,\rho\,V_\infty^2\,c} \tag{3.16}$$

Where ρ is the air density and *c* is the length of the airfoil or projected area of the body, V_∞ is the incoming relative velocity, and F_l and F_d are the lift and drag forces, respectively. The magnitude of the lift and drag forces is variable depending on body shape and also on the Reynolds number (Hibbeler, 2015).

Since the shroud geometry was created from an airfoil in the curvature shape by revolving it around an axis of symmetry, this shape will generate these forces when the fluid flows on it. However, Widnall (2009) indicated that the lift force on a shroud (duct) is not really lift, but is rather the suction pressure directed towards the axis of symmetry. In addition, Spera (2014) believed that the shroud lift forces are probably responsible for accelerating the wind speed through the throat area.

Each airfoil has specific angle of attack, which is designed for an appropriate purpose. The lift coefficient (C_l) increases linearly with increasing angle of attack (α) until a maximum value of

C_l is reached, with respect to Reynolds number. In the airfoil E423, the drag coefficient has maximum value at low lift coefficient, and the shape of the curve is approximately parabolic (Abbott, 1949), Figures 20(a) and (b).

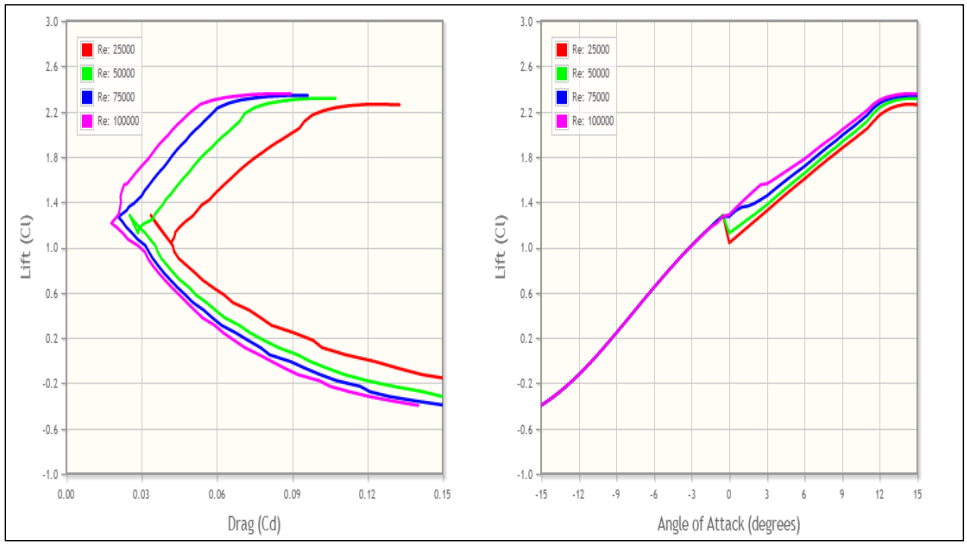

(a) (b)

Figure 20. Lift coefficient vs (a) drag coefficient and (b) angle of attack for airfoil E423 (airfoil investigation database, 2013).

The angle of attack and length of airfoil E423 for shroud geometry was analyzed at different values to maximize the exit area ratio for the shroud, in order to increase the augmentation velocity factor of the shroud. Figure 21 shows airfoil E423 of the shroud under four different angles of attacks.

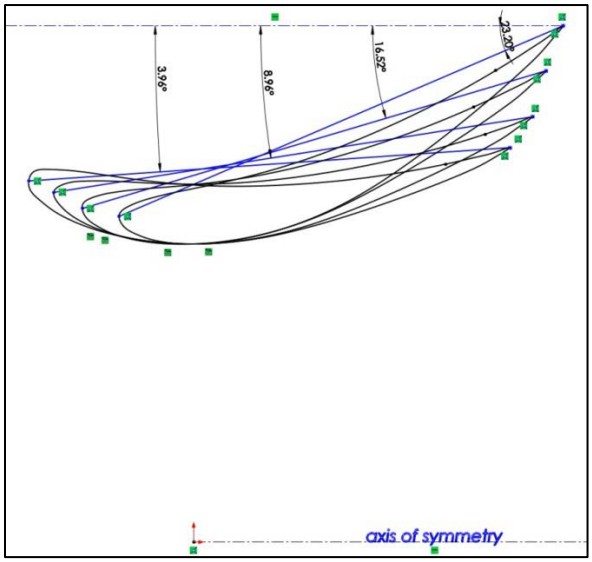

Figure 21. Airfoil E423 profile under different angle of attack**.**

As mentioned previously, Widnall (2009) asserted that the lift force is not a real lift force, rather a suction force directed to the center. According to the numerical analysis on empty shroud E423 in this study, it was found that the lift force is zero, which is directed toward the center of the shroud, and it is independent on the angle of attack. Thus, the influence of the angle of attack only focuses on the drag force.

The drag force has a substantial influence on the shroud design. High drag forces reduce the mass flow rate through the turbine, as will be discussed. In addition, increasing the drag forces can lead to detrimental economic issues.

Foreman (1983) examined drag loads on three conical diffusers in the context of preliminary structural design and the cost estimates. Foreman concluded that with using drag force coefficient (C_d= 0.54) as a half value of total drag coefficient (C_d= 1.1) which was found, based on diffuser frontal area in a 64.9 m/s extreme wind, the cost effectiveness increases with size.

Lubitz and Shomer (2014) described the drag force on the shroud surface as the force acting on diffuser that aligned with the wind

$$F_d = \frac{1}{2} C_{dd} \rho \frac{\pi}{4} \left({D_0}^2 - D_r^2 \right) U^2 \tag{3.17}$$

Where D_0 is diameter of exit area, and D_r is the throat diameter of the shroud, C_{dd} is the diffuser drag coefficient, and U is wind velocity. The researchers concluded that diffusers with flanged exits, sharp bends or very large opening angles (thus causing separated flow) would experience significantly greater aerodynamic drag than long, revolved airfoil diffusers. This can significantly impact required structural strength to ensure survival of the shroud in extreme winds.

It is clear that the design shape of shroud plays a large role in determining the extent of the influence of the drag force. Increasing the efficiency of the shroud requires increasing parameters such as the exit area, but still the benefit from increasing the exit area is worthwhile. While, Lubitz and Shomer (2014) mentioned that, Phillips analysis (2003) found that the cost efficiency of a diffuser augmented wind turbine increases as the extent (size) of the diffuser (whole turbine system) is reduced, resulting in the extreme case that a conventional diffuserless wind turbine would be most cost effective. Phillips (2003) also found, and clearly stated, that it is a design for extreme wind loads that is the limiting structural case

for diffuser augmented wind turbines, and that these loads will be many times greater than for a horizontal axial wind turbine of comparable size.

As can be seen in Equation 3.17, drag force increases with increasing the exit diameter. Foreman et al. (1978) analyzed the diffuser (shroud) cost based on the size of the shroud especially on the dimension of the diameter. The study found that shroud augmented wind turbine can be anywhere from marginally cheaper to much more expensive depending on whose authoritative judgment is used. Considering the benefits of these turbines, including a potentially greater factor for usable annual wind energy pattern, one can conclude they generally become more economical than conventional wind energy conversion systems, regardless of the size turbine costing, the longer they are in operation.

3.3. Wind Tunnel Testing of Shrouded Wind Turbine

Experimental investigations on a micro-shroud wind turbine included measurement of the air velocity distribution inside the shroud at the throat and also power output measurement of a small turbine with and without the shroud. A low speed wind tunnel was used for the experiments. These experiments were important in order to help validate the computational work that is presented in section 3.4 of this report. Before experimentally testing the shroud, the velocity distribution inside the entire wind tunnel was mapped to establish the test section area that exhibited fully developed flow.

3.3.1. Wind Tunnel

The advances in computational fluid dynamics (CFD) modelling on high speed digital computers have reduced the demand for wind tunnel testing. However, CFD results are still not completely reliable and wind tunnels are used to verify the CFD computer codes. The wind tunnel which was available at Youngstown State University is an open, low air speed tunnel with small size of dimensions 16’ x 4’ x 4’. The aluminum structure of the side walls are covered by thick glass sheets to become a good monitor during the test as shown in Figure 22. The wind tunnel consists of an axial fan (Cincinnati Fan –Size 48) which is powered by a 10 horsepower motor in a 4 feet diameter housing. The wind tunnel is capable of generating wind speeds up to 34 mph.

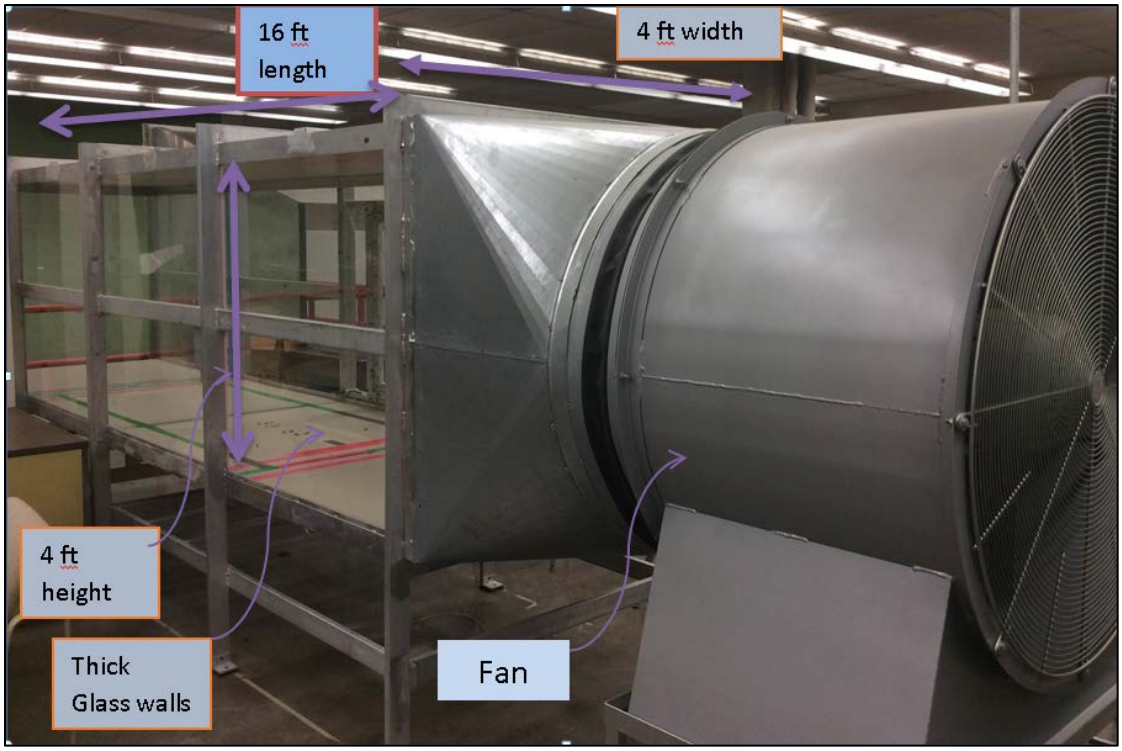

Figure 22. Low Speed Wind Tunnel at YSU

The motor fan is controlled by a small computer. The LabVIEW v8.6 software was used to control the wind tunnel, including switching on the fan and controlling the speed, while reversing the fan direction was done manually from the fan system VFD.

3.3.2. Experimental Apparatus (Preparations and Tools)

The preparation for the experiments required a setup of the wind tunnel with computer software. The apparatus that was used to receive and transform the information to the LabVIEW (computer) was DAQ (Data Acquisition device) NI cDAQ-9172, module NI 9264 as shown in Figure 23. The DAQ hardware acts as the interface between a computer and signals from the outside world. It primarily functions as a device that digitizes incoming analog signals so that a computer can interpret them.

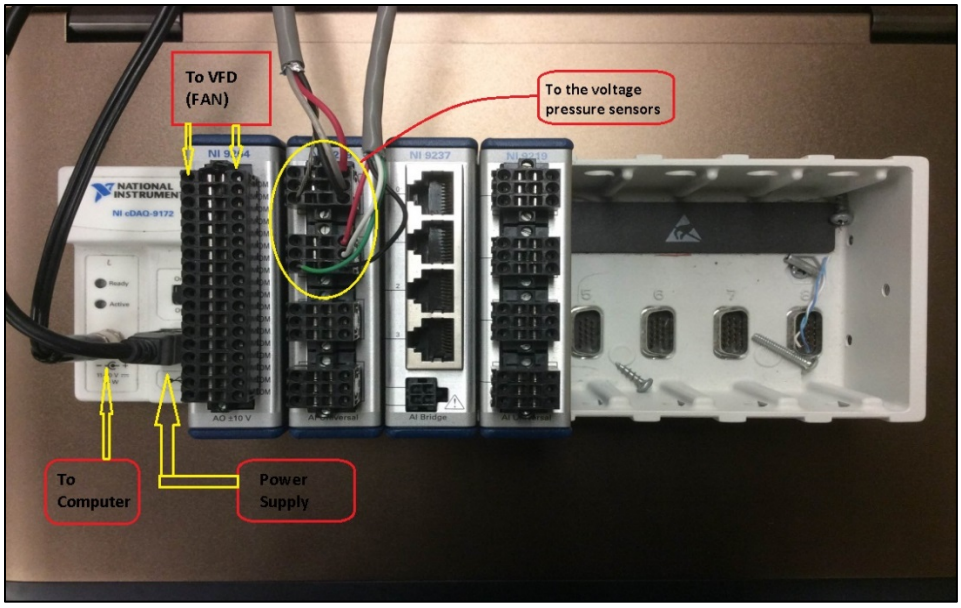

Figure 23. Data Acquisition device (DAQ)

The Fan was run by a variable frequency drive (VFD) Allen Bradley Model PowerFlex-4M connected to the DAQ. The DAQ permitted an input voltage to the fan which varied from 0 to 8 V DC. Also, the frequency input for the VFD has an input range, from 0 to 80 Hz, which is capable of providing wind speeds up to 34 mph from the fan.

A pitot -static tube (166-12,1/8" diameter, 12" insertion Depth, 3" tip length) was used to measure the static and total pressure in order to calculate the air speed inside the wind tunnel at specific points. A pitot-static tube has two ports; static pressure (P_{static}) and total pressure (P_{total}). The difference between these two pressures is the dynamic pressure which is used to determine wind speed. Connecting a differential pressure transducer across the two ports will therefore measure $P_{dynamic}$ directly (PI Research, 2014).

The pitot-static tube was connected to a pressure sensor through thin plastic tubing (1/8" diameter). The MLV (Magnetic Low Voltage) series, low voltage pressure sensors, wired to the DAQ, transfers the signal to the computer software (LabVIEW). Two pitot-static tubes and pressure sensors were used in the experiment. Unit conversions were done in LabVIEW to change the dynamic pressure readings to equivalent air flow measurements.

The experimental tools and devices were set and installed properly to achieve accurate results of the dynamic pressure measurements**.** Figure 24 shows the setup of instrumentation block diagram, based on measuring the airspeed distribution in the selected section inside the wind tunnel. The block diagram includes the apparatuses that were used in the experiments.

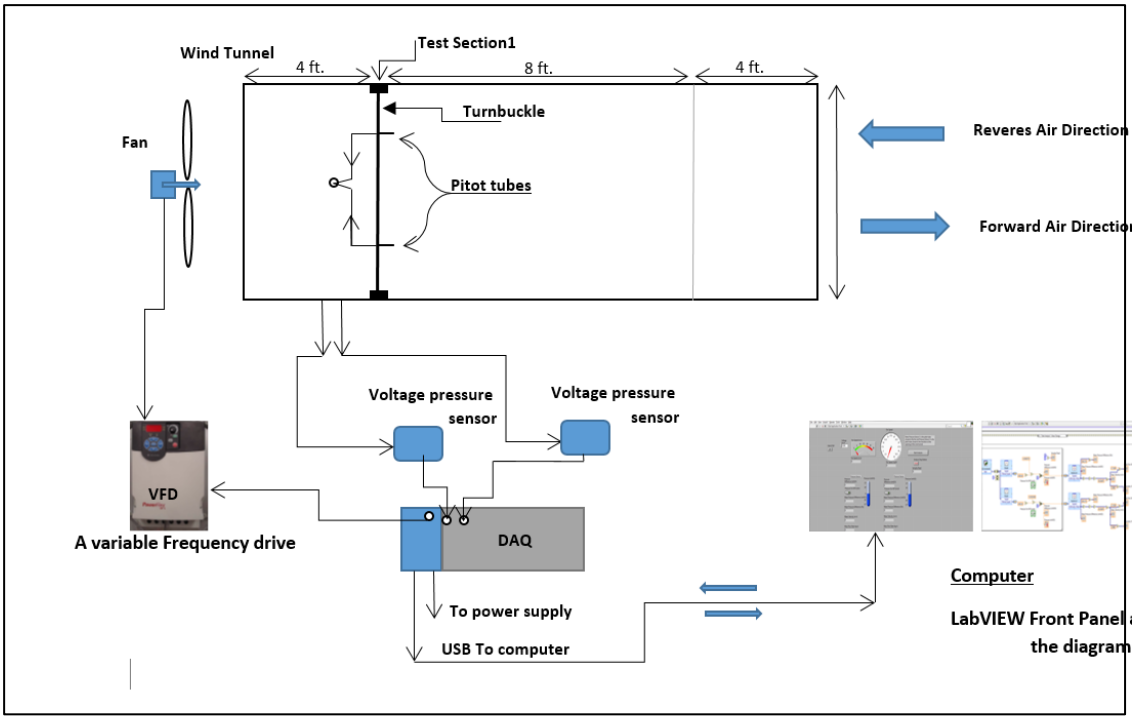

Figure 24. Schematic of the experimental wind tunnel setup

3.3.3. Measurement of Velocity Distribution inside Wind Tunnel

The first experiment was performed to determine the most consistent testing section area in wind tunnel. Two sections were tested with the air flow in both the positive and negative axial directions. The first section was four feet from the fan, and the second section was twelve feet from the fan, close to the open end, as shown in Figure 25.

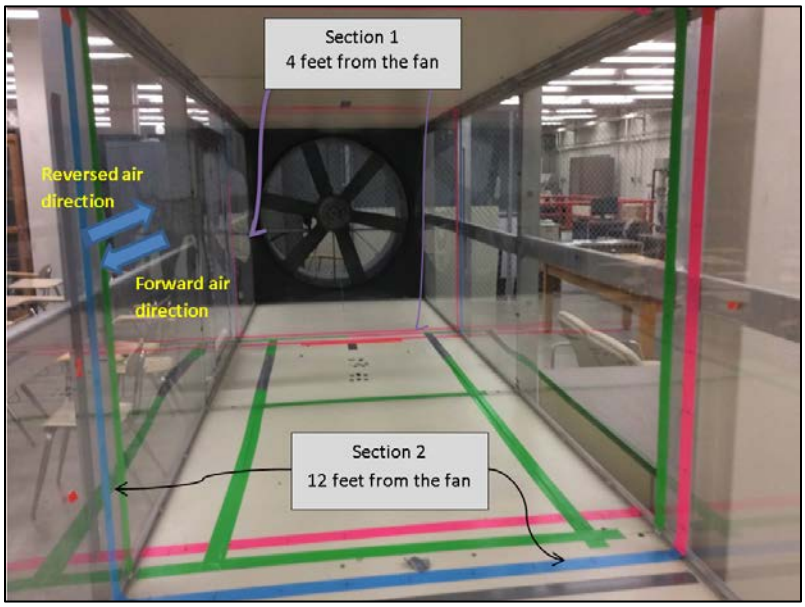

Figure 25. Test Sections inside Wind Tunnel

It was determined that Section 1 with reverse air direction was the best configuration for testing the shroud. The velocity profile was fully developed in this section, so it was decided to place the shroud at its center. The graphic plot of the first section is shown in Figure 26.1. The maximum velocity in center reached 9.1 m/s, and minimum velocity was 4.3 m/s close to the walls for a control voltage of 5.5 volts.

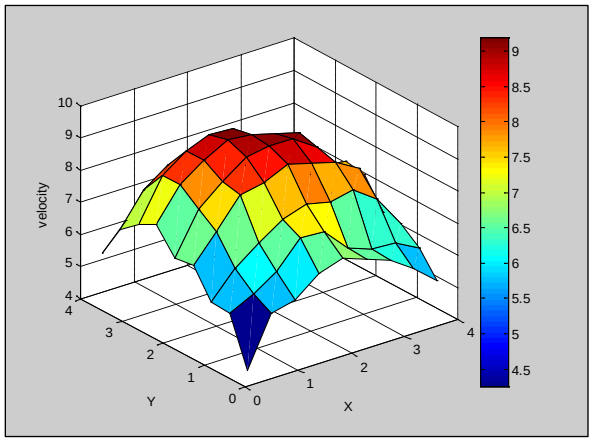

Figure 26.1. Air velocity distribution at section1 (reverse direction)

3.3.4. Experimental Shroud Model, Setup, and Method

The shroud model was designed in SolidWorks based on the coordinates of the airfoil E423. To create the full solid body, the sketch was positioned with respect to an axisymmetric center-line. The experimental shroud size was a result of scaling down a full optimum size with scale factor of 0.0265 because the wind tunnel was not large enough to test full size. The throat radius (R_{throat}) of experimental shroud model was 4.46 inches, and the length (L) was 7.18 inches resulting in L/R_{throat} of 1.6. The shroud expansion angle, α was $8.96°$ giving outlet and inlet area ratio (β) of 2, as shown in Figure 26.2.

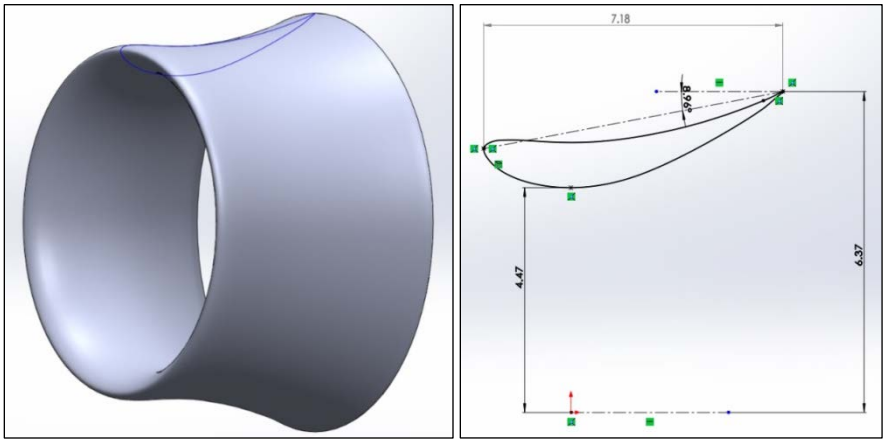

Figure 26.2. Configurations of the Experimental Shroud Model

After the model was designed in SolidWorks, it was printed in a 3D printer machine (MAKERBOT REPLICATOR 2X) to get more precise configurations for the model. Because of the 3D printer size, the shroud was printed in 8 pieces and then glued and taped together to get a rigid, sustainable experimental part. Figures 27.1-27.6 depict some stages of creating the experimental shroud model.

Figure 27. Experimental shroud (Shroud manufacturing steps): (1-2) glued parts together (3) sand the surfaces to be smooth (4) taped the whole model (5-6) complete model

The shroud was setup in the testing section, 4 feet from the fan, as a result of the first experiment showing this section had fully developed velocity when the air direction was reversed (backward). In order to measure the velocity distribution inside shroud throat area, two pitot tubes were used. One of them was placed inside the shroud and the other was placed 5 inches just in the front of it. The velocity readings were taken along the radial axis at throat region since the shroud has axis-symmetric geometry, as shown in Figure 28.

The wind tunnel was run under input voltage 5.5 volts, which provides airspeed of producing maximum air velocity 16.4 m/s inside the shroud. The Reynolds number for wind tunnel was $5.87\ x\ 10^5$ where the mean air velocity at 5.5 volts was 7.33 m/s inside wind tunnel. Based on this mean air velocity (7.33 m/s), Mach number was 0.0213.

Figure 28. Pitot static tubes placed inside and outside the shroud

The results and comparisons to the computational simulations are discussed in section 3.5.

3.3.5. Micro-Shroud Testing with Small Turbine

In the final experiment, a micro-wind turbine was built in order to measure the extracted power without a shroud and then with this turbine inside the shroud throat area. The micro turbine consisted of a small generator (3000 rev/min, 12V-24V, 31mm diameter, 3.175mm shaft diameter, and 52 mm length), as shown in Figure 29(a). The model turbine has three blades, modeled from NACA 4415 airfoil profile with angle of attacks variant between 2.8° and 27°. The blades and nacelle were sketched in SolidWorks, and then printed in 3D printer (MAKERBOT REPLICATOR 2X), as shown in Figure 29(b).

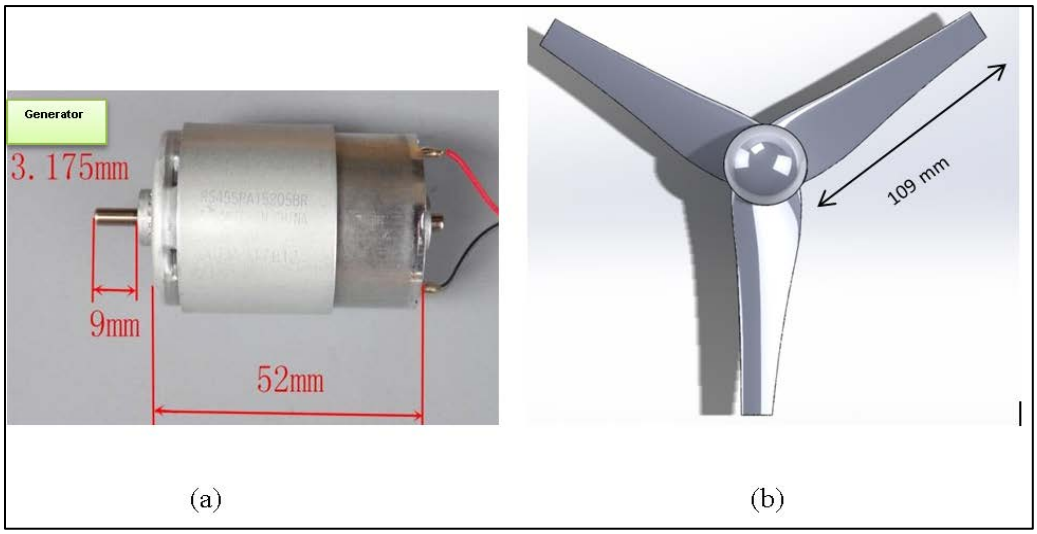

Figure 29. Micro-wind turbine: (a) Micro Generator (b) Airfoil NACA4415 and Nacelle

The length of each blade was 109 mm in order to fit in the shroud throat area. The clearance was approximately 2mm between the shroud inner perimeter and blade tip. Three different voltage multi-meters were used to measure the voltage and the current, to ensure consistency of results. Power was calculated from these measurements by using the simple electric power relationship.

$$\text{Power } (P) = \text{Voltage } (v) \text{ x Current } (i) \tag{3.18}$$

Both the bare wind turbine and shrouded wind turbine were placed in the test section in the wind tunnel. A pitot tube was put 5 inches in front of the turbine to measure the inlet velocity as shown in Figure 30.

(a) (b)

Figure 30. Micro-Turbine in Test Section: (a) with and (b) without Micro-Shroud

The results are discussed in section 3.5.

3.4. Computational Fluid Dynamics of the Shrouded Wind Turbine

Computational fluid dynamics (CFD) is process by which numerical solution to fluid flow problems are obtained by the use of computers. The advanced computers with large memory and high speed have enabled CFD programs to achieve solution to many flow problems such as those that are compressible or incompressible, laminar or turbulent (Ganis, 2003). CFD analysis employs a number of algorithm equations, which replace the differential equations. The differential equations for fluid flow problems are the continuity (conservation of mass), Navier-Stokes (conservation of momentum), and the conservation of energy equations. The numerical method used corresponds to the finite volume and finite difference method when using the

commercially available code ANSYS FLUENT. In turbulence modeling, the standard $\kappa - \varepsilon$ and $\kappa - \omega$ turbulence models were used in this study. In 2-Dimensional analysis, the standard $\kappa - \varepsilon$ turbulence model is a widely accepted model for turbulent flow simulation in CFD.

3.4.1. Mass and Momentum Conservation Equations

The fluid motion can be described by the dynamic equations for fluid. The conservation of mass or continuity equation states that the local rate of change of mass within the control volume, plus the net rate of mass entering and leaving the open control surface must equal zero. Since the analysis in this research was 2D axisymmetric, the continuity equation must be expressed in polar coordinate:

$$\frac{\partial \rho}{\partial t} + \frac{\partial (\rho \mathrm{v}_x)}{\partial x} + \frac{\partial (\rho \mathrm{v}_r)}{\partial r} + \frac{\rho \mathrm{v}_r}{r} = S_m \tag{3.19}$$

Where, *r* is the radial coordinate, *x* is the axial coordinate, v_x is the axial velocity, v_r is the radial velocity, and S_m is the source term.

The conservation of momentum equation can be obtained by applying the fundamental principles of Newton's second law of motion to the fluid domain. Newton's second law states that the net force on an element, or a particle, is equal to the time rate of change of its linear momentum. This law can be applied to a fluid particle moving through 3-dimensional space where the total momentum of any system, the instant directly prior to an event will equal the total moment of the system in the instant immediately after event. The net force on the particle, or object, in the *x*-direction is equal to the time rate of change of its linear momentum in the *x*-direction. The conservation of momentum equation can be written in general form (Cartesian coordinates):

$$\frac{\partial \rho V}{\partial t} + \nabla \cdot \rho \vec{V} V = -\nabla p + \rho g + \nabla \tau \tag{3.20}$$

Where, V is general velocity component, p is the pressure, g is the gravity, and τ is the shear stress.

3.4.2. Navier-Stokes' Equation for Axisymmetric Analysis

The 2-D and 3-D incompressible Navier-Stokes Cartesian equations cause the weak solution based on the regularity assumed for velocity. According to Ukhovskii (1968), if the initial data and the domain are symmetric and θ-component of initial velocity is zero, then the solution becomes regular. In this study, the shroud E423 was cylindrically symmetric and the domain

kept symmetric so that there was no θ-component of velocity. According to this assumption, a weak solution becomes indeed a strong solution. The axisymmetric conservation of momentum equation can be expressed:

$$\frac{\partial(\partial v_x)}{\partial t}+\frac{1}{r}\frac{\partial(r\rho v_x v_x)}{\partial x}+\frac{1}{r}\frac{\partial(r\rho v_r v_x)}{\partial r}$$
$$=-\frac{\partial(p)}{\partial x}+\frac{1}{r}\frac{\partial\left[r\mu\left\{2\frac{\partial(v_x)}{\partial x}-\frac{2}{3}(\nabla.v)\right\}\right]}{\partial x}+\frac{1}{r}\frac{\left[r\mu\left\{\frac{\partial(v_x)}{\partial r}+\frac{\partial(v_r)}{\partial x}\right\}\right]}{\partial x}+F_x \qquad (3.21)$$

For axisymmetric flow, there is no flow in the θ-direction and all θ derivatives are identically zero. Thus it is considered a function of only two variables, *r* the radial direction and *x* the axial direction.

3.4.3. Turbulence Modelling – Eddy viscosity

$\kappa-\varepsilon$ Turbulence Model: The model is based upon the exact transport equations for the turbulence kinetic energy κ and its dissipation rate ε (Sveningsson, 2003). P. Bulat and V. Bulat (2013) stated that, in the standard $\kappa-\varepsilon$ turbulence model, viscosity is determined by a single characteristic linear turbulence scale; in reality all scales of motion contribute to turbulent diffusion. The modelled κ and ε equations are:

$$\frac{\partial k}{\partial t}+u_j\frac{\partial k}{\partial x_j}=\frac{\partial}{\partial x_j}\left(\left(v+\frac{v_t}{\sigma_k}\right)\frac{\partial k}{\partial x_j}\right)+P_k-\varepsilon \qquad (3.22)$$

$$\frac{\partial \varepsilon}{\partial t}+u_j\frac{\partial \varepsilon}{\partial x_j}=\frac{\partial}{\partial x_j}\left(\left(v+\frac{v_t}{\sigma_\varepsilon}\right)\frac{\partial \varepsilon}{\partial x_j}\right)+\frac{C_{\varepsilon1}P_k-C_{\varepsilon2}\varepsilon}{\mathcal{T}} \qquad (3.23)$$

Where $\mathcal{T}$: turbulent time scale ($\mathcal{T}\geq 6\sqrt{\nu/\varepsilon}$)

P_k : Production turbulent kinetic energy $P_k=2v_tS^2$, $S^2=S_{ij}S_{ij}$

S_{ij} : Symmetric part of the mean strain rate tensor, $S_{ij}=\frac{1}{2}\left(\frac{\partial U_i}{\partial x_j}+\frac{\partial U_j}{\partial x_i}\right)$

v : Kinematic viscosity

v_t : Kinematic turbulent viscosity

$U_{i,j}$: Mean velocity in x, y-direction respectively

The standard $\kappa-\varepsilon$ model coefficients were kept as a default in shroud analysis:

$$C_\mu=0.09,\quad C_{\varepsilon1}=1.44,\quad C_{\varepsilon2}=1.92,\qquad \sigma_k=1.0,\ \ \sigma_\varepsilon=1.3$$

$\kappa - \omega$ Turbulence Model: The model is the same as the $\kappa - \varepsilon$ model, but it employs equations for the turbulent energy dissipation rate (ω) instead of dissipation equation ε . The modelled κ and ω equations are:

$$\frac{\partial k}{\partial t} + u_j \frac{\partial k}{\partial x_j} = \frac{\partial}{\partial x_j}\left((\nu + \sigma^* \nu_t)\frac{\partial k}{\partial x_j}\right) + P_k - \beta^* \omega k \tag{3.24}$$

$$\frac{\partial \omega}{\partial t} + u_j \frac{\partial \omega}{\partial x_j} = \frac{\partial}{\partial x_j}\left((\nu + \sigma \nu_t)\frac{\partial \omega}{\partial x_j}\right) + \gamma \frac{\omega}{k} P_k - \beta \omega^2 \tag{3.25}$$

Where: $\nu_t = \gamma^* \frac{k}{\omega}$

The standard $\kappa - \omega$ model coefficients are:

$$\beta = {}^{3}/_{40}, \quad \beta^* = {}^{9}/_{100}, \quad \gamma = {}^{5}/_{9}, \quad \gamma^* = 1, \quad \sigma = 0.5, \qquad \sigma^* = 0.5$$

3.4.4. Fluent Solver Algorithms

The FLUENT solver has provided two basic solver algorithms: The first is a density-based coupled solver (DBCS) that uses the solution of the coupled system of fluid dynamics equations (continuity, momentum and energy); the second is a pressure-based algorithm solver (PBCS) that solves the equations in a segregated or uncoupled manner. The segregated pressure-based algorithm has proven to be both robust and versatile, and it has been utilized in concert with a wide range of physical models, including multiphase flows, conjugate heat transfer and combustion (Kelecy, 2008*).* The pressure-based solver in ANSYS-FLUENT is used for most incompressible flows, while the density-based solver is used for compressible flows. Since there was no heat included in this analysis of study, and the flow over the shroud was incompressible, the pressure-based solver was used and the energy equation was turned off.

The pressure-based solver uses an algorithm, which classified as general classic method called the projection method. Based on this method, the continuity (or mass) equation represented by the velocity field is obtained by solving the pressure correction equation. In order to satisfy the continuity equation, the velocity field should be corrected by the pressure field. Also, in the momentum equation, the process of solving velocity field is the same as in continuity equation. Because the governing equations are non-linear and coupled to one another, they are solved frequently with the required number of iterations until the solution reaches the convergence (Fluent Inc., 2013-2014).

3.4.5. Physical Modeling, Computational Domain, and Boundary Conditions

Different geometries of the shroud design for CFD modeling were analyzed using ANSYS-FLUENT 14 and ANSYS-FLUENT 15. The models were created in SOLIDWORKS 13 based on the airfoils E423 (Eppler E423 high lift airfoil) database with changing the angle of attack. Six models in full scale were analyzed in 2D simulation of the axisymmetric shroud body expressed in polar coordinates. The experimental comparison model analyzed in 2D was a scale down of full optimum model size with an area ratio of 2. In addition, CFD analysis included simulation in 3D for drag force investigations.

Six full scale models with proposed throat radius of 168 inches were modeled in solidworks. These models, shown in Figures 31 and 32, were simulated in ANSYS-FLUENT to investigate the effects of changing the length and angle of attack on the aerodynamic performances of the shroud E423. In addition, these models were designed to determine the available amount of the extracted power of each model. The scaled down experimental validation model (named M7_EX) is shown in Figure 33. It was a scale model of M1 since preliminary computational analysis showed this to be the optimum reference model based on augmentation velocity factor, power performance, and cost efficiency.

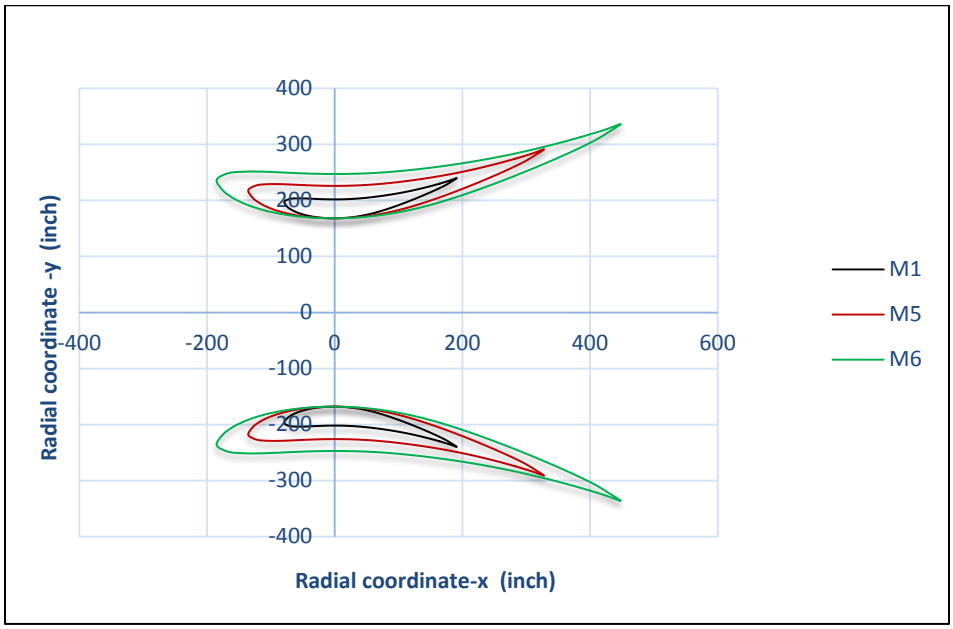

Figure 31. Shroud models M1, M5, and M6 showing change in the shroud length with the angle of attack and throat radius kept constant

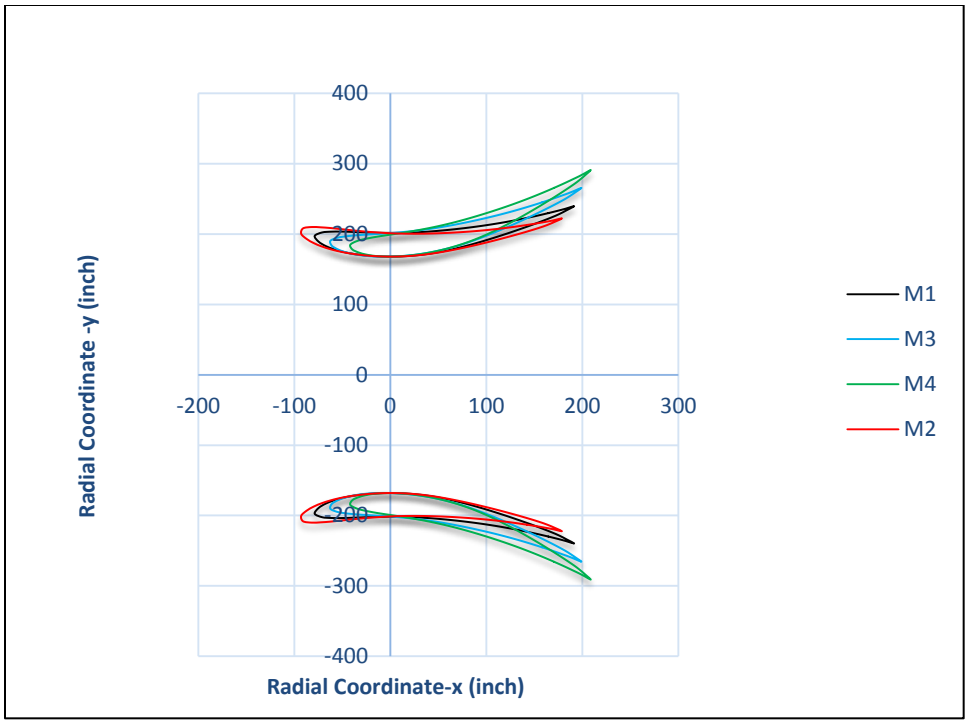

Figure 32. Shroud models M1, M2, M3, and M4 showing change in the angle of attack with the length and throat radius kept constant

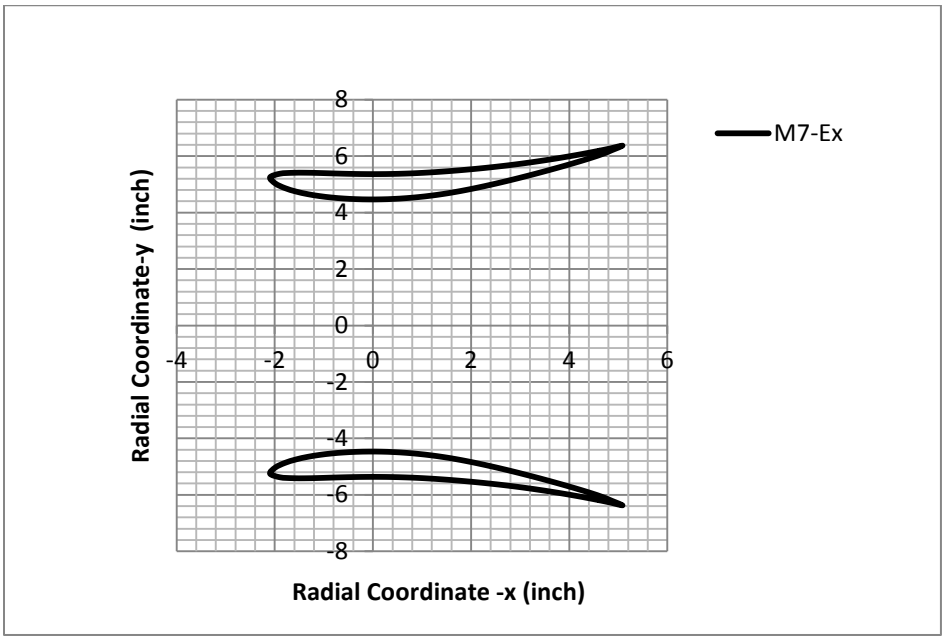

Figure 33. Experimental shroud model M7-Ex scaled down of M1

Table 2 shows clearly the configurations of the shroud models. As compared to model M1, the models M5 and M6 were changed in the length but with throat radius and angle of attack kept constant to give area ratios of 3, and 4, respectively. Models M2, M3, and M4 had different angles of attack, keeping the throat radius and length constant resulting in area ratios of 1.75, 2.5, and 3 respectively.

Table 2. Configurations of the six models and experiment model

Model Type	Description	Angle of attack α	Area Ratio β	Length Ratio L/R_{th}
M1	Optimum Model	8.96	2	1.6
M2	α : reduced; R_{th}& L : constant	3.96	1.75	1.6
M3	α : increased; R_{th}& L : constant	16.52	2.5	1.6
M4	α : increased; R_{th}& L : constant	23.2	3	1.6
M5	L : increased; R_{th}& α : constant	8.96	3	2.75
M6	L : increased; R_{th}& α : constant	8.96	4	3.77
M7_EX	Exp. model: 0.0265"scale of M1	8.96	2	1.6

Since the shroud E423 geometry was axisymmetric, the 2D simulation was performed on only half of the empty shroud for each of seven models. To avoid any blockage effect, save the analysis time, and achieve converged solution, the rectangular computational domain was sized to $(75\ x\ R_{throat})$ long and $(29\ x\ R_{throat})$ high for the full-scale size models, as shown in Figure 34. For the micro-experimental model, the computational domain was $(90\ x\ R_{throat})$ long and $(33\ x\ R_{throat})$ high.

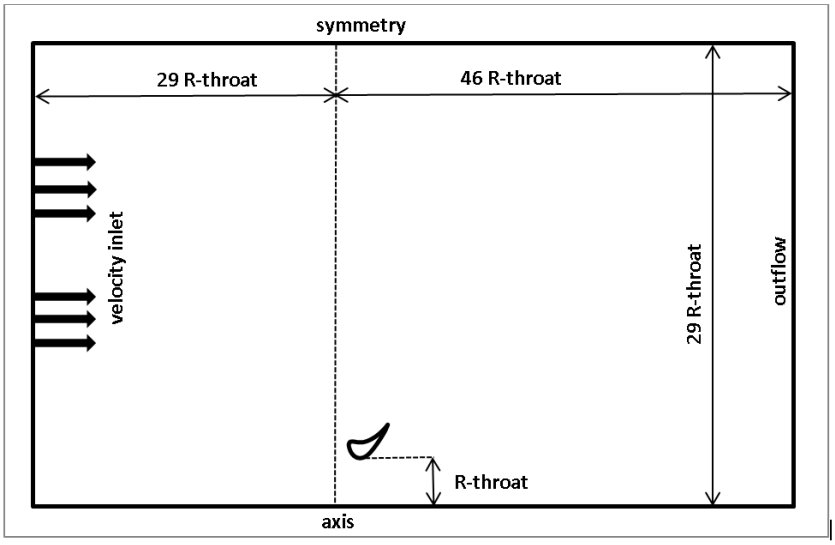

Figure 34. Axisymmetric Computational Domain

The goal of 3D analysis in ANSYS-FLUENT 15 was to analyze the drag force effect on the empty shroud for each model. The domain was taken as cylindrical symmetry, only a portion of 60°, with radius $(23\ x\ R_{throat})$ and length $(60\ x\ R_{throat})$, as shown in Figure 35.

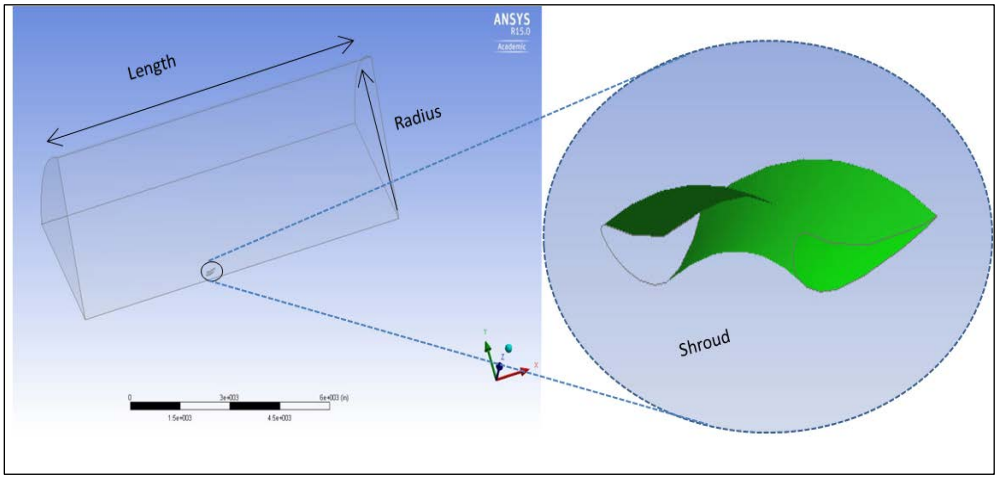

Figure 35. 3D Computational Fluid Domain for 60° Portion of Empty Shroud Model

Ansys-Workbench was used to create the model's domain and mesh in this analysis. For the 2D simulation, each model was discretized into approximately 140,000 triangle elements using unstructured mesh. It was difficult to generate structured mesh in workbench around the shroud geometry analyzed with an axisymmetric domain since the airfoils have sharp edge, and a curvature shape. However, five layers of structured quadrilateral mesh were created around the shroud surface to capture the boundary layer affects. Adjacent to this, a very fine triangular mesh was created and extended in both x and y-directions the boundary layer mesh, out from the shroud. Beyond these two regions, larger triangular meshes were utilized. All three regions are illustrated in Figure 36.

The relevant center of mesh shape was selected fine with high smoothing. The minimum mesh size was varied from 0.5 inches to 1 inch depending on the model configuration, while the maximum mesh size reached to 200 inches. These sizes were for full size model. For the micro-experimental model, 0.03 inches was the minimum and 11.79 inches the maximum mesh sizes.

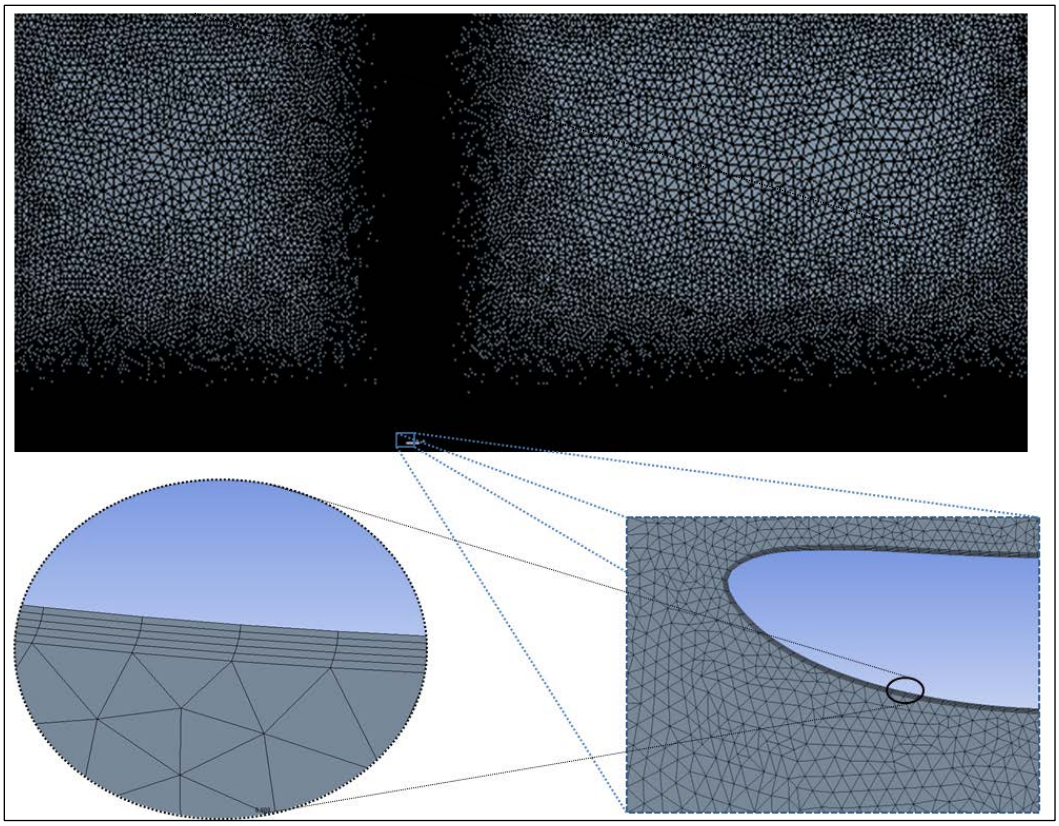

Figure 36. Unstructured triangle mesh with showing layers around the shroud

The mesh in the 3D modeling was also created in Workbench of ANSYS-FlUENT15, for a 60° portion of the shroud model**.** Unstructured meshes of 2,558,323 tetrahedron elements were used. Again five hexahedron boundary layers were added along the surface of the shroud, shown in Figure 37.

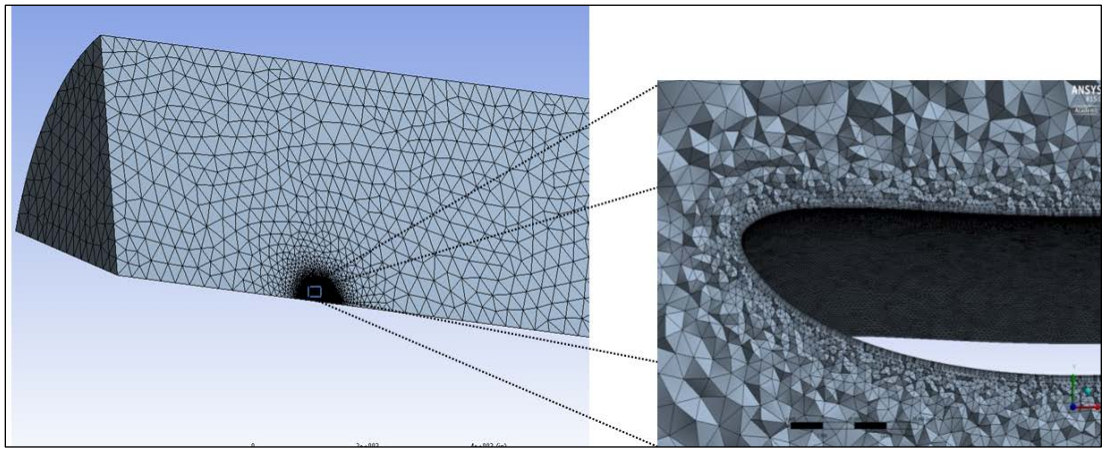

Figure 37. Three-Dimensional Mesh for a 60° Portion of the Empty Shroud

Numerical simulations of 2D and 3D models were carried out using Fluent 14 &15. The fluid flow was considered as steady state flow in order to simplify the CFD simulations for the wind tunnel experiments. As mentioned previously, pressure-based solver was chosen since the flow over the shroud was assumed incompressible under very small Mach number. Since the shroud is symmetric, the axisymmetric analysis was utilized for the 2D simulations to lower the number of iterations, and therefore time, to reach a converged solution.

The inlet boundary condition was a constant free stream velocity of 5 m/s for full size models and the outlet boundary of the domain was set to zero atmospheric pressure (operating pressure 101,325 Pa). The inlet velocity for experimental validation model was 8.98 m/s which was the same velocity used in wind tunnel. The turbulent intensity was set to 5% since it was assumed as a free-stream, low velocity operation.

Simple scheme of pressure –velocity coupling was selected even though it takes little more time than couple scheme to reach convergence; it is more accurate for steady state flow. The residual convergence criteria were chosen 10^{-6} which gave convergent solution with around 1200 iterations. As discussed previously, the 2D simulations employed the $\kappa - \varepsilon$ turbulence model while the 3D simulations employed the $\kappa - \omega$ turbulence model.

The wind tunnel used in the experiment of this study was small with dimensions of (16x4x4) feet. As mentioned previously, the wind tunnel was not large enough to test the full size model of exit diameter 39.95 feet. In order to match the augmentation velocity factor and other results between the experimental model and full size model M1, it was required to scale the velocity and the geometry. The experimental model M7 used in this investigation was 1.06 feet in exit diameter and 0.598 feet in the length.

In order to make a similitude between the experiment model and the prototype, it was necessary for the Reynolds number to be the same for both of them (Hibbeler, 2015).

$$\left(\frac{\rho VD}{\mu}\right)_m = \left(\frac{\rho VD}{\mu}\right)_p \tag{3.26}$$

Where ρ is the air density, μ is the air viscosity, *V* is the air velocity, *D* shroud diameter, m is the model, and p is the prototype .The same fluid was used for both the model and the prototype. Therefore, its properties ρ and μ will be the same, then:

$$V_m D_m = V_p D_p \tag{3.27}$$

Equation 3.27 is the reason that the computational full scale model was not directly verified by the experimental model. The air velocity of the experimental would need to be over 37 times that of the computational simulation. By running a simulation of the same size shroud as the experiment, the velocity could be kept the same. Since the computational scale up was consistent, confidence in the results was achieved.

3.5.Experimental and Computational Results and Comparisons

3.5.1. Computational Results Validation by Wind Tunnel Testing

In order to validate the CFD simulation results, wind tunnel experiments were conducted with shroud E423 as discussed previously. The validation experimental work was performed on a scaled down empty micro-shroud of area ratio equal to 2. The properties in both wind tunnel and CFD analysis were assumed the same. Figure 38 shows experimental results of the velocity distribution at the throat area of the empty micro-shroud placed inside the test section of the wind tunnel. The solid line represents the velocity distribution at 5 inches just before the shroud inlet section. The marked line represents the augmented velocity at throat section of the shroud model M7_EX. The outside readings were taken in radial distance of 8 inches to cover a larger area, while the radial distance inside the throat area of shroud was at a maximum of 4.33 inches. The maximum velocity (V_{max} =16.48 m/s) occurred at the radius 4.33 inches inside the shroud throat section. The maximum radius R_{max} was considered the maximum radial distance of 8 inches, which was taken outside the shroud, and at the section plane just 5 inches in front of the inlet section of the shroud.

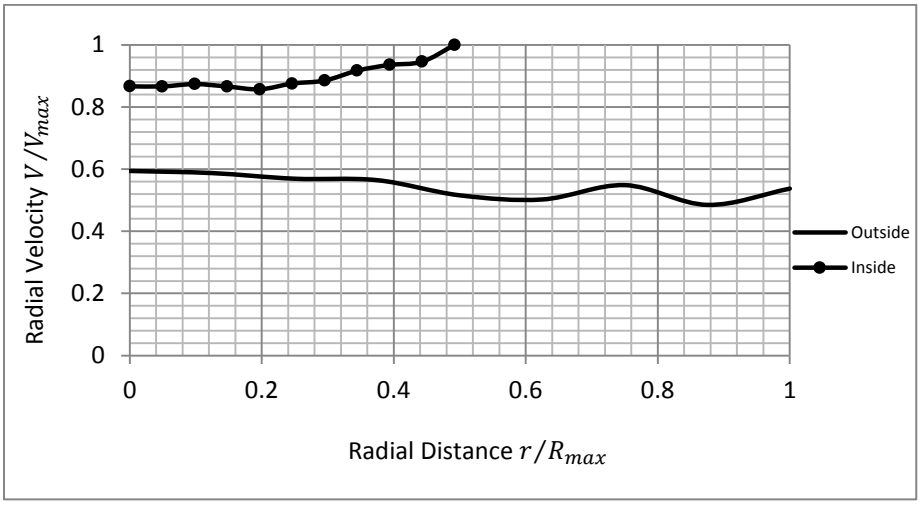

Figure 38. Experimental results of non-dimensional air velocity distribution

In this investigation**,** good agreement was found between numerical and experimental results with an error of about 1.06%, which validated the numerical model. Figure 39 shows the numerical and experimental results represented in non-dimensional form**.** The maximum velocity (V_{max} =17.612 m/s) occurred in CFD modeling at radius 0.108 m where maximum radius is 0.111 m (4.33 inches), and the inlet velocity was 8.98 m/s.

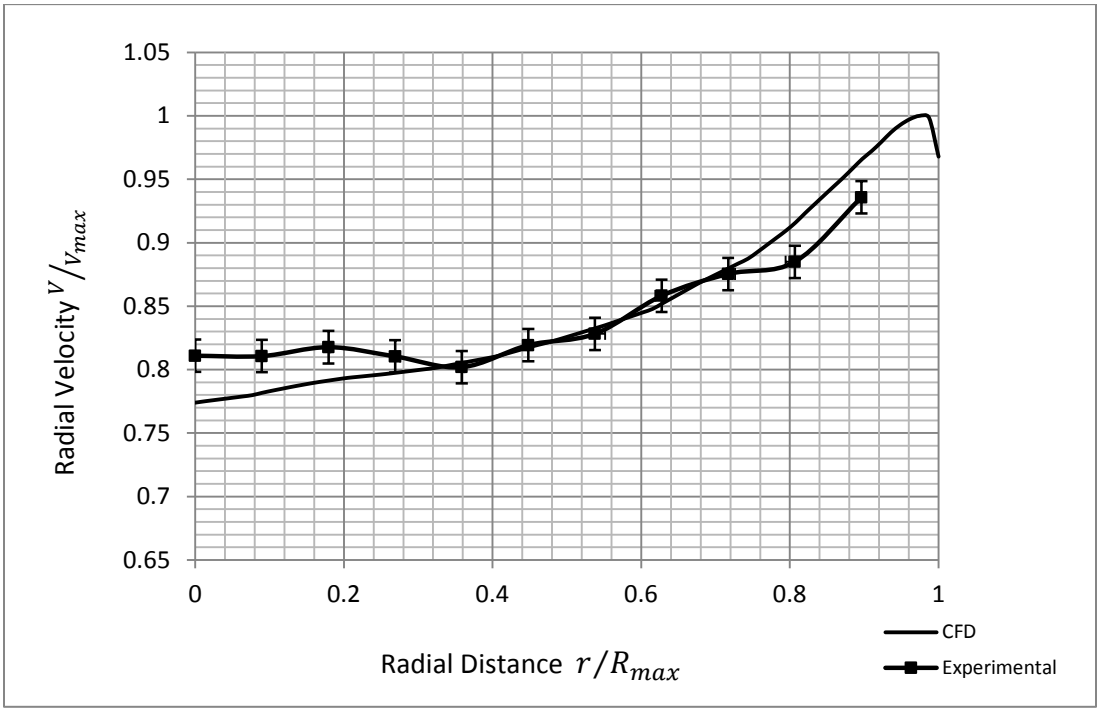

Figure 39. Numerical Vs Experimental Empty Micro-Shroud Results

As mentioned previously, the inlet velocity for the CFD comparison was the same as the one used in the wind tunnel velocity (8.98 m/s). Then, the full size of the model M1 was scaled down to be the same experimental model. Table 3 shows the comparison of the augmentation factor between the numerical and experimental work.The scaled shroud model M7_EX, with $V_0 = 8.98$ m/s produced augmentation factors of 1.66 in CFD analysis and 1.65 in experimental work.

Table 3. CFD vs Experimental Results on Empty Micro-Shroud

	CFD	Experimental Test
V_{inlet}	8.98 m/s	8.98 m/s
$V_{average\ at\ throat}$	14.97 m/s	14.81 m/s
Augmentation Factor AF0	1.667	1.65

In case of full-scale shroud size, throat radius was assumed 168 inches, and the augmentation factor of Model M1 was 1.9. In order to get the same value of the augmentation factor for model M7_EX, the inlet velocity had to be scaled up according to similitude requirements discussed earlier. While it was not feasible to do this experimentally, it was appropriate to do so in the scaled down simulation model. The velocity for full scale was assumed 5 m/s, then by applying Equation 3.27 the velocity became 187 m/s, which approximately gave augmentation factor 1.89 for experimental model M7_EX in CFD simulation, Figure 40.

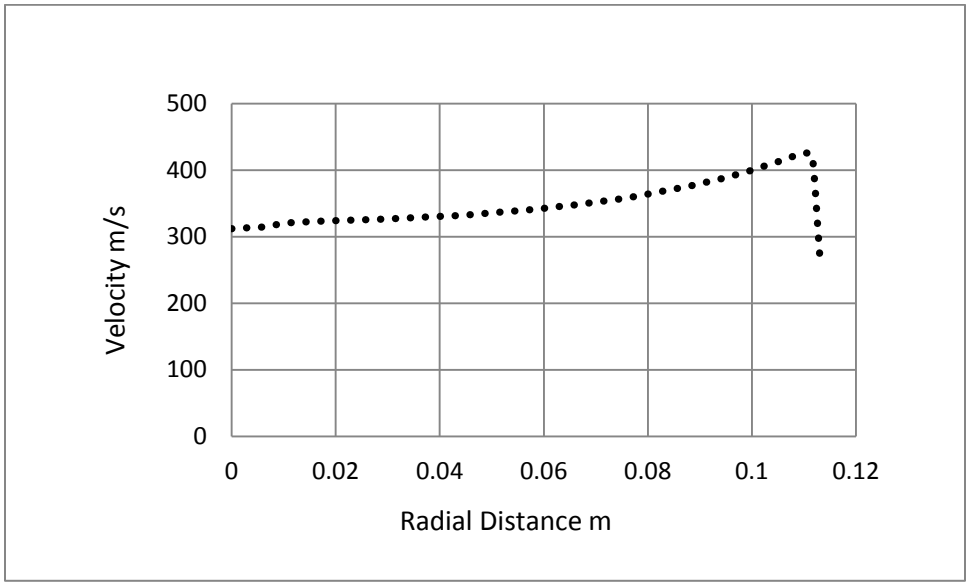

Figure 40. Plot of the velocity at the throat area of the shroud against the radial position for experimental validation model M7_EX at inlet velocity 187 m/s

3.5.2. Full Scale Augmentation Factor AF0 and Radial Velocity Distribution

The improvement of the shroud's augmentation capabilities was sought in this study. After validation of the CFD simulations, analysis on the six different models of empty shroud E423 was conducted. It was found that the wind speed is doubled inside the shroud particularly in throat area, as shown in Figure 41.

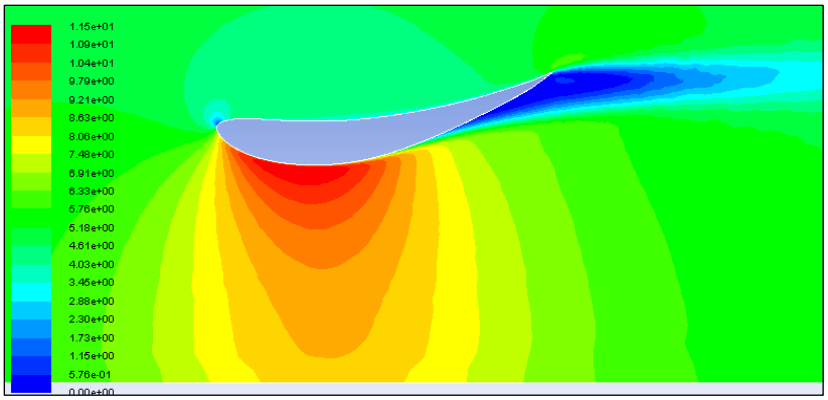

Figure 41. Velocity contour of the axisymmetric empty shroud E423 of M1

The augmentation velocity factor (AF0) is the first factor affecting the increase in power output and the method of comparison used by Shroud Augmented Wind Turbines (SAWT) to determine whether the system is worth developing. In other words, the augmentation factor describes the SAWT efficiency. Igra (1981), and Widnall (2009), referred to the augmentation velocity factor (AF0), as the ratio of the average wind velocity in the throat area of the shroud to the undisturbed wind velocity ($V_{throat\ ave.}/V_0$). Table 4 shows the augmentation velocity factors (AF0) for each model. A higher AF0 indicates a higher mass flow rate through the shroud throat area, thus increasing the extracted power.

Table 4. Augmentation Velocity Factors for Empty Shroud E423 Models

Model	AF0	Model	AF0
M1	1.9	M4	1.742
M2	1.82	M5	2.11
M3	1.785	M6	2.16

There is significant increase in AF0 in models M5 and M6 since these models were increased in length and area ratio, as shown in Table 2. However, model M4, which has area ratio of 3, was much lower than M1 (optimum model) even though it has higher area ratio. This was caused by the higher separation layers, leading to lower mass flow rates in the throat area of models M3 and M4. Also, the entrance section of both models M3 and M4 were reduced (because of high angle of attack) compared to M1. The large curvature section enhanced the inlet section (entrance) of the shroud model M1, and served as a nozzle. In the model M3 and M4, it can be seen that increasing the area ratio without increasing the shroud length appropriately, caused high separation layers and then led to a reduced AF0.

Figure 42 shows radial velocity distribution in the shroud throat area. The maximum velocity was $V_{max} = 12.0633$ m/s for an inlet velocity of 5 m/s. For the non-dimensional velocity, V_{max} occurred in model M5 at a radius ratio of 0.97, while maximum radius R_{max} is 4.2164 m for all models. Model M5 and M6 have higher air velocity since they have highest area ratio and longest length. The model M1 (AR=2), in the bold line, also has good air velocity distribution compared with other models. In the all models, a remarkable increase in wind speed can be obtained, achieving a high average velocity in the throat plane that is 1.82 – 2.16 times greater than that of the approaching wind velocity V_0.

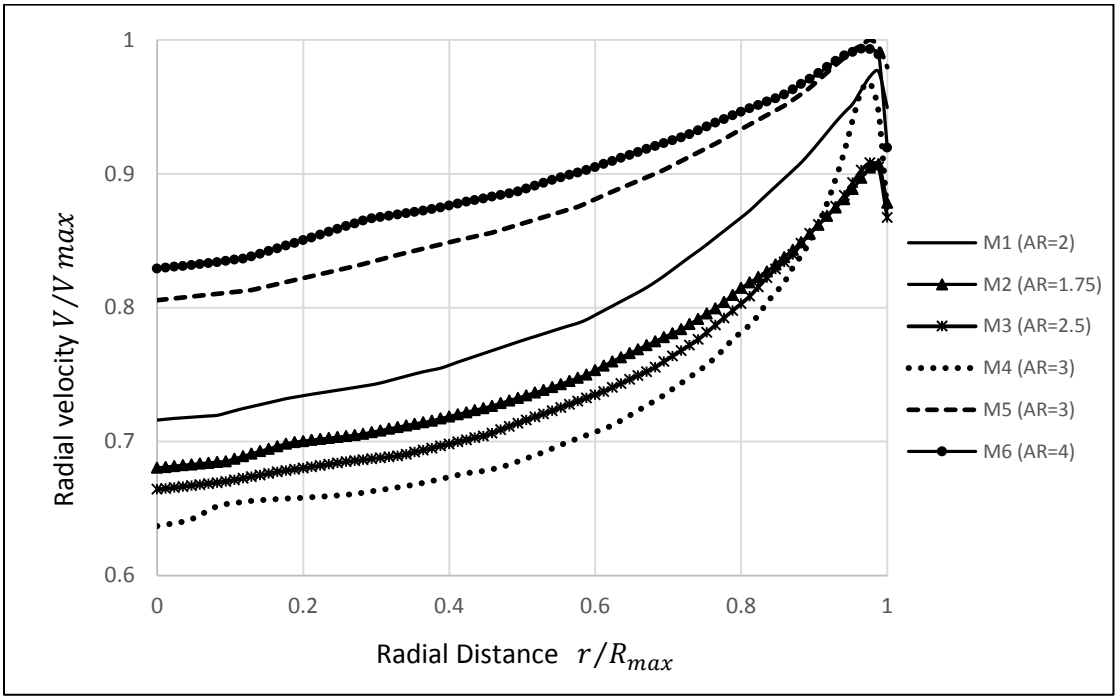

Figure 42. Non-dimensional, radial velocity distribution in the throat section of the shrouds

3.5.3. Back-Pressure Ratio γ and Radial Velocity Distribution at the Shroud Exit Plane

The CFD analysis on the six models revealed an improvement in the pressure recovery. It was discussed previously that the pressure drops when entering the shroud and continues to drop causing increase in the velocity, while trying to return to the static pressure once passing the exit plane. The pressure recovery or back pressure was described as ratio of velocities in Van Bussel equation for extracted power. It is the ratio of the average velocity in the exit plane of the shroud to the undisturbed wind velocity ($\gamma = V_{exit}/V_0$). According to the Van Bussel, the power increases with increasing γ.

Table 5 shows the back pressure ratios for the six models. A significant increase of the back pressure ratio γ was observed in the model M1 and M2 compared to the other models. The

effect of extending the shroud length (in model M5 & M6), and increasing the angle of attack (in model M3 & M4), resulted in a lower back pressure ratio γ.

Table 5. Back pressure ratios for the six models of the empty shroud E423

Model	Back-Pressure γ
M1	**1.1353**
M2	**1.1996**
M3	**1.0011**
M4	**0.9077**
M5	**1.0001**
M6	**0.8682**

Figure 43 shows the non-dimensional air velocity distribution in the exit section of the shroud models. A significant lower sub-atmospheric pressure has surrounded the outlet of the shroud. There is low pressure region at trail edge of the shroud caused by flow separation from the shroud surface as referred in the figure. The higher area ratio of the models provides a greater base pressure effect, and then produces higher separation flow at the exit area. The maximum velocity (V_{max} = 6.706 m/s) occurred in model M1 at $r = .99$ m while R_{max} is 8.5344 m.

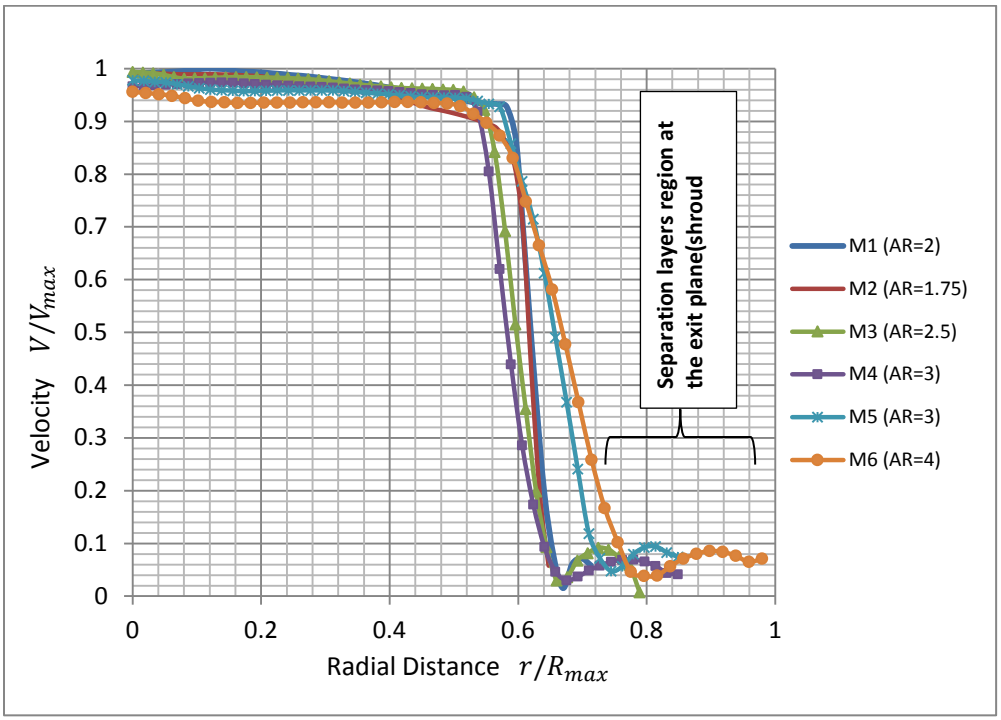

Figure 43. Non-dimensional, radial velocity distribution in the exit plane of the shrouds

3.5.4. Pressure Distribution Along and Inside the Empty Shroud

Figure 44 shows the pressure distribution inside the empty shroud models, along *x*- coordinate in two different radial positions. In position 1, which is radially at the R_{max} of the throat area, the pressure drops pointedly at the throat area and then it tries to recover at exit area (at the trailing edge of the shroud) where the separation layers start. In position 2, which is at the centerline (r = 0), the pressure is a little higher; this means the velocity at the center is less than that at the edge of shroud as showed previously in Figures 41 and 42. The minimum static pressure is ($p_{\min}$ =– 76.2 Pa), which occurred in model M5 at axial distance -0.12**,** where x_{max} is the shroud cord length in positive direction. The radial plane of the throat section was aligned with origin.

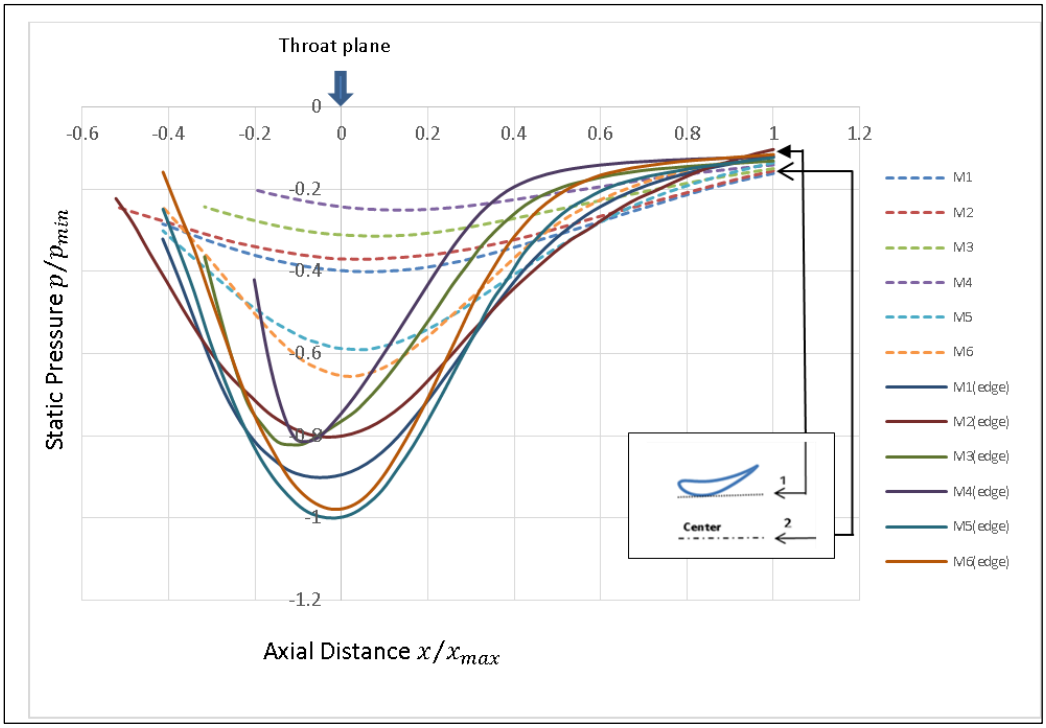

Figure 44. Axial pressure distributions along the empty shroud E423 models at two positions.

Figure 45 illustrates the static pressure distribution along the entire empty shroud surface, both outer and inner, for each model. The pressure drop in the throat area of the shroud (as shown at the readings -0.8 and -1) indicates the velocity is at maximum. It can be seen clearly that at approximately 80% of airfoil cord length the flow starts to separate which is indicated by an increase in the static pressure. In outer surface of the shroud, the static pressure is higher at stagnation point of the leading edge (as shown at 0.2). In general, the pressure over the outer surface is greater which causes the lift force that is directed toward the center of the shroud. As a reference, Figure 46 illustrates this in contour form for the M1.

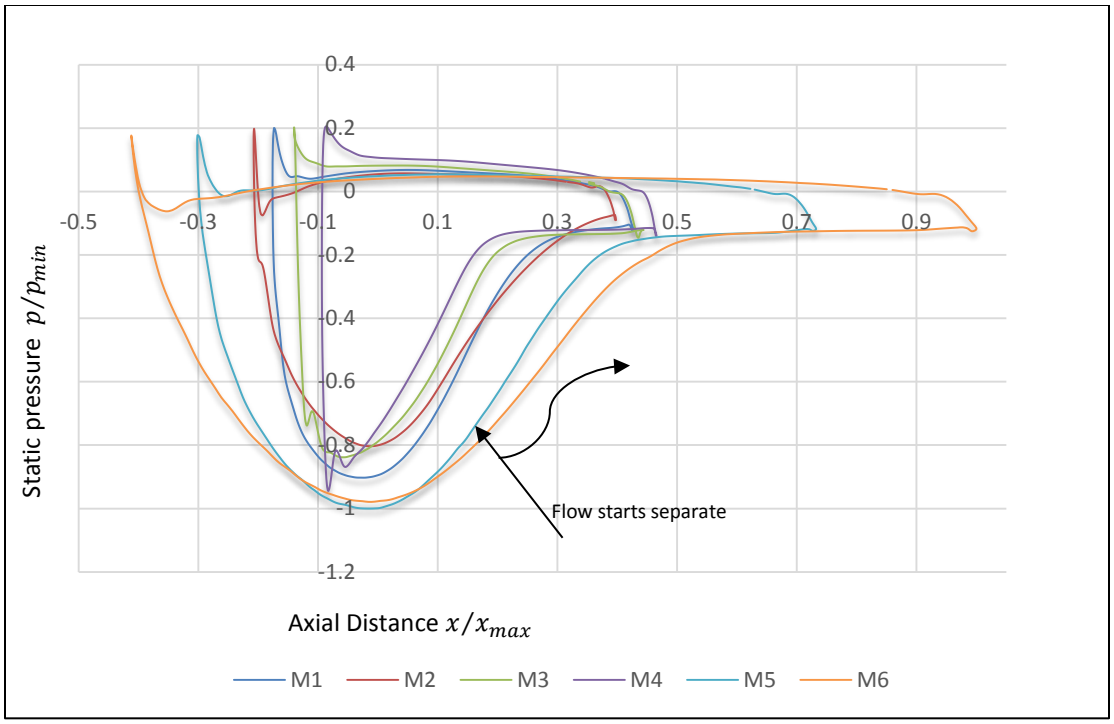

Figure 45. Static pressure distribution over outer/inner surface of empty shroud E423 models

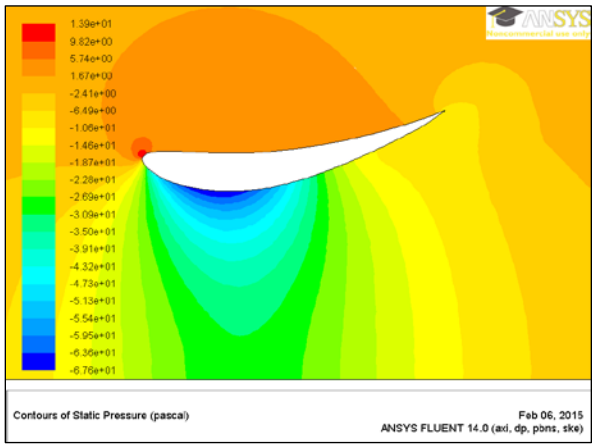

Figure 46. Static pressure contour of the empty shroud model M1

3.5.5. Drag Force Analysis

The drag force effect on the empty shroud models was analyzed computationally in 2D simulation and confirmed with 3D simulation. Table 6 shows the drag force coefficient (C_d) and configurations for each model. The drag force coefficient was calculated using Equation 3.16, with the drag force obtained from CFD analysis. As discussed previously, the drag force acts normally on the projected frontal annular area.

Table 6. Geometry configurations of empty shroud for the six models and drag coefficients

Model	Area ratio	Angle of attack α	$\mathrm{L/R_{th}}$	C_d
M1	2	8.96	1.6	0.3417
M2	1.75	3.96	1.6	0.2319
M3	2.5	16.52	1.6	0.5588
M4	3	23.2	1.6	0.6
M5	3	8.96	2.75	0.5394
M6	4	8.96	3.769	0.5908

Figure 47 shows that the drag coefficient increases with increasing the angle of attack. Since the drag force is a combination of both the pressure drag and friction drag, the pressure drag acting on the frontal area will maximize once this area became bigger. As a result of increasing the angle of attack, the frontal area exposed to airflow will become larger. Model M4, that has angle of attack $\alpha = 23.2°$ showed drag coefficient of 0.6, while model M2, that has α=3.96°, showed drag coefficient of 0.2319. Indeed, the drag coefficient of model M1 was close to that of model M2, which was the minimum.

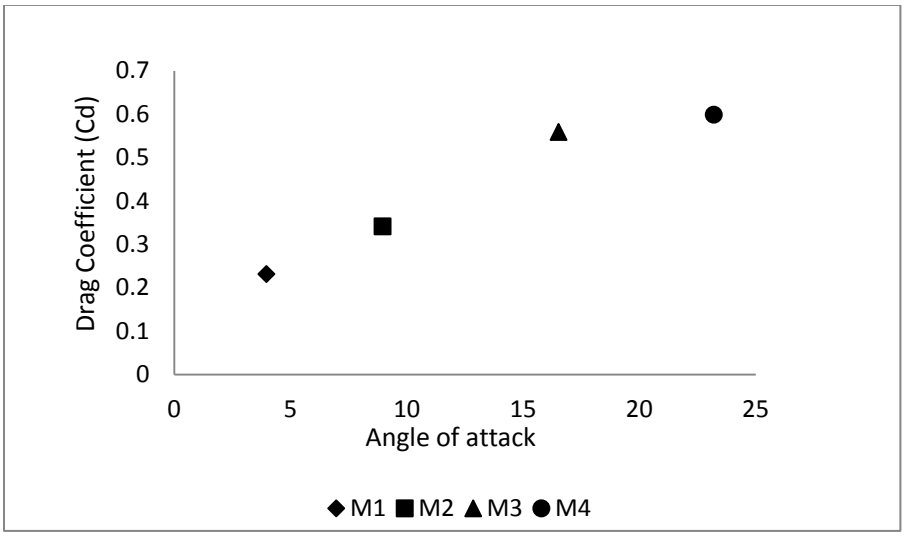

Figure 47. Comparison of the empty shroud drag coefficient against angle of attack

Figure 48 shows the drag coefficient corresponding to shroud model area ratio. As mentioned previously, increasing the frontal area causes enormous drag force on the shroud and since the difference between the throat area and exit area (represented by frontal area) increased, the drag coefficient maximized. In the figure, it is noticed that there is a difference in drag coefficient between model M4 and M5 even though they have the same area ratio. The reason is that model M4 has a higher-pressure drag because it has a higher angle of attack. In contrast,

the pressure drag is lower on the surface of model M5 which has lower angle of attack. Comparing between these models' sizes, the pressure drag is much more influential than friction drag.

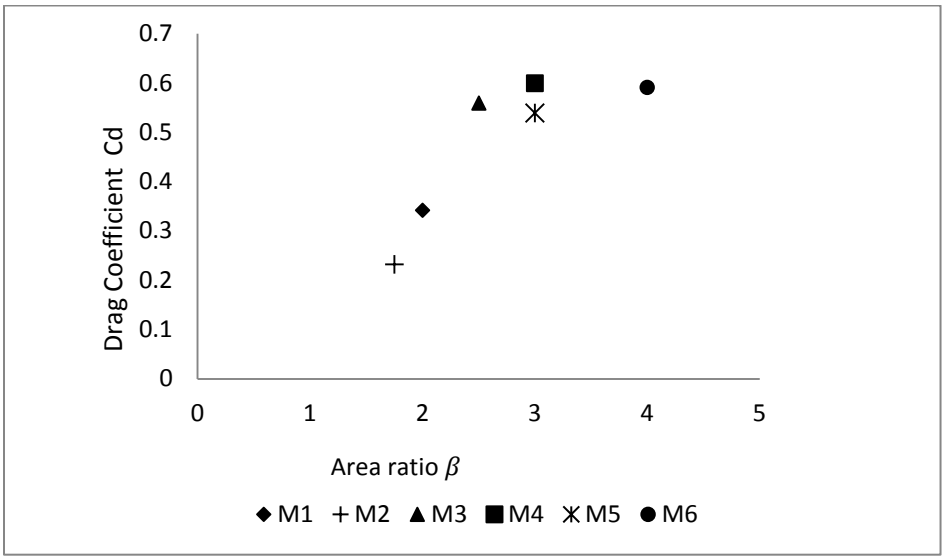

Figure 48. Drag coefficient of empty shroud against area ratio**,** for the six Models

The interrelationship between the drag coefficient and length ratio is illustrated in Figure 49. The drag coefficient increased with extending the shroud length and also area ratio because the friction drag on the surface has been increased. Model M6 that has the greatest length ratio (L/R_{th}=3.769), has larger drag coefficient of 0.59, compared to model M1.

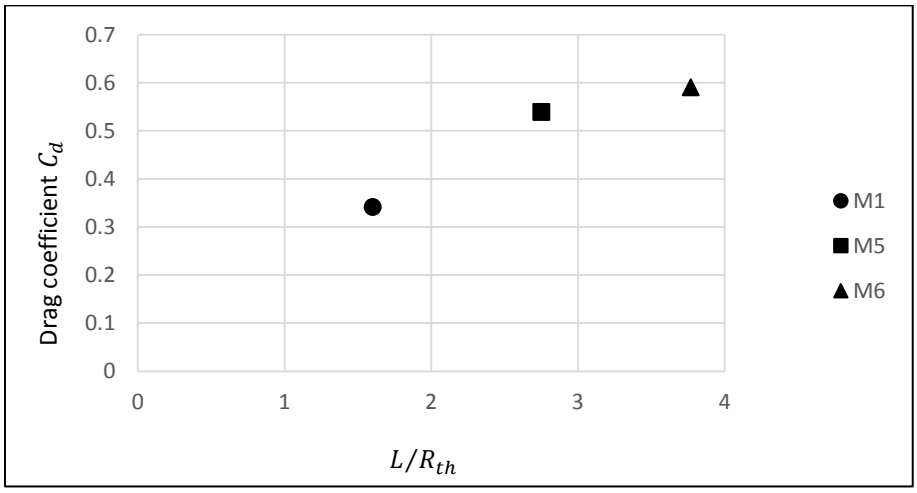

Figure 49. The shroud length ratio versus drag coefficient of the M1, M5, and M6

3.5.6. Grid Convergence

The numerical results for all of augmentation velocity factor AF0, back pressure ratio γ, and drag force were validated with changing the mesh size. The grid convergence simulations were conducted in order to determine an appropriate grid size that balanced accuracy with practicality. The mesh would become finer as the volumes of the elements (cells) become smaller, and thus the error in the discrete results would be reduced. However this increases the computer processing time, sometimes prohibitively. Therefore, three different grid types were taken for each of six models.

The comparison was done based on analysis time and solution convergence, and also the percentage of errors of Grid1 and Grid2 with respect to a very fine mesh Grid3. The Grid2 showed a decrease in the computer processing time and at the same time, the solution reached the convergence with acceptable number of iterations. However, the Grid1 and Grid3 generally showed an increase in analysis time and required a greater number of iterations to reach the convergent solution, which led to an increase in the processing time. Thus, the characteristics of Grid2 were used for all of the final models, as shown in Table 7.

Table 7. Geometry and Grid information for convergence of Grid2

Grid2				
Models	# of Nodes	# of Elements	Run Time (min)	# of Iterations
M1	58432	113698	14.28	1472
M2	52757	101704	9.1	1423
M3	51624	100100	17	1083
M4	67675	130868	19	2153
M5	71265	139385	20	2008
M6	73863	144603	22	2100

3.5.7. Mathematical Power Calculations using CFD Results

The PV-curves of the six models and bare wind turbine were obtained from the mathematical modeling employed by Van Bussel (1999). The power equation can be easily found using the power coefficient C_p definition as mentioned previously and by applying the difference pressure equation right before (p_2) and after (p_3) the shroud throat. The power coefficient for SAWT becomes:

$$C_{p,rotor} = \frac{(p_3 - p_2)V_2}{\frac{1}{2}\rho V_0^3} = \beta\gamma 4a(1-a)^2 \tag{3.28}$$

And consequently the power coefficient based upon the diffuser exit area:

$$C_{p,exit} = \gamma 4a(1-a)^2 \tag{3.29}$$

From Equations 3.28 & 3.29, a good relationship is obtained between power coefficients at the throat and exit area:

$$\beta = \frac{C_{p,rotor}}{C_{p,exit}} \tag{3.30}$$

An important conclusion can be seen in Equation 3.28; the power coefficient for bare wind turbine can be found by setting $\beta\gamma = 1$.

Thus the generated power can be written:

$$P = \frac{1}{2}\rho A_r V_0^3 C_{p,rotor} \tag{3.31}$$

Where ρ is air density, A_r is the rotor swept area, V_0 is the undisturbed air velocity, and $C_{p,rotor}$ is the power coefficient for the rotor in the shroud calculated from Equation 3.28. The back pressure ratios (γ) were calculated as result of average air velocity at the exit plane of the shroud to the undisturbed air velocity from CFD analysis as shown previously in Table 5.

Figure 50 shows the variation of the output power versus the inlet air velocity using Equations 3.28 and 3.31. Note the nonlinear increase between inlet velocities of 5 m/s to 30 m/s.

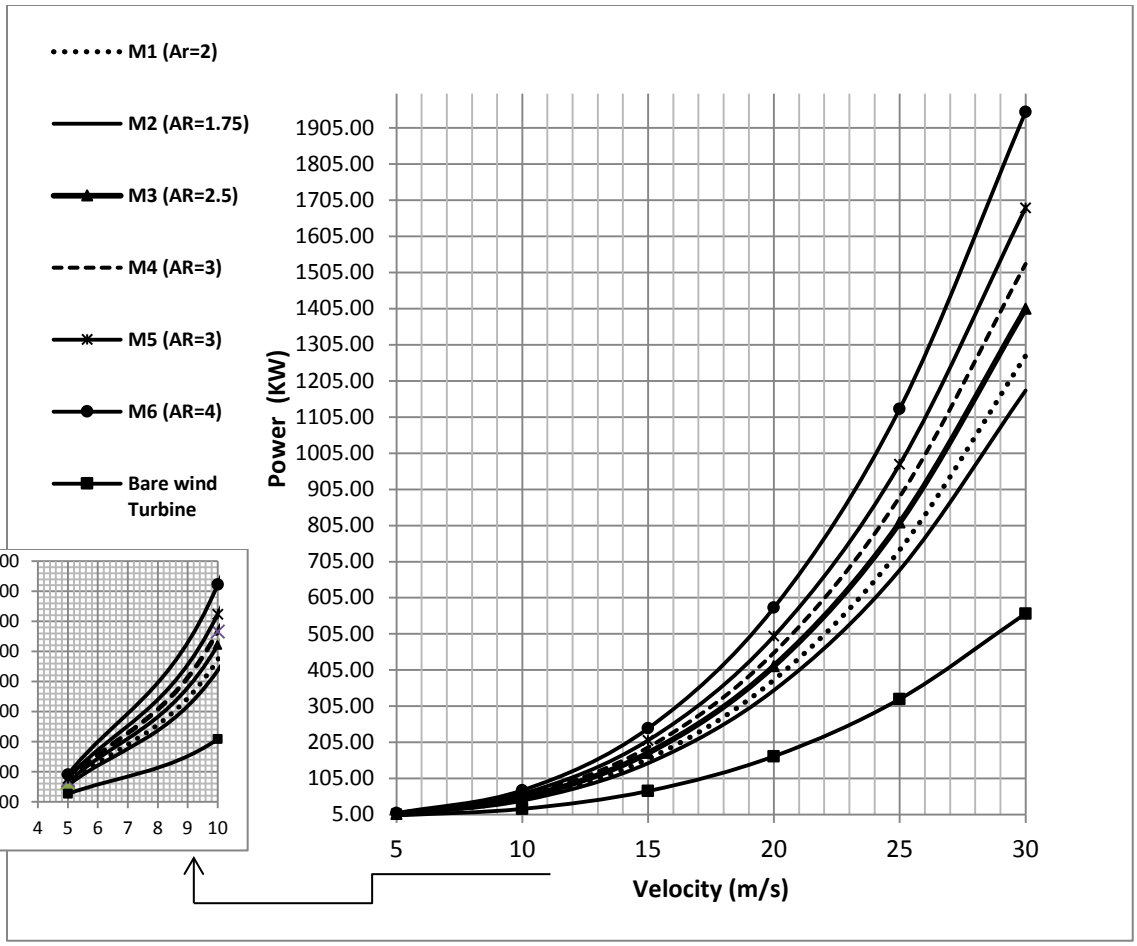

Figure 50. Output power versus inlet air velocities for the six models and bare wind turbine.

In Table 8, the maximum output power was achieved in model M6 since it has the highest area ratio of 4. The power of model M6 was approximately 3.5 times compared to bare wind turbine. While the power in model M1 (area ratio of 2) was 2.3 times that of a bare wind turbine. According to PV-curves, it seems clear that the output power increases with increasing shroud area ratio, even though there was a slight effect of back pressure. For instance, the difference in back pressure ratio γ between model M2, that has less separated layers, and the one of model M1 was 0.065. Furthermore, the difference is 0.3 between model M1 and M6, and in this case the difference in back pressure ratio γ did not have a big effect on the output power compared to the area ratio effect. However, the output power performance is dependent upon the shroud efficiency (velocity augmentation factor AF0). The more air mass that was pulled inside the shroud, the much better power output was obtained, as discussed previously.

Table 8. Mathematical calculations of output power of the six models and a bare wind turbine

Inlet Velocity (m/s)	Power_M1 (KW) (ratio=2.27)	Power_M2 (KW) (ratio=2.1)	Power_M3 (KW) (ratio=2.5)	Power_M4 (KW) (ratio=3)	Power_M5 (KW) (ratio=3)	Power_M6 (KW) (ratio=3.47)	Bare Wind Turbine
5	5.90	5.46	6.50	7.08	7.80	9.03	2.60
10	47.21	43.65	52.04	56.62	62.38	72.20	20.79
15	159.33	147.31	175.62	191.08	210.53	243.69	70.17
20	377.67	349.18	416.29	452.94	499.05	577.64	166.33
25	737.64	681.99	813.06	884.65	974.70	1128.20	324.87
30	1274.64	1178.49	1404.97	1528.67	1684.28	1949.53	561.37

The induction factor (a) in Equation 3.28 was considered as optimum factor of 1/3 for the power calculations in Table 3.8 to give an optimum power coefficient with Betz limit of 16/27. Also, Figure 51 shows power coefficients C_p with various induction factors. It is clear that all models are higher than Betz limit of a bare wind turbine. Model M6 has the maximum power coefficient since it has the highest area ratio.

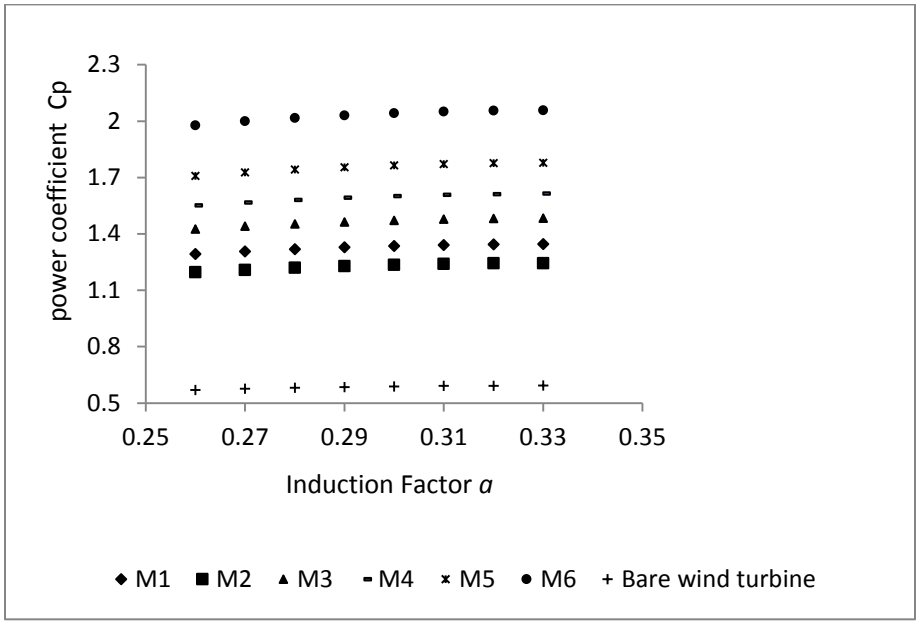

Figure 51 Power coefficients of six models versus different induction factors a

3.5.8. Experimental Power Calculations using Wind Tunnel Micro-Shroud

Since the appropriate tools for 3D simulation of entire shrouded wind turbine's system were not available, power was validated by experimental work only. Table 9 shows the experimental results of the power measurements for both the shrouded wind turbine and the bare wind

turbine. Different multi-meters were used in this experiment which allowed measurements of the voltages and the currents by taking the mean values between the maximum and minimum readings. A remarkable increase in the output power in Shroud Augmented Wind Turbine was observed, approximately 1.6-2.2 times that of a bare wind turbine.

Table 9. Experimental measurements of the extracted power

Bare wind Turbine (Non-shrouded)				Shrouded Wind Turbine(SAWT)			
Mean Velocity (m/s)	Voltage (V)	Current (mA)	Power (W)	Voltage (V)	Current (mA)	Power (W)	Ratio (P_{shroud}/P_{bare})
9.32	18.2	12.6	0.231	21.35	24.8	0.531	2.3
9.81	19.45	16.25	0.318	22.95	29.7	0.683	2.14
10.19	20.75	21.05	0.4988	23.9	36.3	0.868	1.98
10.58	21.95	29.45	0.73644	25.2	44	1.109	1.71
11	24.1	30.1	0.8109	27.3	50.15	1.373	1.88

Also, Figure 52 shows clearly the difference between two cases. The mean velocity was the average velocities that were taken just 5 inches in front of the test section.

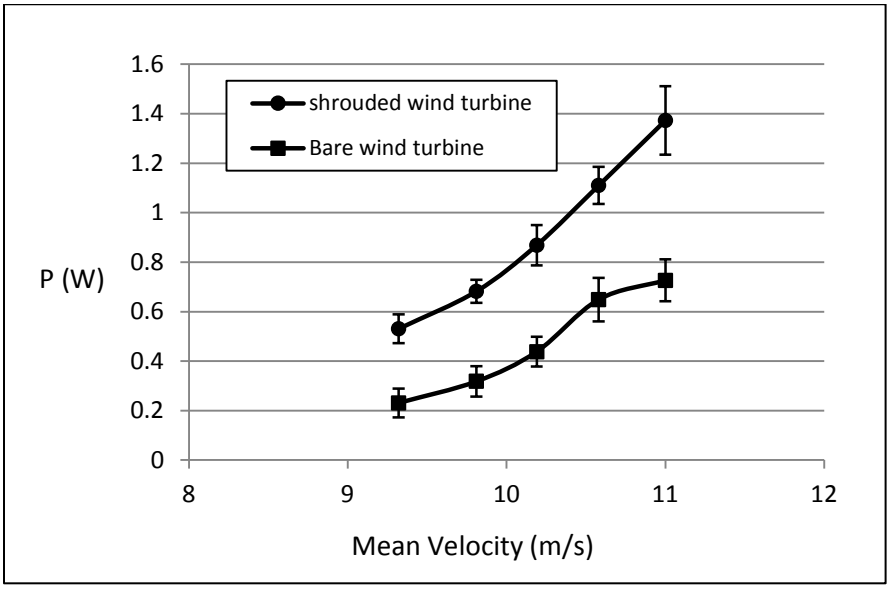

Figure 52. Experimental comparison between shrouded wind turbine and bare wind turbine

Since the optimum power coefficient C_p for the bare wind turbine is 0.59 (at a =1/3) for a very large scale, it is not practical to consider this value for micro wind turbine (it has to be so small). It was difficult to compare the mathematical results for the power with the experimental result of the micro-wind turbine for both cases because the test conditions were not the same as the

mathematical calculations. There were many factors that influence the turbines' performance including blade profile, which was chosen randomly (not part of research topic), size of the blade diameter, swept area, and the number of the blades used in experiment. Thus, the goal of this experiment was to focus only on the power generated by the bare wind turbine and SAWT in a real world experimental environment. In this case the Shroud Augmented Wind Turbine fully out-performed the bare Wind Turbine and caused great anticipation of the Shrouded Turbine to be installed at Youngstown State University.

3.5.9. Final Thoughts on the Shrouded Wind Turbine Research Section

The computational analysis and wind tunnel experiments on special design of shrouded wind turbine had been carried out to achieve a better understanding of the effect of the air distribution at the throat area of empty shroud and consequently the augmented power. Augmentation velocity factor of six different models was sought in this study and the results of CFD analysis showed good performance when the area ratio is increased at appropriate angles of attack. In this study, the shroud E423 of model M1 (area ratio of 2) proved to be the acceptable design generating good power with less cost caused by drag force, when compared to other shrouded models studied.

The optimum model (model M1, area ratio of 2) has less augmentation velocity factor (AF0=1.9) and less output power, compared to Model M5 and M6, but Model M1 has significantly less drag force coefficient ($C_d = 0.34$) which reduces the cost effect on the shroud price. In addition, the numerical analysis results on empty models showed a decrease in back pressure ratio in the model M5 ($\gamma = 1$) and M6 ($\gamma = 0.86$). However, the back pressure ratio in model M1 was ($\gamma = 1.135$) which is higher than that in the model M5 and M6. In fact, the reduction in back pressure γ is caused by the flow separation that occurred in the outlet area of the shroud. This flow separation at all of the model M3, M4, M5, and M6 makes the Kutta condition not completely satisfied compared to model M1 which has been shown that Kutta condition was completely satisfied.

The velocity distribution inside empty shroud E423 obtained from CFD with the proposed model M1 presented excellent agreement with experimental work. In fact the velocity profile matched with the experimental data at the throat area of empty shroud model M1 with error less than 1.06% of the augmentation factor.

The experimental results on micro–wind turbine showed an increase in the output power by approximately 2.2 times with the turbine placed inside the shroud of model M1 (Area ratio of

2), compared to the performance, found in the bare wind turbine. According to the mathematical calculations, the power can be maximized about 3.5- 4 times using model M6 of higher area ratio of 4.

According to the drag force analysis of empty shroud models, the shrouded wind turbine must be designed to survive an extreme wind gusts that are many times greater than normal wind speeds. Shrouded Augmented Wind Turbines require an enhanced structure and strength foundation, compared to the bare wind turbine that is shroud-less. The model M1, selected to be optimum, has a reasonable drag force coefficient and good output power. Model M6, while having better output power, has much greater drag load on its body. In reality, the high loads caused by drag force will add more cost.

3.6.Full Scale Wind Turbine at YSU

3.6.1. Foundation Analysis and Work

Before the full scale shrouded wind turbine could be installed. Foundation work was required. Professional Service Industries, Inc. (PSI) was contracted by Green Energy Technologies to complete an exploration and evaluation of the subsurface for the proposed wind turbine to be located at the southeast corner of the intersection of Wick Avenue and Interstate 422, in the City of Youngstown, Mahoning County, Ohio. The proposed 25 kW wind turbine is estimated to be about 92 feet in height. The maximum vertical structural load will be 12,000 pounds.

One soil boring was drilled and selected soil samples tested in the laboratory. At the location, topsoil was encountered having a thickness of about four inches. Topsoil thickness should be expected to vary across the site. Beneath the overlying topsoil, fill materials consisting of sand with gravel containing variable fractions of slag, concrete, and red brick fragments were encountered to a depth of about 8.9 feet below the existing surface grades. Beneath the fill materials, natural soils consisting of sandy silt clay with traces of rock fragments were encountered to a depth of about 18.5 feet below the existing surface grades. Underlying the natural soils, bedrock was encountered consisting of gray, weathered shale to the terminal depth of the test boring location. No groundwater was encountered during the field drilling operation at test boring location.

Based on site conditions, PSI recommended that the proposed wind turbine can be supported on drilled shaft/caisson foundations bearing within the area's bedrock formation. It was anticipated that the drilled shaft foundation design be governed by resistance to shear, uplift, and overturning moment forces. The caisson was adequately reinforced for the design lateral

loads. The drilled shaft/caisson was designed with an ultimate side friction and net allowable tip bearing pressure presented in Table 10.

Table 10. Drilled Shaft Foundation Design Parameters at Boring Location

Depth (feet)	Shear Strength		Lateral Modulus, k (pci)	Ultimate Side Friction Capacity (PSF)	Ultimate End Bearing Pressure (PSF)	Strain Factor, E_{50}
	ϕ (degrees)	C (PSF)				
0-9	Neglect	Neglect	Neglect	Neglect	Neglect	---
9-18.5	---	4,000	400	1,800	10,000	0.005
18.5-39	---	8,000	800	3,000	20,000	0.004

Once the soil analysis came back satisfactory (with the exception of needing a thicker than anticipated footer) the foundation was poured and the site was ready for a turbine, Figures 53-55.

Figure 53. Foundation Preparation for Shrouded Wind Turbine

Figure 54. Foundation Preparation for Shrouded Wind Turbine

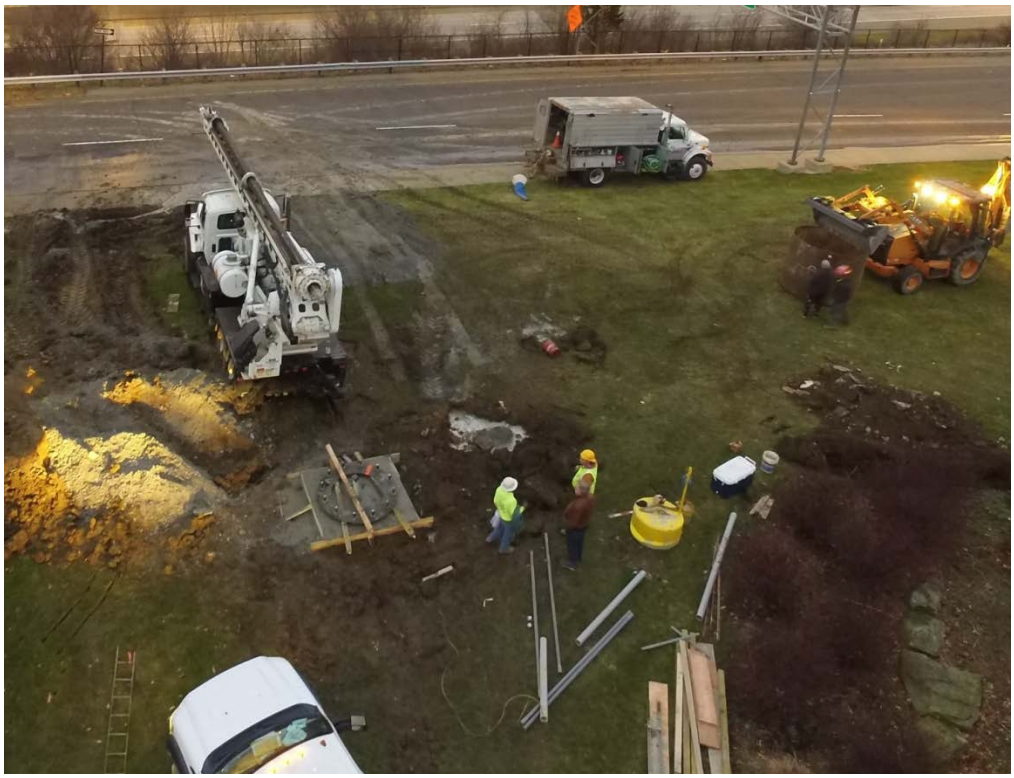

Figure 55. Foundation Preparation for Shrouded Wind Turbine

3.6.2. The Shroud Augmented Wind Turbine – The Wind Sphere

With the foundation poured as shown previously, all indications were given that the turbine would be operational at the beginning of 2016. While all the components and permits were complete, the company manufacturing the wind turbines decided that it was important to conduct more in house testing. This shrouded turbine is the first of its kind to be built in the United States. Figure 56 shows the nacelle going through the final testing procedure in early spring 2016.

Figure 56. Final Testing of Wind Turbine Nacelle

The shrouded wind turbine was then temporarily erected at a height of 20 feet in order to ensure that the system would operate as expected. Figure 57 shows the installation at this height. A video of the turbine operating was uploaded to the EERE-PMC web site as well. The test operation was a success and it was reported to have cut-in speeds as low as 1.5 mph wind speed.

Figure 57. Cut-In Speed Testing of Wind Sphere

The Wind Sphere was finally erected on the Youngtown State University site in Fall 2016. The true measure of its effectiveness is of course analysis of the collected data. There were electrical issues that needed to be resolved and there seems to still be issues with the data collection today as the results are not favorable for the augmented performance. Engineers from Green Energy Technologies are working to figure out these issues. The following is a report of the preliminary performance of the Wind Sphere. The format of this section (3.6.3) is altered because the performance report was simply copied into this report.

3.6.3. The Wind Sphere Performance

This test is being conducted as part of the U.S. Department of Energy's (DOE) TechBelt Energy Innovation Center (TBEC) project. This project was established to study how shrouded wind turbines performed in low wind speed areas. One turbine is being tested at Youngstown State University (YSU) as part of this project. The main focus of this testing is on the wind turbine's power curve and power coefficient data.

1. Test Summary

Figures 1 and 2 are a summary of the results of a power performance test that YSU conducted on the Wind Sphere 25 kW small wind turbine. For this test the Wind Sphere 25 kW turbine was installed at Melnick Hall, YSU in Youngstown, OH.

In the following summary sea-level air density normalization was not accounted for due to negligible elevation differences. This summary contains two sets of data, one of which was collected from 3/01/2017 – 3/20/2017 and the other was collected from 4/23/2017 – 5/05/2017. In all YSU collected and analyzed a total of approximately 768 hours of data. The bin which had the most data for the first time period was 8 mph and the bin that had the most data for the second time period was 11 mph.

Power Performance Test
Wind Sphere 25 kW

Sea-Level Air Density assumed for Cp

Turbine Specificiations

Rated Power:	25	kW
Cut-in Wind Speed:		
Cut-out Wind Speed:		
Rated Wind Speed:		
Rotor Diameter:		

Site Conditions:

Location:	YSU, Youngstown, OH	
Air Density:	1.225 (assumed)	kg/m^3

Total Statistics:

Start Date:	1-Mar-17	
End Date:	5-May-17	
Amount of Data Collected:	768 (approx)	hours
Highest Bins Filled:	8 & 11	mph

From 3/01/17 to 3/20/17			
Bin Wind Speed (mph)	Number of Data Points	Bin Power (kW)	Cp
0	1	0.00	0.00
1	2	0.00	0.00
2	10	0.00	0.03
3	53	0.08	0.99
4	108	0.25	1.23
5	172	0.48	1.24
6	203	0.76	1.12
7	202	0.90	0.84
8	204	1.41	0.88
9	186	1.25	0.55
10	166	1.61	0.51
11	149	2.04	0.49
12	116	3.07	0.57
13	99	4.02	0.58
14	84	5.29	0.62
15	57	7.05	0.67
16	26	8.39	0.65
17	21	7.72	0.50
18	8	8.97	0.49
19	4	5.88	0.27
20	4	6.03	0.24
21	2	0.02	0.00
22	3	2.14	0.06
23	3	0.00	0.00
24	1	0.00	0.00
25	3	0.81	0.02

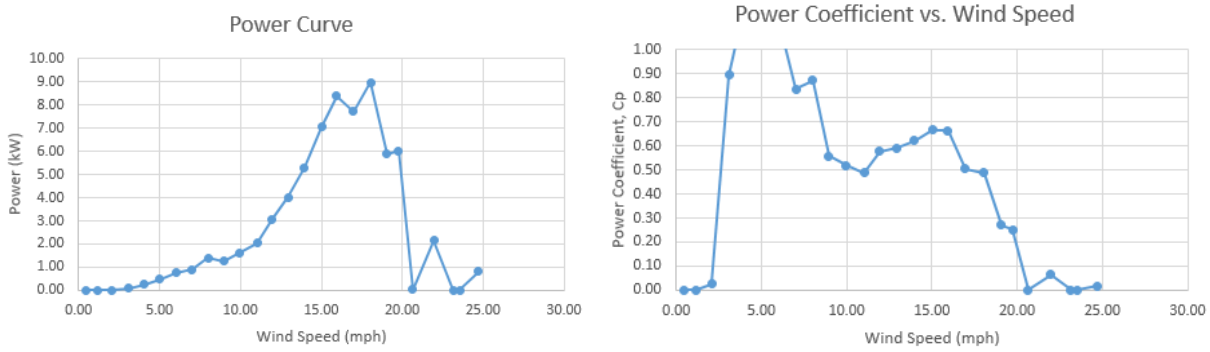

Figure 1: Data from 3/1 to 3/20/17

From 4/23/17 to 5/5/17			
Bin Wind Speed (mph)	Number of Data Points	Bin Power (kW)	Cp
1	0	0.00	0.00
2	6	0.00	0.02
3	40	0.03	0.31
4	61	0.06	0.30
5	90	0.14	0.37
6	90	0.21	0.31
7	122	0.28	0.26
8	138	0.46	0.29
9	180	0.79	0.35
10	195	1.28	0.41
11	201	2.15	0.52
12	161	3.35	0.62
13	97	4.19	0.61
14	80	5.25	0.61
15	56	6.62	0.63
16	30	7.50	0.58
17	23	7.99	0.52
18	12	7.00	0.38
19	8	5.81	0.27
20	2	9.80	0.39
21	7	9.31	0.32
22	4	2.59	0.08
24	3	1.28	0.03
31	1	1.27	0.01

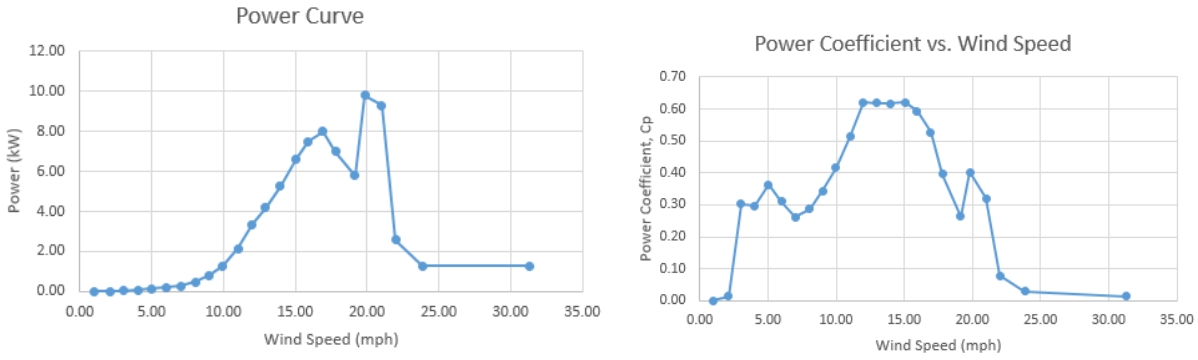

Figure 2: Data from 4/23 to 5/5/17

2. Test Turbine Configuration

Rotor Diameter (ft)	28
Hub Height (ft)	91
Rated Electrical Power (kW)	25
Rated Wind Speed (mph)	21
Max Rotor Speed (rpm)	125
Number of Blades	3

Table 1: Test Turbine Configuration

3. Test Site Description

The test turbine is located on the northeast corner of YSU's campus. The terrain consists of surrounding trees, buildings, a highway overpass, as well as variations in elevation.

4. Description of Data Collected

Data was collected for the following categories: date, time, wind speed, average wind speed, wind direction, average wind direction, turbine speed, average volts, average current, meter power, kWh for a month, kWh for a year. The data collection equipment was located on the mast of the wind turbine behind the turbine.

5. Test Results

5.1 Tabular Results of the Power Performance Test

There may have been some errors in the data collection, one of the main issues noticed was multiple zero values for turbine speed and power when it appeared there shouldn't have been. Tables 2 through 5 list the power performance results. Table 2 shows the binned power performance results including all zero data values for the time period 3/1 -3/20/17 and Table 3 shows the binned power performance results through this same time period without including all of the zero data. Table 4 shows the binned power performance results including all zero data values for the time period 4/23 -5/5/17 and

Table 5 shows the binned power performance results through this same time period without including all of the zero data.

From 3/01/17 to 3/20/17

Bin No.	Norm./Ave. Wind Speed (mph)	Hub Height Wind Speed (mph)	Number of Data Sets (10 min. avg.)	Turbine RPM	Norm./Ave. Meter Power (kW)	Cp
0	0.45	0	1		0.00	0.00
1	1.17	1	2		0.00	0.00
2	2.05	2	10		0.00	0.03
3	3.10	3	53		0.08	0.90
4	4.05	4	108		0.25	1.19
5	5.01	5	172		0.48	1.23
6	5.99	6	203		0.76	1.13
7	7.00	7	202		0.90	0.84
8	8.01	8	204		1.41	0.87
9	8.95	9	186		1.25	0.56
10	9.95	10	166		1.61	0.52
11	11.02	11	149		2.04	0.49
12	11.93	12	116		3.07	0.58
13	12.95	13	99		4.02	0.59
14	13.95	14	84		5.29	0.62
15	15.01	15	57		7.05	0.67
16	15.92	16	26		8.39	0.66
17	16.96	17	21		7.72	0.51
18	18.05	18	8		8.97	0.49
19	19.04	19	4		5.88	0.27
20	19.75	20	4		6.03	0.25
21	20.63	21	2		0.02	0.00
22	21.97	22	3		2.14	0.06
23	23.14	23	3		0.00	0.00
24	23.55	24	1		0.00	0.00
25	24.69	25	3		0.81	0.02

Table 2: Performance chart including all zero values.

From 3/01/17 to 3/20/17

Bin No.	Norm./Ave. Wind Speed (mph)	Hub Height Wind Speed (mph)	Number of Data Sets (10 min. avg.)	Turbine RPM	Norm./Ave. Meter Power (kW)	Cp
3 Average	3.25	3	3	23.65	0.45	4.21
4 Average	4.13	4	64	26.12	0.44	2.00
5 Average	5.06	5	166	25.57	0.49	1.21
6 Average	5.96	6	198	32.83	0.72	1.09
7 Average	7.02	7	195	39.41	0.99	0.91
8 Average	7.99	8	220	43.61	1.34	0.84
9 Average	8.95	9	167	46.39	1.25	0.56
10 Average	9.95	10	180	50.52	1.64	0.53
11 Average	11.00	11	133	52.57	2.10	0.50
12 Average	11.96	12	126	54.20	3.02	0.56
13 Average	12.97	13	98	57.84	4.21	0.62
14 Average	13.91	14	75	62.28	5.55	0.66
15 Average	14.96	15	55	66.54	6.84	0.65
16 Average	15.87	16	37	70.98	8.07	0.65
17 Average	17.01	17	15	74.80	9.23	0.60
18 Average	18.06	18	3	77.67	10.21	0.55
19 Average	19.07	19	4	77.20	10.94	0.50
20 Average	20.05	20	2	80.45	11.99	0.48

Table 3: Performance chart excluding all zero values.

From 4/23/17 to 5/5/17

Binned No.	Wind Speed	Wind Speed Ave. (mph)	Number of Data Sets (10 min. avg.)	Wind Direction	Wind Direction Ave.	Turbine RPM	Volts	Current	Meter Power	kWh Month	kWh Year	Cp
1 Average	0.97	0.97	0	162.70	166.57	0.00	486.20	0.00	0.00	821.67	2893.67	0.00
2 Average	2.10	2.08	6	147.37	145.50	0.03	485.08	0.00	0.00	803.03	2897.25	0.01
3 Average	2.98	3.01	40	135.77	127.88	1.46	484.80	0.13	0.03	729.11	2888.56	0.30
4 Average	4.02	4.03	61	123.36	117.89	5.18	484.79	0.33	0.06	708.02	2878.80	0.30
5 Average	5.03	5.02	90	126.83	122.68	18.98	484.60	0.81	0.14	690.43	2910.59	0.36
6 Average	6.00	6.01	90	130.28	125.15	32.78	484.39	1.13	0.21	680.08	2926.96	0.31
7 Average	7.01	7.00	122	143.37	142.24	44.78	484.72	1.34	0.28	629.23	2952.46	0.26
8 Average	8.02	8.03	138	150.27	148.88	54.39	484.51	1.52	0.46	566.44	2969.35	0.29
9 Average	9.02	9.02	180	168.85	169.68	58.30	484.38	1.73	0.79	500.72	2992.15	0.34
10 Average	9.98	9.96	195	169.90	170.82	61.09	483.64	2.14	1.28	457.74	2980.88	0.42
11 Average	11.04	11.02	201	177.31	176.28	64.05	483.69	2.98	2.15	469.94	2961.59	0.51
12 Average	12.08	11.99	161	183.88	183.92	66.76	483.65	4.28	3.35	447.37	2950.12	0.62
13 Average	12.96	12.93	97	202.47	202.64	68.48	483.47	5.23	4.19	457.27	2940.44	0.62
14 Average	13.92	13.96	80	216.59	215.37	68.50	484.40	6.43	5.25	408.76	2972.88	0.62
15 Average	14.89	15.04	56	227.34	228.05	72.95	484.12	8.06	6.62	322.76	2987.43	0.62
16 Average	15.68	15.91	30	233.21	233.50	69.85	485.70	9.01	7.50	335.95	2987.73	0.59
17 Average	17.04	16.92	23	252.03	252.90	69.08	487.80	9.54	7.99	289.06	3027.81	0.53
18 Average	17.47	17.81	12	270.23	271.14	57.37	485.88	8.37	7.00	206.17	3056.04	0.40
19 Average	18.50	19.15	8	252.08	263.97	41.78	484.96	6.87	5.81	103.38	3064.38	0.26
20 Average	19.48	19.83	2	259.05	263.90	71.03	487.19	11.66	9.80	112.01	3073.01	0.40
21 Average	20.88	21.02	7	256.36	258.69	61.18	486.76	11.01	9.31	107.05	3068.05	0.32
22 Average	22.87	21.99	4	253.89	253.10	18.60	484.38	3.10	2.59	78.87	3039.87	0.08
24 Average	23.58	23.85	3	266.79	273.89	10.68	486.80	1.51	1.28	112.68	3073.68	0.03
31 Average	32.03	31.28	1	255.26	257.25	14.63	486.87	1.52	1.27	23.00	2984.00	0.01

Table 4: Performance chart including all zero values.

From 4/23/17 to 5/5/17

Binned No.	Wind Speed	Wind Speed Ave. (mph)	Number of Data Sets (10 min. avg.)	Wind Direction	Wind Direction Ave.	Turbine RPM	Volts	Current	Meter Power	kWh Month	kWh Year	Cp
4 Average	4.01	4.13	19	90.86	85.64	20.05	485.18	1.21	0.22	699.95	2,865.53	1.00
5 Average	5.02	5.10	55	127.76	123.40	29.68	485.01	1.31	0.24	698.45	2,915.92	0.57
6 Average	5.94	6.00	113	142.47	137.63	37.12	484.58	1.34	0.25	693.86	2,931.07	0.37
7 Average	7.01	7.05	141	140.30	137.42	47.25	484.25	1.42	0.31	626.96	2,944.85	0.29
8 Average	8.07	8.04	172	150.26	149.61	55.21	484.50	1.55	0.50	574.59	2,972.22	0.31
9 Average	9.00	9.01	189	168.77	169.05	58.26	484.49	1.72	0.76	481.12	2,993.39	0.33
10 Average	9.99	9.96	199	167.94	168.42	61.28	483.62	2.13	1.27	463.44	2,977.71	0.41
11 Average	11.00	10.95	158	184.13	184.25	63.94	483.80	2.92	2.10	461.62	2,966.86	0.51
12 Average	12.02	12.04	101	178.10	177.70	66.91	482.89	4.32	3.39	498.32	2,940.00	0.62
13 Average	13.03	12.95	86	199.54	199.83	68.49	484.74	5.21	4.19	416.32	2,953.49	0.62
14 Average	13.88	13.95	51	224.96	224.72	70.50	484.07	6.59	5.36	371.74	2,984.11	0.63
15 Average	14.81	14.99	35	223.39	222.74	73.04	484.25	8.15	6.71	350.02	2,980.82	0.64
16 Average	15.73	15.93	17	232.76	231.65	75.15	484.38	9.45	7.82	378.69	2,973.63	0.62
17 Average	17.11	16.90	16	242.41	243.63	78.56	487.23	11.48	9.63	273.38	3,012.13	0.64
18 Average	16.70	17.70	2	255.12	255.61	77.57	485.18	11.04	9.25	501.95	3,018.45	0.53
19 Average	19.35	18.89	4	257.54	258.81	80.76	487.32	13.00	10.92	111.06	3,072.06	0.52
20 Average	19.84	20.09	3	260.83	261.14	81.42	487.70	12.99	10.92	113.12	3,074.12	0.43
21 Average	21.03	20.72	1	267.40	268.73	84.25	485.74	14.85	12.46	112.80	3,073.80	0.45
22 Average	22.80	22.14	1	273.93	274.55	93.28	489.90	17.94	15.21	118.45	3,079.45	0.45
23 Average	22.58	22.57	1	235.87	233.87	84.82	487.73	16.29	13.74	92.00	3,053.00	0.38

Table 5: Performance chart excluding all zero values.

5.2 Graphical Results of the Power Performance Test

Figures 3 through 8 list the power performance results.

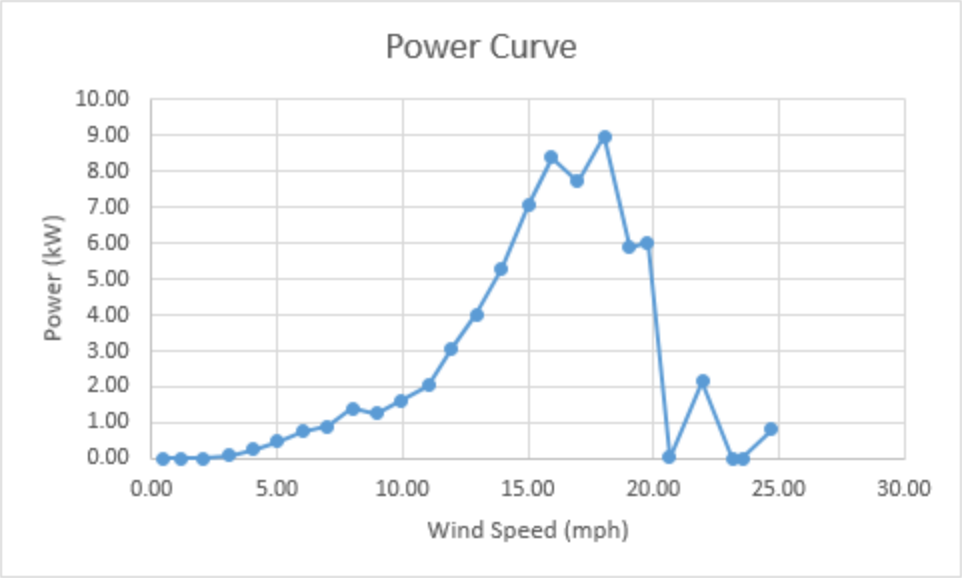

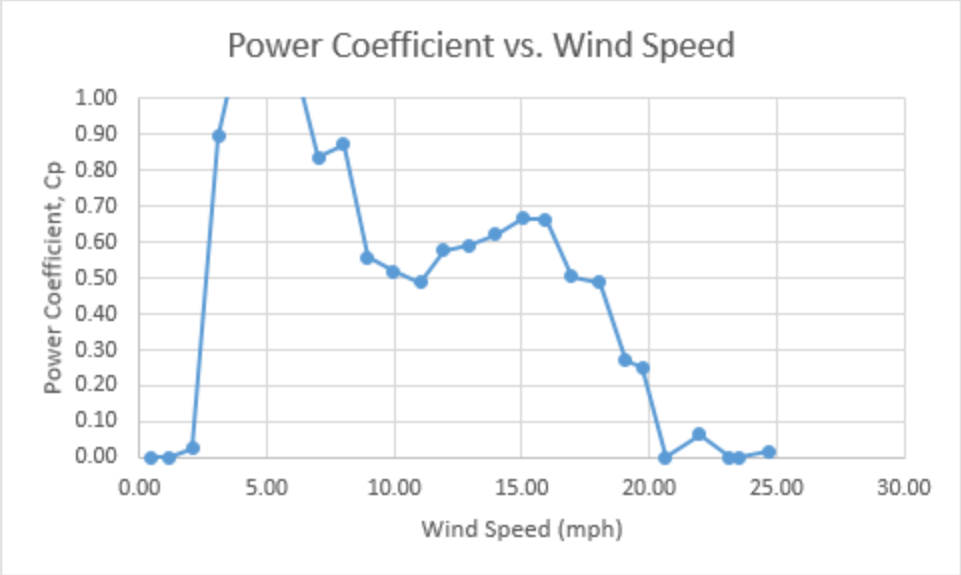

Figure 3: Power curve and Cp vs. wind speed graphs for 3/1 – 3/20/17 for all data points including zeros.

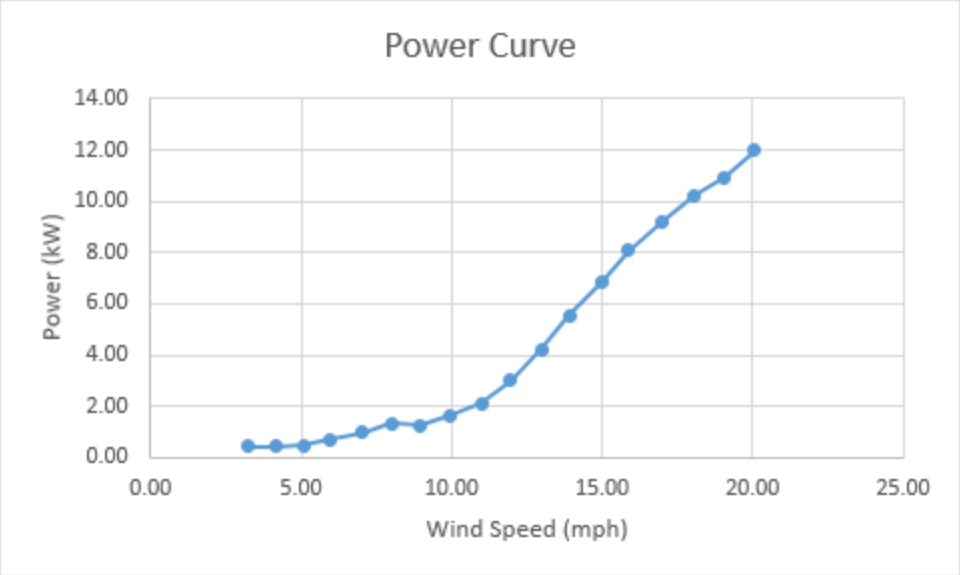

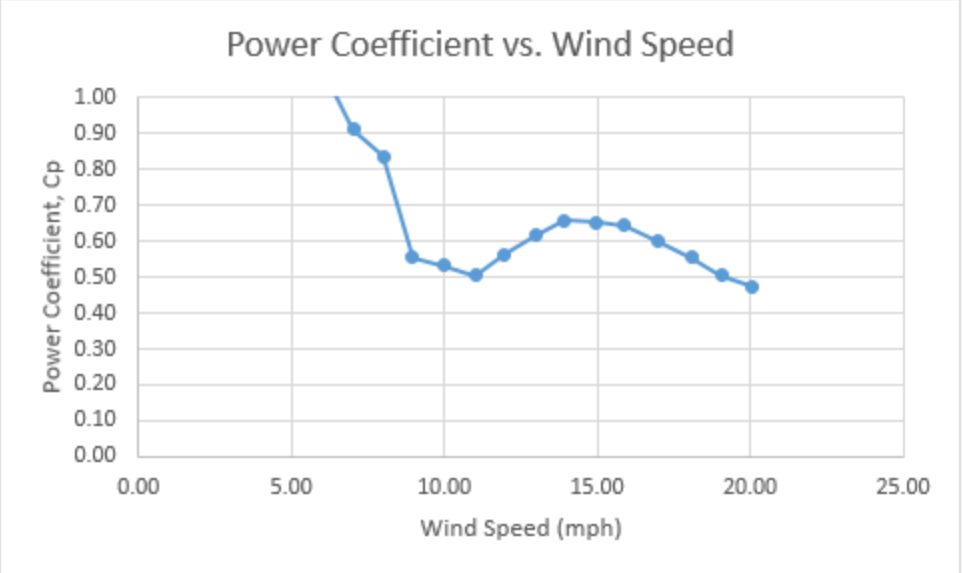

Figure 4: Power curve and Cp vs. wind speed graphs for 3/1 – 3/20/17 for all data points excluding zeros.

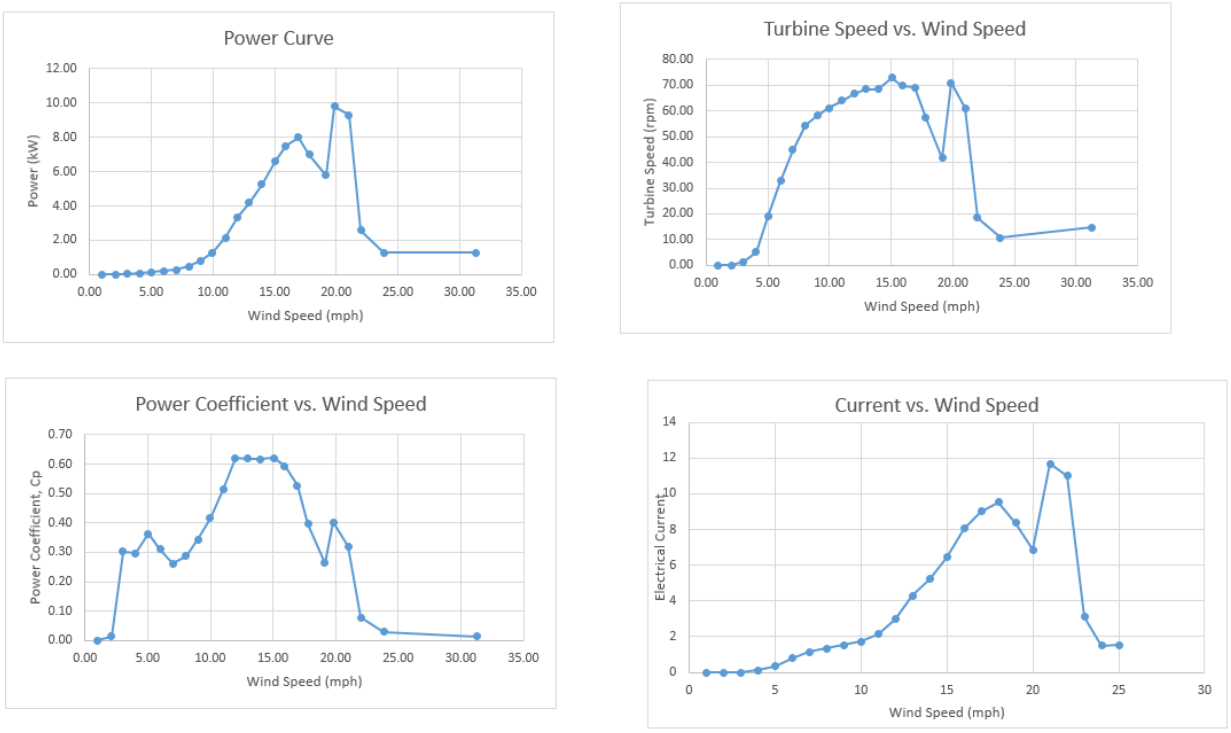

Figure 5: Various graphs for 4/23 – 5/5/17 for all data points including zeros.

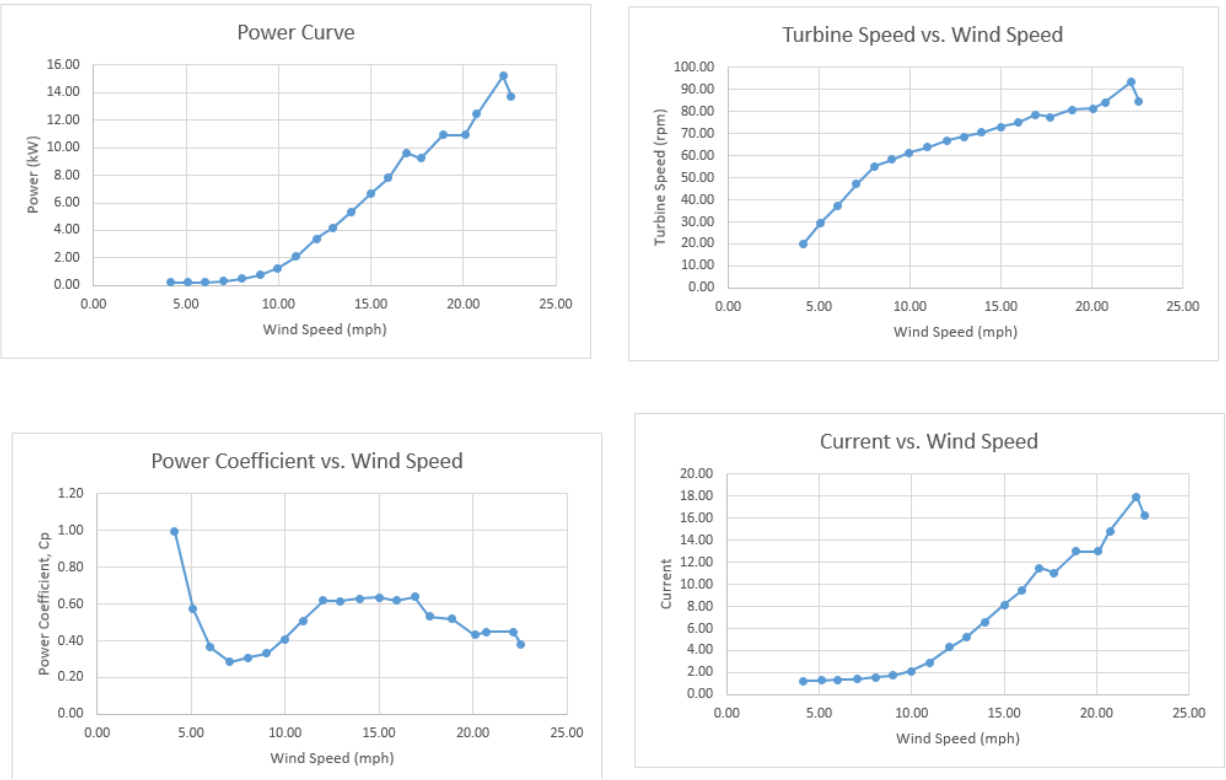

Figure 6: Various graphs for 4/23 – 5/5/17 for all data points excluding zeros.

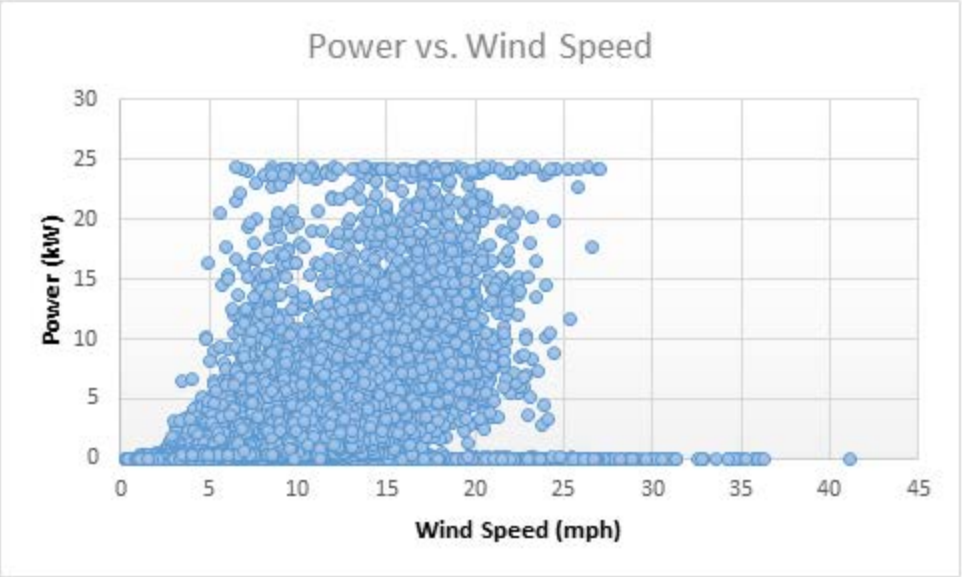

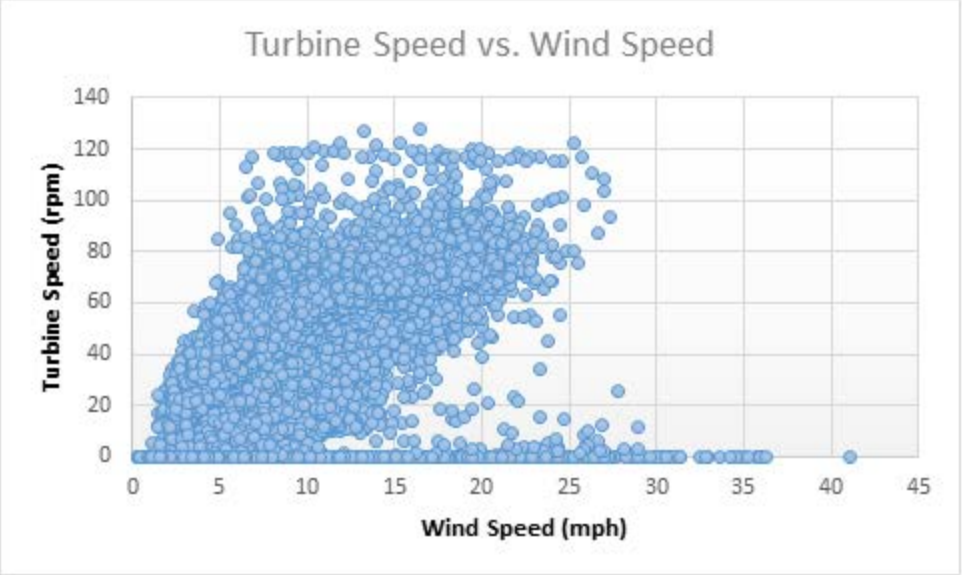

Figure 7: Power curve and turbine speed vs. wind speed graphs for 3/1 – 3/20/17 based off all non-averaged raw data.

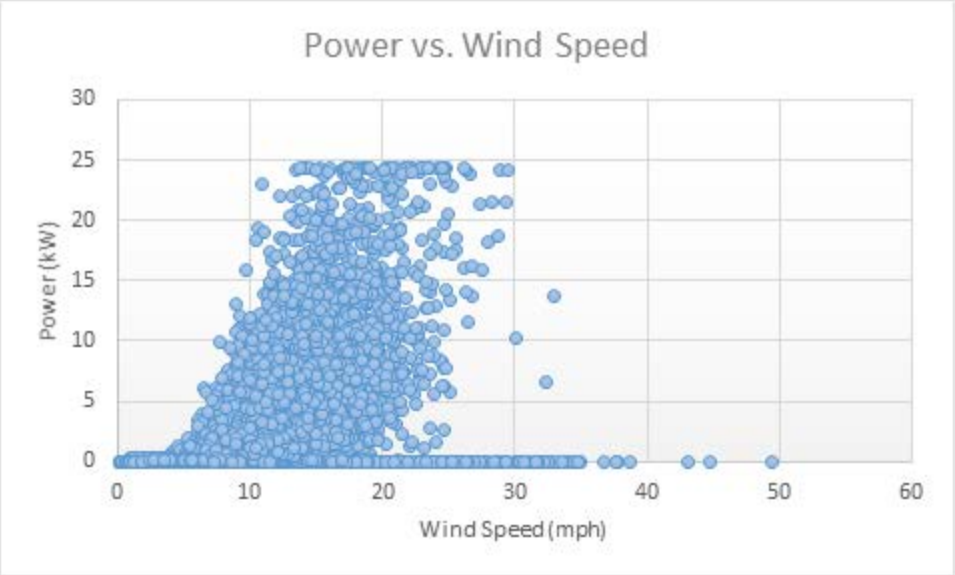

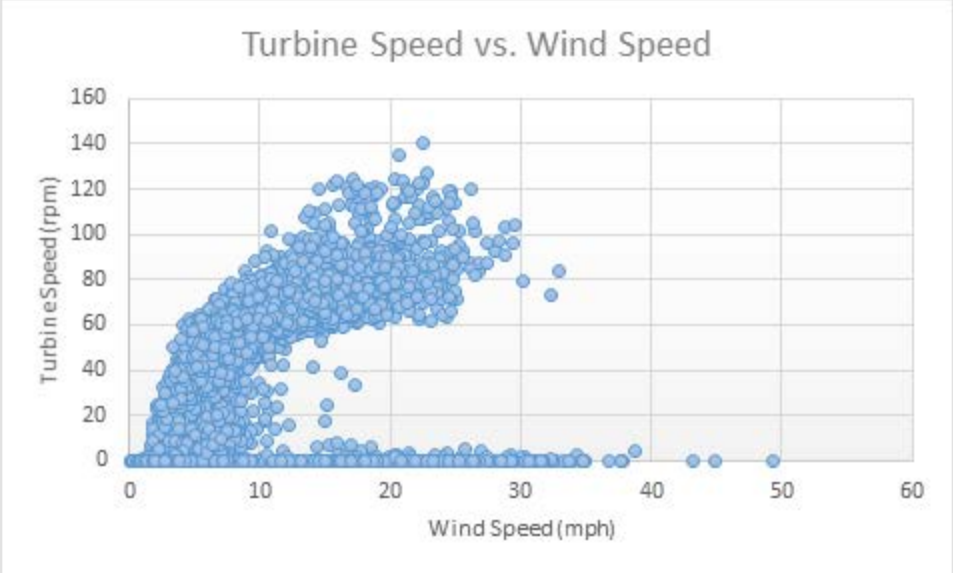

Figure 8: Power curve and turbine speed vs. wind speed graphs for 4/23 – 5/5/17 based off all non-averaged raw data.

6. Deviations and Expectations

There are various data that deviate from turbine specification expectations and realistic performance expectations in general. The power being produced by the turbine is generally low compared to the rated 25 kW at 21 mph, however the power coefficient values seem to be unrealistically high at the same time. It is possible that there may be same errors occurring in the data collection process. It has been observed when sifting through the raw data that there seems to be high variations between wind speeds and turbine speed as well as turbine speed and power being produced. This appears to occur within a window where the wind direction is not changing too drastically.

From a comparative standpoint to other turbines of similar size there is little published data other than manufacturer's flyers, which are rarely certified or follow any standards and are often idealized. This is because small wind turbines fall into a category that is not regulated for power curves by any organization. The power coefficient would be the main value to compare, where this number is based off of a ratio of how much power the turbine produces compared to how large the rotor diameter is (as well as wind speed and air density), or how efficient the turbine is at capturing available energy from the wind. The wind turbine being studied is showing efficiencies in the 60% and above range for lower wind speeds approximately 15 mph. This is very good considering most wind turbines that are considered efficient fall into the 34-45% range. Based on this data it appears that the shrouded wind turbine design may provide a clear advantage when attempting to capture energy from the wind in low wind speed areas.

4. Education and Outreach

As an education and outreach element several key activities were undertaken to inform and educate the public as to both sustainable energy practices and sustainable energy career opportunities.

4.1. Website Development

TBEIC created a website (http://tbeic.org/) depicting the status of the TBEIC facility, the anticipated business incubation and acceleration services, and promotion of other pending outreach initiatives. The facility also has a Facebook page and a Twitter account.

Live data depicting energy generated by solar panels on the YSU campus is currently available at: http://live.deckmonitoring.com/?id=youngstown_state_university. This information is posted on the YSU STEM College website and is mapped to several other regional energy-related sites. Similar depictions of data showing energy generated from the installed wind turbine are set up and ready to go live pending trouble shooting from Green Energy Technologies Electrical Engineers.

4.2. Kiosks

YSU collaborated with the OH WOW Children's Center for Science and Technology, located in downtown Youngstown to build energy kiosks at the facility. YSU now provides real time video feeds of solar panels and the correlated energy generation data. The OH WOW graphics and web team made the display and information age-appropriate for the audience. Cameras, servers, and display screens show the solar panels and the wind turbine.

4.3. Sustainable Energy Forum

Three YSU Sustainable Energy Forums were held during the grant period with plans to continue the forums through TBEIC in the future years. All conference activities were made available at no cost to attendees. The first of the three forums featured Acting Assistant Energy Secretary Henry Kelly and Siemens North America President Eric Spiegel as keynote speakers.

The second forum keynote speakers were Marc Gerken, President of American Municipal Power; Jason Walsh, Senior Adviser, U.S. Department of Energy (Office of Energy Efficiency and Renewable Energy); Craig Butler, Assistant Policy Director Energy, Agriculture and Environment, Office of Governor John Kasich; Cynthia Powell, Director, Office of Research and Development, National Energy Technology Laboratory; David Mordan, Director – NGL Operations, Dominion Transmission; Scott Hallam, Manager – Development and Operations, Chesapeake Energy. At

this second forum, more than twenty companies and organizations displayed their technologies at the Energy Expo, and other displays featured electric and natural gas vehicles.

The third YSU forum during the grant period included keynote speakers: Ed Morris, Director, National Additive Manufacturing innovation Institute; Sean O'Brien, State Representative; Dr. Jeffrey Daniels, Ohio State University; Ms. Kelly Visconti, Department of Energy (EERE); Dr. Cynthia Powell, Director - Department of Energy (NETL); Mike Wise, McDonald Hopkins Law Firm; Scott Coye - Huhn, Aloterra Energy (Biofuels); Steve Csonka, Director of Commercial Aviation Alternative Fuels Initiative (CAAFI); Raymond Evans, Vice President of Environmental - First Energy; Chris Jaskiewicz, Vice President of Valley Electrical Consolidated (VEC); Matthew Moran, NASA Glenn; Dr. Craig Blue, Oak Ridge National Laboratory; Dave Mrowinski, IGS Energy MINDDRIVE Vehicle, a Kansas City-based after school program designing electric vehicles. In addition, the TBEIC Leadership team held a Natural Gas/Fuel Cell breakout session for interested parties.

4.4.Network Development with the Energy Incubator

The heart of the TBEIC outreach program is to offer entrepreneurial support to start-up energy companies and help in the commercialization of new energy technologies. The program elements include collaborations with regional partners and universities while building-out the TBEIC facility as an energy company incubator/accelerator and shared technology resource center. While establishing TBEIC as an industry asset (state and nationwide), all elements of the TBEIC program lend to the pipeline of tenants and users of the facility. Ongoing focus includes developing marketing, social media, and outreach to existing energy companies in the state of Ohio. TBEIC was named the lead energy sector incubator in the state of Ohio and has been actively trying to recruit companies, startups, and individuals to work from the Warren incubator. TBEIC has developed email marketing campaigns and has held two open house events to promote the opening of the TBEIC facility.

4.4.1. General Outreach

The key to leveraging TBEIC outreach activities is collaboration with other economic development organizations and universities. For example, TBEIC participated in the Youngstown NASA Roadshow. TBEIC not only helped planned, but also had two companies complete the Roadshow and gain access to NASA subject matter experts. The collaboration with NASA on the Roadshow has led to a signing of a joint use agreement that partners NASA and TBEIC in research and development activities. TBEIC has also actively worked with Team NEO, Jumpstart, YBI, and other local economic development organizations to create

collaboration and promote the activities of TBEIC and its companies. The Valley Alliance for Science and Technology also has been a great promotion tool for the Tech Belt Energy Innovation Center; local executives and companies owners are coming to TBEIC to learn about the organization and hear the workshops that TBEIC puts together.

TBEIC reports detailed activities to YSU in monthly invoice support packages. General outreach activities continued with an emphasis on building the TBEIC name and reach across Ohio. This effort is intended to increase the TBEIC toolbox of support for companies in the energy industry and build a healthy flow of opportunity to sustain TBEIC operations.

4.4.2. Collaborations

With the completion of the TBEIC is building, staff concentrated on recruiting companies to the Warren Incubator. Staff is connecting with other organizations that further the TBEIC mission and leverage resources. Key collaborations give TBEIC access to technical assets, financial assets for start-up companies, and industry partnerships that can speed the process of technology commercialization.

TBEIC continued work with JumpStart and the JumpStart Entrepreneurial Network (JEN) on go-forward collaboration for the TBEIC program. As part of the JEN, TBEIC is the sector lead for energy start-ups in the 21 counties of Northeast Ohio. TBEIC has served more than 80 energy or natural resource startup companies/opportunities resulting in more than 20 of them achieving funding events or industry partnerships. TBEIC worked with JumpStart on a new collaboration agreement to solidify its relationship in the JEN for another two years that started in January 2017.

4.4.3. Entrepreneurial Support

Entrepreneurial support included business planning reviews, coaching, planning and preparation for fundraising and investment opportunities, technology reviews, business model validation, strategic partner introductions and many other entrepreneurial support services.

As examples of the work being done at TBEIC, some of the companies that have and continue to be actively supported include:

Ashlawn Energy - Ashlawn Energy is the third company to move into the TBEIC building. The founder moved the research and development office from Johnstown, Pennsylvania to Warren, Ohio. Ashlawn works with fuel cells for munitions and flow batteries and works in the areas of

nanomaterials, powder metals, transitioning R&D projects into pilot production, manufacturing technologies, and process improvements.

First Fuel Cells.com - FirstFuelCells.com is a company that started in Parma, Ohio and has shown an interest in moving to TBEIC, the company currently is reviewing the TBEIC Tenant License Agreement. First Fuel Cells creates fuel cells and packages kits for educational purposes. The company also manages the First Ohio Robotics Competition that brings together high schools students to compete in developing fuel cell run robots and other technologies.

Alios 3D - Alios 3D is the first TBEIC Tenant Company to move into the building. They reserved a first floor office that measures over 600 sq ft. Alios has three people on staff working on the operations, sales, and engineering of 3D prototype printing. Alios offers professional services and contract manufacturing to clients. The company has advanced 3-D printing machines primarily for plastic materials stock, ceramic and metal 3-D printing capabilities. Alios will provide additive manufacturing consultation, design and training.

Sky Harvest Wind - Sky Harvest Wind is the second tenant company to move into TBEIC. Sky Harvest Wind is engaged in the development, marketing and distribution of small vertical axis wind turbines. TBEIC EIR's have been working with the company to grow their Warren office and to figure out new go to market strategies.

MegaJoule - MegaJoule is commercializing grid level energy storage solutions for industrial power quality and microgrid applications. TBEIC continues to work closely with MegaJoule, connecting them to partners, potential customers and potential hires. MegaJoule has shown an interest in moving into the TBEIC facility. Megajoule is a TBEIC company that is in the application process with the Youngstown NASA Roadshow. Through a VAST meeting, MegaJoule partnered with a local manufacturing company to research fuel cells.

TMI - TMI has developed a solid-oxide fuel cell system that can power homes, forward operating military units, and third world applications in a cost-effective manner. TBEIC continues to work closely with TMI on its strategy for the US State Department's Power Africa program.

CFRC - CFRC is a minority-led company with a revolutionary water saving showerhead that has broad application in the hotel, real estate and education sectors. TBEIC is working with CFRC on various business issues and opportunities, including completing the Cuyahoga County North Coast Opportunities Technology Fund disbursement and beginning go-to-market strategies.

The company is currently preparing to run a test with the Departments of Transportation for California, Florida, and Ohio.

Design Flux Technologies - Design Flux (DFT) has a unique energy management system that dramatically improves the efficiency of and cuts the design time of battery operated devices from power tools to electric tractors to electric vehicles to grid-level energy storage systems. TBEIC is working with DFT to achieve critical non-dilutive funding through the Innovation Fund and the North Coast Opportunities fund. DFT began important collaborative projects with BMW electric vehicles, EPRI and Case Western Reserve University.

Intwine Energy - Intwine has unique software and hardware to truly enable individualized building management in high-rise rental units. TBEIC continues to work with Intwine as it progresses in trials and expands its development resources at CWRU, as well as achieve additional non-dilutive funding through the Innovation Fund.

FITOS - FITOS has a patented method for controlled cracking of indium tin oxide panels, enabling significant cost reduction and improved performance of controlled windows (first application) and touchscreen displays.

Brilliency - TBEIC began working with Brilliency, a woman-led business focused on improving the interface between municipal utilities and their customer base, as well as preparing to act as an energy trading partner with the advent of micro-grids in the U.S. TBEIC is currently helping Brilliency prepare to present at the North Coast Opportunity Fund.

HLC - HLC has a unique, patented technology that uses boron doped diamond for electro-oxidation, resulting in significant improvement in performance and cost in treating severely contaminated wastewater. This technology could change the wastewater equation for U.S. chemical plants, potentially avoiding the use of deep injection wells for waste storage.

Yanhai Power - TBEIC has worked with Yanhai Power in researching and submitting information for an SBIR application. TBEIC EIR's have also been influential in drafting a commercialization plan for the company. Yanhai Power has showed an interest in moving to the TBEIC facility.

4.4.4. Energy Integration Lab (EIL) Development

A key differentiator of the TBEIC facility and program is the focus on commercialization of new grid-connected and other energy technologies. Primed by this Department of Energy grant and other contributions, TBEIC is working to create a unique national resource for energy system research, testing and development. It is unique with regard to the ease of access to resources

necessary to test, demonstrate and develop technologies, and industry connections necessary to identify customer needs and marketing or manufacturing partnerships.

TBEIC's planned energy systems lab will provide an environment for energy entrepreneurs to evaluate grid compatibility and "readiness" early in the development process, as well as develop power electronics and key testing methodologies. As a shared resource center, the TBEIC lab will be accessible to start ups and existing companies across the country seeking access to expertise and equipment to bring grid-connected devices to market.

In May 2017, a $245,000 grant from the Appalachian Regional Commission was awarded to the Tech Belt Energy Innovation Center. The grant will unlock matching funds from the state of Ohio and permit TBEIC to build out TBEIC's shared resource lab! Technical focal points of the center will include a grid-connectivity and simulation lab, as well as an intelligent device lab, where IoT (Internet of Things) devices can be tested and certified per emerging industry standards in a grid-connected environment. The center will also be used to help local industry make decisions regarding investment in new energy-saving technologies through technical demonstrations and testing.

5. References

Abbott, Ira H. *Theory of Wing Sections/ Including a Summary of Airfoil Data*. New York: Research Engineer, NASA, 1949. Print.

Airfoil Investigation Database. 26 May 2013. Web. 30 Oct. 2014. <http://www.airfoildb.com/foils/list>.

Burton, Tony, David Sharpe, Nick Jenkins, and Ervin Bossanyi. *Wind Energy Handbook.*England*.* John Wiley &Sons, Ltd, 2001. Print.

Dwyer. "Air Velocity Measurement:How to Take Traverse Readings." *Dwyer Instruments Inc*. Web. 20 Jan. 2015. <http://www.dwyerinst.com/products/airvelocityintroduction.cfm>.

Engineering design and Technology Series. "*Student's Guide to learnings SolidWorks Software*". SolidWorks Corporation. Massachuests.printed.

Forman, K. M. "Preliminary Design and Economic Investigations of Diffuser Augmented Wind Turbines (DAWT)." *Research Department/ Grumman Aerospace Corporation* (May 15 1980). Print.

Foreman, K. M., B. Gilber, and R. A. Oman. "Diffuser Augmentation of Wind Turbines." *Solar Energy,* 20 (1978): 305-11. Print.

Forman, K. M. "Size Effects in DAWT Innovative Wind Energy System Design." *J. Solar Energy Engineering* 105.4 (01 Nov1983): 401-07.Print.

Fluent Inc. "Pressure-Based Solver." *SAS IP, Inc* (2014).Web.19 Jan. 2015.

Fuel Economy. The official U.S. Government Source for Fuel Economy Information.15 Oct, 2012. Web. 3 June 2014.

FlowKinetics LLC. *Generic Pitot-Static Pitot Configuration*. Digital image. 2001-2015. Web. 4 Jan. 2015. <http://www.flowkinetics.com/pitot-static-probe-measurement.htm>.

Grassmann, H., F.Bet, M. Ceschia, and M.L. Ganis. "On the Physics of Partially Static Turbines". *Renewable Energy,* Vol. 29 (2003): 491-499. Print.

Green Energy Technologies. Issue brief. Green Energy Technologies, LLC. Web. 10 Oct. 2014. <http://www.getsmartenergy.com/>.

Ganis, Maximilian Ludwig. *National Institute for Nuclear Physics/Department of Physics of Udine*. Hamburg. 2003. Print.

Hansen, Martin O.L. *Aerodynamics of Wind Turbines.* 2nd ed. London: Earthscan, 2008. 27-42. Print.

Hansen, M. O. L, N. N. Sqrensen, and R. G J. Flay. "Effect of Placing a Diffuser around a Wind Turbine." *Wind Energy* 3 (2000): 207-13. Print.

Health Canada. The Government of Canada, 3 April 2014. Web. 25 June 2014.

Hibbeler,R.C. *Fluid Mechanics*. *Pearson Prentice Hall*. NJ. 2015. Print

Igra, Ozer. "Research and Development for Shrouded wind turbines." *Energy Cmt & Mgmt*, Vol. 21,pp. 1981: 13-48. Print.

Igra, Ozer. "The Shrouded Aerogenerator." *Energy Cmt & Mgmt*, Vol. 2, p. 1977:429-439. Print.

Jamieson, P., Garrad Hassan, and Partners. "Beating Betz-Energy Extraction Limits in a Uniform Flow Field." *Conference Paper* (2008). Web. <http://www.gl-garradhassan.com/assets/downloads/Beating_Betz_Energy_Extraction_Limits_in_a_Uniform_Flow_Field.pdf>.

Jafari, S.A.H, and B. Kosash. "Flow Analysis of Shrouded Small Wind Turbine with a Simple Frustum Diffuser with Computational Fluid Dynamics Simulations". *J.Wind Eng. Ind. Aerodyn., Vol.125* (2014):102-110. Print.

Klujszo, L.A.C., P.K.Songfack, M. Rafaelof, and R. K. Rajamani, "Design of a Stationary Guide Vane Swirl Air Cleaner," *Minerals Engineering*, vol. 12, no. 11, pp.1375–1392, 1999.

Kossasih, P.B., N. Bryce, A. Tondelli, and A. Breazley. "Experimental Study of the Performance of Bare and Nozzle-Diffuser Shrouded Micro Wind turbine Under Axial and Non-Axial Inflow Condition." *Australasian Fluid Mechanics Conference.* Launceston. 7 December 2012.

Kelecy, Franklyn *J. "*Coupling Momentum and Continuity Increases CFD Robustness". *Applications Specialist, ANSYS, Inc.* Volume II, Issue 2, 2008.

Lilly, G.M., and W.J Rainbird. *A preliminary Report on the Design and Performance of Ducted Windmills.* Rep. no. 102. College Of Aeronautics Cranfield, 1956. Print.

Lubitz, William David, and Shomer, Adam. “Wind Loads and Efficiency of a Diffuser Augmented Wind Turbine (DAWT).” *CSME international Congress* (4 June 2014). Print.

Lawn, C. J. "Optimization of the Power Output from Ducted Turbines." *J. Power and Energy* 217 (2003): 107-17. Print.

Mouser Electronics. *MLV Series Low Voltage Pressure Sensors*. Digital Image. *DesignNews*.14 Feb. 2011. Web. 5Jan2015.<http://www.designnews.com/document.asp?doc_id=230126&dfp PParams=ind_184, aid_230126&dfpLayout=article>.

National Instruments. “Data Acquisition (DAQ)”.2014. Web. 6 January 2015 NRDC. Renewable Energy for America, 2011. Web. 9 June 2014.

Ohya, Yuji, and Takashi Karasudani. “A Shrouded Wind Turbine Generating High Output Power with Wind-lens Technology”. *Energies,* Vol. 3 (2010): 634-649. Print.

P. Bulat, Mikhail, and Pavel Victorovich Bulat. "Comparison of Turbulence Models in the Calculation of Supersonic Separated Flows." *World Applied Sciences Journal* 27.10 (2013): 1263-266. Print.

Philips, Derek Crant. *An Investigation on Diffuser Augmented Wind Turbine Design*. Diss. The University of Auckland, 2003. New Zealand: ResearchSpace@Auckland, 2003. Print.

PI Research. “Pitot Static Tube.” 1-4. *Cosworth*. 2014. Web. 4 Jan. 2015. <http://www.cosworth.com/media/198947/29b-071181.pdf>.

Righter, Robert W. *Wind Energy in America*. Norman. The University Of Oklahoma Press.pp. 42-58. 1996. Print.

Rittner, Don. “Windmills of East-America’s first Green Technology” *Timesunion.com*. Hearst Corporation, 18 May 2010. Web. 22 July 2014.

Rienstra, S.W. “A Note on the Kutta Condition in Glauert’s Solution of the Thin Airfoil Problem.” *Journal of Engineering Mathematics*. 26:61-69. 1992. Print.

Rice University. *World Energy Use*. Digital image. *Openstax CNX*. 2006. Web. 12 Sept. 2014. <http://cnx.org/contents/a4b7e0ec-bded-45de-8016-416aaaa8286b@5/World_Energy_Use>.

Sangoor, Abbas "Experimental and Computational Study of the Performance of a New Shroud Design for an Axial Wind Turbine." Electronic Thesis. Youngstown State University, 2015. <https://etd.ohiolink.edu>

Spera, Daivd A. *Wind Turbine Technology/ Fundamental Concepts of Wind Turbine Engineering*. 2nd ed. New York: ASME, 2009. Print.

Spera, David A. *Advisory on Shrouded Wind Turbine Project*. Rep. Florida: DASCON Engineering,LLC. 19 June 2014. Print

Spera, David A. *Update WindSphere Shroud CFD Analysis*. Rep. Florida: Dascon Engineering, LLC. 15 October 2014. Print.

Snel, H. "Reviews of Aerodynamic Investigation and Design Work Underlying the Vortec 1 MW Turbine and Suggestions for Further Optimization." (2001): 1-27. Print.

Shinomiya, Leo Daiki, Déborah Aline, Amanda Maria, Taygoara Felamingo, José Gustavo, André Luiz Amarante, and Jerson Rogério Pinheiro. “Numerical Study of Flow around Diffusers with Different Geometry Using CFD Applied to Hydrokinetics Turbines Design.” *OBEM International congress of Mechanical Engineering.* 7 November2013.

Shah, Ishan.M, S. A. Thakkar, K. H Thakkar, and Bhavesh A. Patel. "Performance Analysis on Airfoil Model in Wind Tunnel Testing Machine (WTTM)." *Engineering Research and Applications (IJERA)* 3.4 (2013): 2094-103. Print.

Sveningsson, Andreas. "Analysis of the Performance of Different Turbulence Models in a Stator Vane Passage_Flow." *Department of Thermo and Fluid Dynamics Chalmers University Of Technology* (2003). Print.

SolidWorks. "SOLIDWORKS TUTORIALS." *Dassault Systemes Solidworks*. N.p., 2014. Web. 18 Sept. 2014. <http://www.solidworks.com/sw/resources/solidworks-tutorials.htm>.

Ukhovskii, M.R, and V.I. Iudovich. "Axially Symmetric Flows of Ideal and Viscous Fluids Filling the Whole Space." *Elsevier Ltd.* 32.1 (1968): 59-69. Print.

Van Bussel, Gerard J.W, Dr. "The Science Of Making More Torque From Wind:Diffuser Experiments and Theory Revisited." *Journal of Physics: Conference* 75th ser. (2007): 1-12. Print.

Van Bussel, Gerard J.W, Dr. “An Assessment of the Performance of Diffuser Augmented Wind Turbine (DAWT’S). *ASME:* 23 July 1999. Print.

Widnall, Sheila. “Potential Flow Calculation of Axisymmetric Ducted Wind Turbine”. *Massachusetts Institute of Technology*. July, 2009.1-19. Print

Wang, Sheng- Huan, and Shih-Hsiug Chen. "Blade Number Effect for a Ducted Wind Turbine." *Mechanical Science and Technology/Spring* 22 (2008): 1984-992. Print.

Yamin, Mat, A.K, Benjamin, S.F, and Roberts C.A. "Pulsating Flow in a Planar Diffuser Upstream of Automotive Catalyst Monoliths." *Int J of Heat and Fluid Flow (benjamin)* 40 (2013): 43-53. Print.

Appendix A

Axial Air Velocity Distribution at Test Wind Tunnel Sections

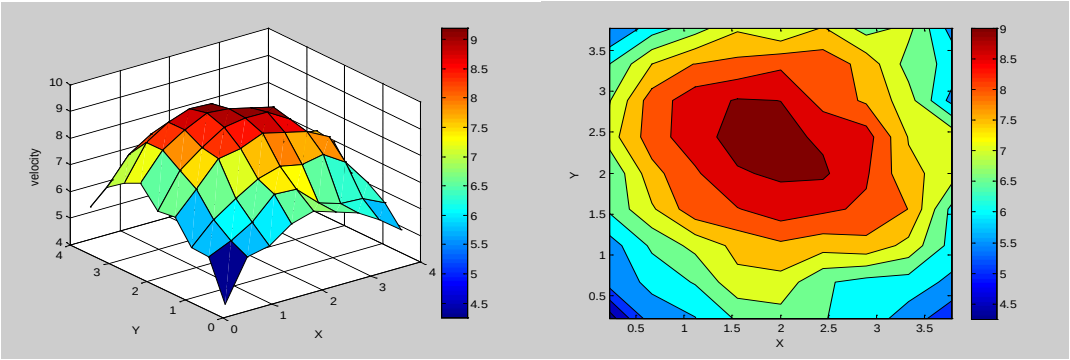

Figure A.1 Air velocity distribution in testing section1 (4 feet from the Fan) (air direction is blowing in reverse direction (backward)).

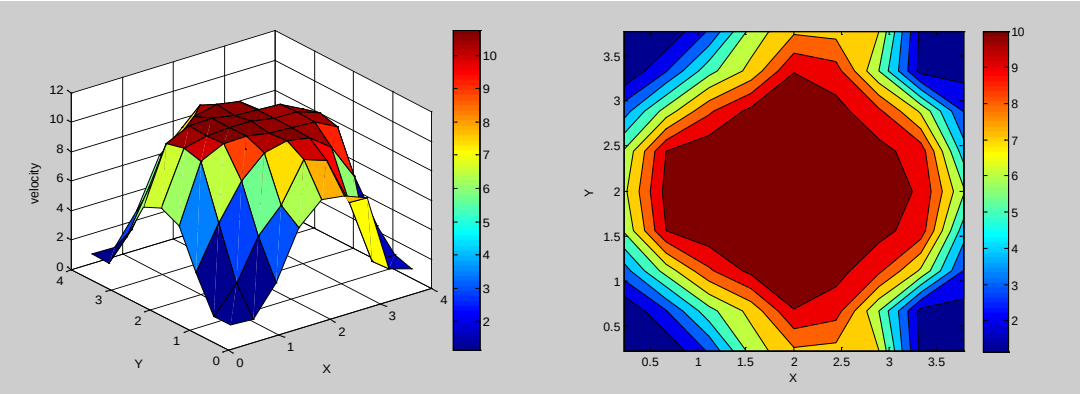

Figure A.2 Air velocity distribution in testing section2 (12 feet from the Fan) (air direction is blowing in reverse direction (backward)).

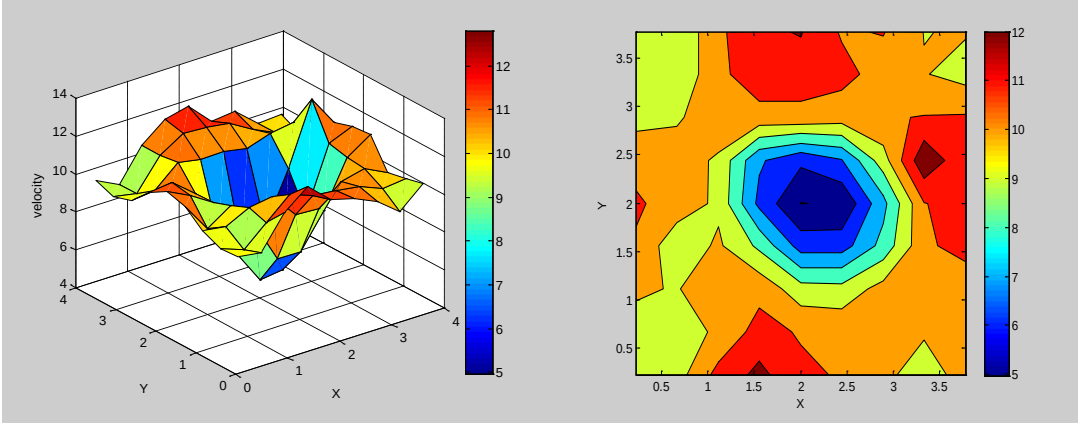

Figure A.3 Air velocity distribution in testing section1 (4 feet from the Fan) (air direction is blowing in forward direction).

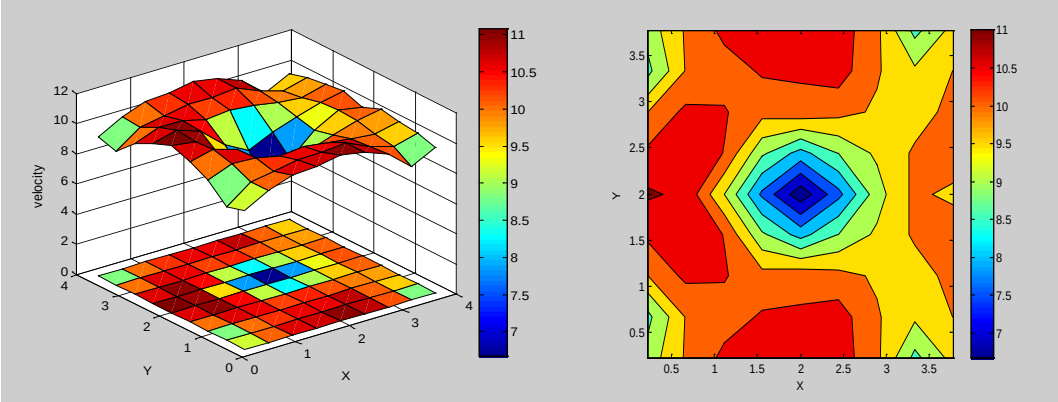

Figure A.4 Air velocity distribution in testing section2 (12 feet from the Fan) (air direction is blowing in forward direction).

Appendix B

Shroud Models' Configurations

Table B.1 Databases of the shroud models' geometries (M1,M2,M3,and M4).

AR=1.75		AR=2		AR=2.5		AR=3	
x	y	x	y	x	y	x	y
142.2258	212.9885	164.4796	229.8384	158.0399	245.154	170.5043	265.7251
133.0169	211.1323	155.3805	226.9368	151.0391	242.0935	163.9246	261.8411
123.7805	209.418	146.2348	224.1851	144	239.122	157.2961	258.0409
114.5188	207.8466	137.0471	221.577	136.9239	236.2399	150.6201	254.3249
105.2328	206.4254	127.8196	219.1137	129.8097	233.4529	143.8948	250.6988
95.92395	205.163	118.5526	216.8032	122.6574	230.7656	137.1196	247.1669
86.59458	204.0623	109.2468	214.6545	115.4678	228.1795	130.2951	243.7311
77.24794	203.1192	99.90462	212.6701	108.2429	225.6938	123.4235	240.3906
67.88757	202.3237	90.52991	210.8453	100.9856	223.3043	116.5081	237.1417
58.51626	201.6694	81.12735	209.1698	93.69881	221.0061	109.5524	233.9799
49.13626	201.1546	71.70029	207.6381	86.38454	218.7971	102.5587	230.9033
39.74944	200.7849	62.25108	206.2495	79.04413	216.6765	95.52827	227.9113
30.35781	200.5706	52.78106	205.0111	71.67797	214.6472	88.46127	225.0068
20.96384	200.5372	43.29105	203.9361	64.28608	212.7139	81.35715	222.1944
11.5715	200.7134	33.78135	203.0541	56.86756	210.8851	74.21396	219.4827
2.186043	201.1132	24.25372	202.3929	49.42042	209.1772	67.02775	216.8874
-7.18717	201.7377	14.71283	201.9641	41.94335	207.6054	59.79538	214.4237
-16.5446	202.5661	5.164357	201.7644	34.43733	206.1782	52.5168	212.1
-25.8842	203.5764	-4.38624	201.7686	26.90476	204.8986	45.19404	209.9196
-35.2047	204.75	-13.935	201.9562	19.34926	203.7619	37.83124	207.8784
-44.5066	206.0629	-23.4793	202.3075	11.77549	202.7541	30.43473	205.9628
-53.8005	207.4323	-33.0181	202.7845	4.186856	201.8652	23.0091	204.1635
-63.1056	208.7214	-42.5561	203.2771	-3.41384	201.0856	15.55829	202.4712
-72.4552	209.624	-52.1012	203.5886	-11.024	200.4051	8.08607	200.8761
-81.8355	210.0569	-61.6503	203.4467	-18.6404	199.7961	0.599156	199.3513
-90.9708	208.141	-71.1135	202.3518	-26.2575	199.1971	-6.88975	197.8363
-92.8953	200.383	-78.856	197.3851	-33.8685	198.5275	-14.3642	196.252
-87.1349	193.0004	-74.7199	189.148	-41.4514	197.5952	-21.7788	194.4103
-79.7684	187.1929	-67.3965	183.0583	-48.9995	196.4091	-29.1283	192.3208
-71.622	182.5266	-59.0047	178.5156	-56.354	194.4014	-36.1864	189.4392
-63.0222	178.7537	-50.1036	175.0667	-62.6374	190.2048	-41.9166	184.5141
-54.1475	175.6792	-40.9195	172.4549	-61.0012	183.4429	-39.4754	177.9995
-45.0869	173.2036	-31.5672	170.5269	-55.1482	178.5564	-33.0749	173.856
-35.8989	171.2514	-22.1126	169.1845	-48.4143	174.9687	-25.9567	171.1082
-26.6226	169.7737	-12.5985	168.3608	-41.2418	172.3469	-18.52	169.3723
-17.2859	168.7442	-3.05501	168.0134	-33.8403	170.4613	-10.9449	168.3948
-7.91096	168.1569	6.494162	168.1273	-26.3125	169.1617	-3.31518	168.0143
1.481247	168.0043	16.02714	168.6953	-18.7172	168.3407	4.323654	168.1171
10.87078	168.2736	25.52379	169.7029	-11.0879	167.9384	11.94558	168.6396
20.23972	168.9527	34.96575	171.1351	-3.44806	167.9043	19.53361	169.5289
29.57118	170.03	44.33619	172.9786	4.186119	168.204	27.07565	170.7489

38.8506	171.4904	53.62015	175.2175	11.80201	168.8121	34.56226	172.2727
48.06664	173.3085	62.80639	177.8287	19.38845	169.7161	41.98389	174.0868
57.21756	175.4311	71.89329	180.7677	26.9346	170.911	49.33038	176.1847
66.3113	177.7872	80.89456	183.9599	34.43006	172.3909	56.59209	178.5595
75.35451	180.3306	89.82314	187.3501	41.86571	174.1468	63.76111	181.2009
84.35139	183.0333	98.68724	190.9059	49.23332	176.1697	70.8303	184.0992
93.30549	185.8748	107.4924	194.605	56.52479	178.4515	77.79265	187.2453
102.2207	188.8361	116.2448	198.4276	63.73312	180.9841	84.64215	190.6304
111.0996	191.9046	124.949	202.3587	70.85212	183.7579	91.37383	194.244
119.9424	195.0754	133.6062	206.3923	77.8778	186.7602	97.98528	198.0732
128.7484	198.3472	142.2159	210.5262	84.81097	189.9705	104.4797	202.0978
137.5142	201.725	150.775	214.7639	91.66203	193.3528	110.8719	206.2831
146.2294	205.2314	159.2721	219.1243	98.44367	196.8723	117.1786	210.5962
154.8719	208.913	167.6807	223.653	105.1647	200.5062	123.4113	215.0155
163.3464	212.9607	175.9082	228.4991	111.8311	204.2395	129.5778	219.527
171.4788	217.6626	183.7044	234.0146	118.447	208.0614	135.6834	224.1204
178.5991	222.31	191.3234	239.7015	125.0171	211.9619	141.734	228.7861
169.6437	219.4818	182.5083	236.1346	131.5453	215.9319	147.7348	233.5158
160.5463	217.1517	173.5292	232.8916	138.0344	219.9654	153.689	238.3039
151.4033	214.9938	164.4796	229.8384	144.4852	224.0601	159.5977	243.148
142.2258	212.9885			150.8977	228.2145	165.4612	248.0467
				157.2709	232.4288	171.2785	253.0003
				163.6012	236.7073	177.0455	258.0123
				169.8792	241.0622	182.7513	263.0939
				176.0866	245.517	188.3749	268.2661
				182.1943	250.1073	193.8832	273.5607
				187.9831	255.0894	199.0276	279.2058
				193.5723	260.2988	203.9465	285.0524
				198.9751	265.6412	208.6641	291.0085
				192.3416	261.9336	202.5272	286.5264
				185.6588	258.2347	196.3403	282.0472
				178.7886	254.8912	189.9244	277.8981
				171.9248	251.5347	183.5165	273.7368
				165.0024	248.3007	177.0356	269.6901
				158.0399	245.154	170.5043	265.7251

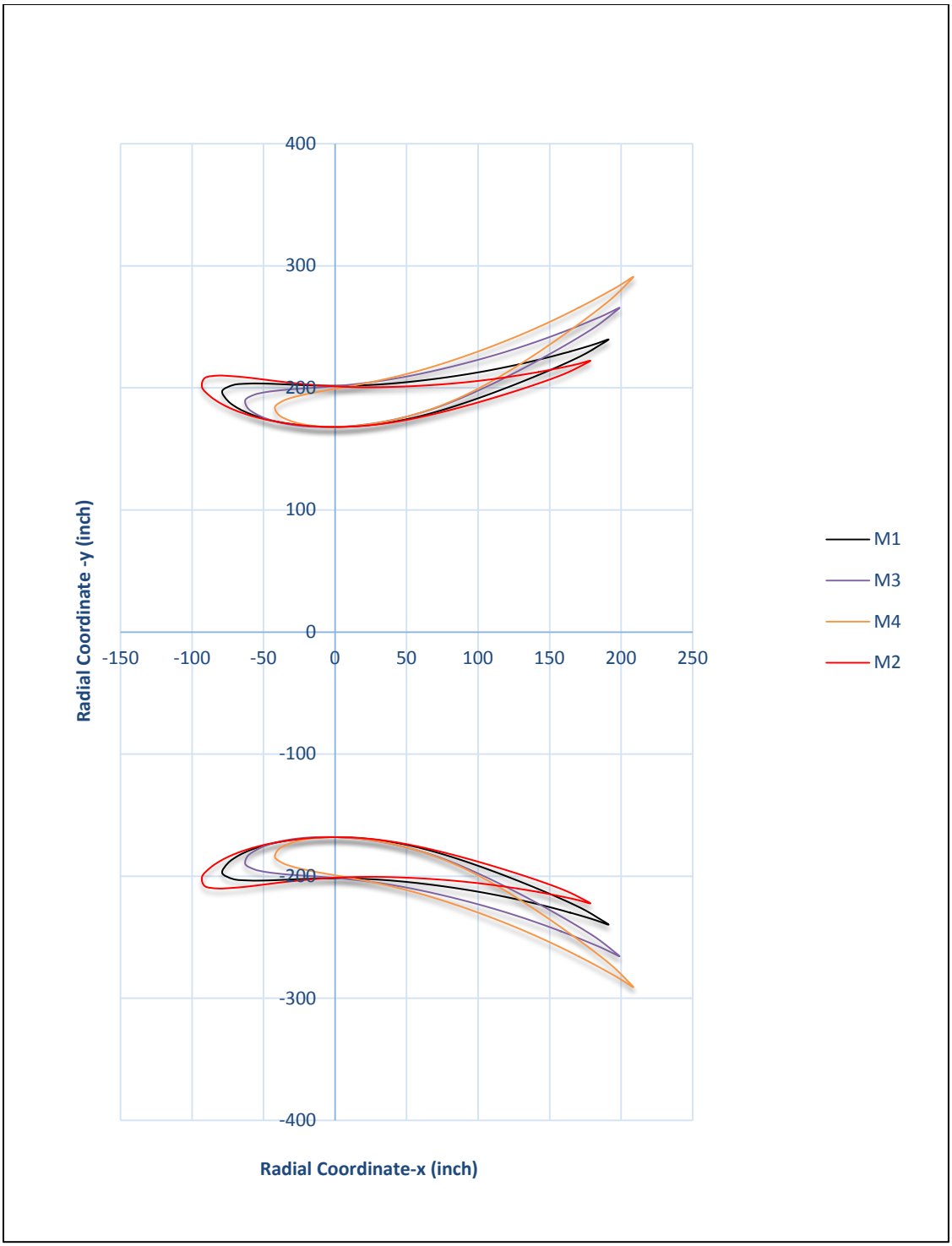

Figure B.5 shroud models (M1, M2, M3, and M4) (changing the angle of attack and keeping the length and throat radius constant)

Table B.2 Databases of the shroud models' geometries (M1, M5, and M6).

AR= 2		AR=3		AR=4		Experimental model	
x	y	x	y	x	y	x	y
164.4796	229.8384	282.0826	274.0528	385.3248	312.8681	4.613537	6.191777
155.3805	226.9368	266.4775	269.0766	364.0083	306.0706	4.372941	6.110603
146.2348	224.1851	250.7927	264.3574	342.5828	299.6242	4.13103	6.03346
137.0471	221.577	235.0358	259.8846	321.0589	293.5144	3.887874	5.9603
127.8196	219.1137	219.2106	255.66	299.4417	287.7435	3.643603	5.890961
118.5526	216.8032	203.3178	251.6975	277.7321	282.3308	3.398275	5.82547
109.2468	214.6545	187.3583	248.0125	255.9314	277.2971	3.151901	5.764043
99.90462	212.6701	171.3364	244.6093	234.0455	272.6483	2.904493	5.706917
90.52991	210.8453	155.2588	241.4797	212.0835	268.3732	2.65612	5.65416
81.12735	209.1698	139.1334	238.6062	190.0562	264.448	2.406878	5.605643
71.70029	207.6381	122.966	235.9793	167.9716	260.8597	2.156893	5.561096
62.25108	206.2495	106.7606	233.5979	145.835	257.6067	1.906256	5.520373
52.78106	205.0111	90.51951	231.4741	123.6497	254.7056	1.65503	5.483455
43.29105	203.9361	74.24416	229.6305	101.4175	252.1873	1.403258	5.450532
33.78135	203.0541	57.93502	228.1178	79.13924	250.1209	1.150958	5.421953
24.25372	202.3929	41.59515	226.9838	56.81897	248.5719	0.898124	5.398502
14.71283	201.9641	25.23251	226.2485	34.4676	247.5674	0.644815	5.380923
5.164357	201.7644	8.856872	225.906	12.09849	247.0995	0.391158	5.369523
-4.38624	201.7686	-7.52241	225.9131	-10.2756	247.1093	0.137301	5.364214
-13.935	201.9562	-23.8986	226.2348	-32.6454	247.5488	-0.1166	5.364324
-23.4793	202.3075	-40.2669	226.8373	-55.0046	248.3718	-0.37047	5.369312
-33.0181	202.7845	-56.626	227.6554	-77.3511	249.4892	-0.62423	5.378652
-42.5561	203.2771	-72.9837	228.5002	-99.6958	250.6432	-0.87784	5.391334
-52.1012	203.5886	-89.3535	229.0344	-122.057	251.373	-1.13142	5.40443
-61.6503	203.4467	-105.73	228.7911	-144.428	251.0406	-1.38519	5.412712
-71.1135	202.3518	-121.96	226.9134	-166.597	248.4757	-1.63907	5.40894
-78.856	197.3851	-135.238	218.3954	-184.735	236.8401	-1.89071	5.379818
-74.7199	189.148	-128.145	204.2688	-175.046	217.5431	-2.0965	5.247794
-67.3965	183.0583	-115.585	193.825	-157.889	203.277	-1.98654	5.028786
-59.0047	178.5156	-101.193	186.0343	-138.23	192.6349	-1.79184	4.866882
-50.1036	175.0667	-85.9276	180.1193	-117.377	184.555	-1.56884	4.746161
-40.9195	172.4549	-70.177	175.6401	-95.8618	178.4364	-1.33208	4.654413
-31.5672	170.5269	-54.1378	172.3336	-73.9522	173.9197	-1.08793	4.58498
-22.1126	169.1845	-37.9232	170.0313	-51.803	170.7748	-0.83926	4.533717
-12.5985	168.3608	-21.6064	168.6188	-29.5144	168.8453	-0.58796	4.498033
-3.05501	168.0134	-5.23934	168.023	-7.15691	168.0315	-0.33503	4.476133
6.494162	168.1273	11.13749	168.2184	15.21385	168.2983	-0.08124	4.466893
16.02714	168.6953	27.48654	169.1924	37.54661	169.6288	0.172657	4.469921
25.52379	169.7029	43.7733	170.9204	59.79433	171.9893	0.42609	4.485018
34.96575	171.1351	59.96626	173.3768	81.91391	175.3447	0.678576	4.511807
44.33619	172.9786	76.03657	176.5384	103.866	179.6634	0.929622	4.549889
53.62015	175.2175	91.95856	180.3779	125.6154	184.9083	1.178724	4.598896
62.80639	177.8287	107.713	184.8563	147.1359	191.0257	1.425521	4.658409
71.89329	180.7677	123.297	189.8967	168.4237	197.9109	1.669776	4.727839
80.89456	183.9599	138.7342	195.3712	189.5109	205.389	1.911397	4.805987
89.82314	187.3501	154.0468	201.1855	210.4279	213.3314	2.150695	4.89085

98.68724	190.9059	169.2486	207.2836	231.1936	221.6614	2.388068	4.980981
107.4924	194.605	184.3495	213.6276	251.8215	230.3274	2.623746	5.075522
116.2448	198.4276	199.3599	220.1832	272.3256	239.2823	2.857855	5.173873
124.949	202.3587	214.2876	226.9251	292.7168	248.4917	3.090549	5.2755
133.6062	206.3923	229.1346	233.8427	312.9978	257.9411	3.321962	5.380014
142.2159	210.5262	243.9002	240.9324	333.1677	267.6256	3.552128	5.487254
150.775	214.7639	258.579	248.2	353.219	277.5532	3.781031	5.597161
159.2721	219.1243	273.1516	255.6782	373.1251	287.7685	4.008587	5.709827
167.6807	223.653	287.5724	263.4448	392.8239	298.3776	4.2345	5.825759
175.9082	228.4991	301.6825	271.756	412.0983	309.7307	4.458054	5.946158
183.7044	234.0146	315.0531	281.2151	430.3626	322.6519	4.676798	6.075005
191.3234	239.7015	328.1196	290.9681	448.2113	335.9744	4.884072	6.221642
182.5083	236.1346	313.0017	284.8508	427.5603	327.6182	5.086617	6.37284
173.5292	232.8916	297.6026	279.2891	406.5251	320.0209	4.852274	6.278003
164.4796	229.8384	282.0826	274.0528	385.3248	312.8681	4.613537	6.191777

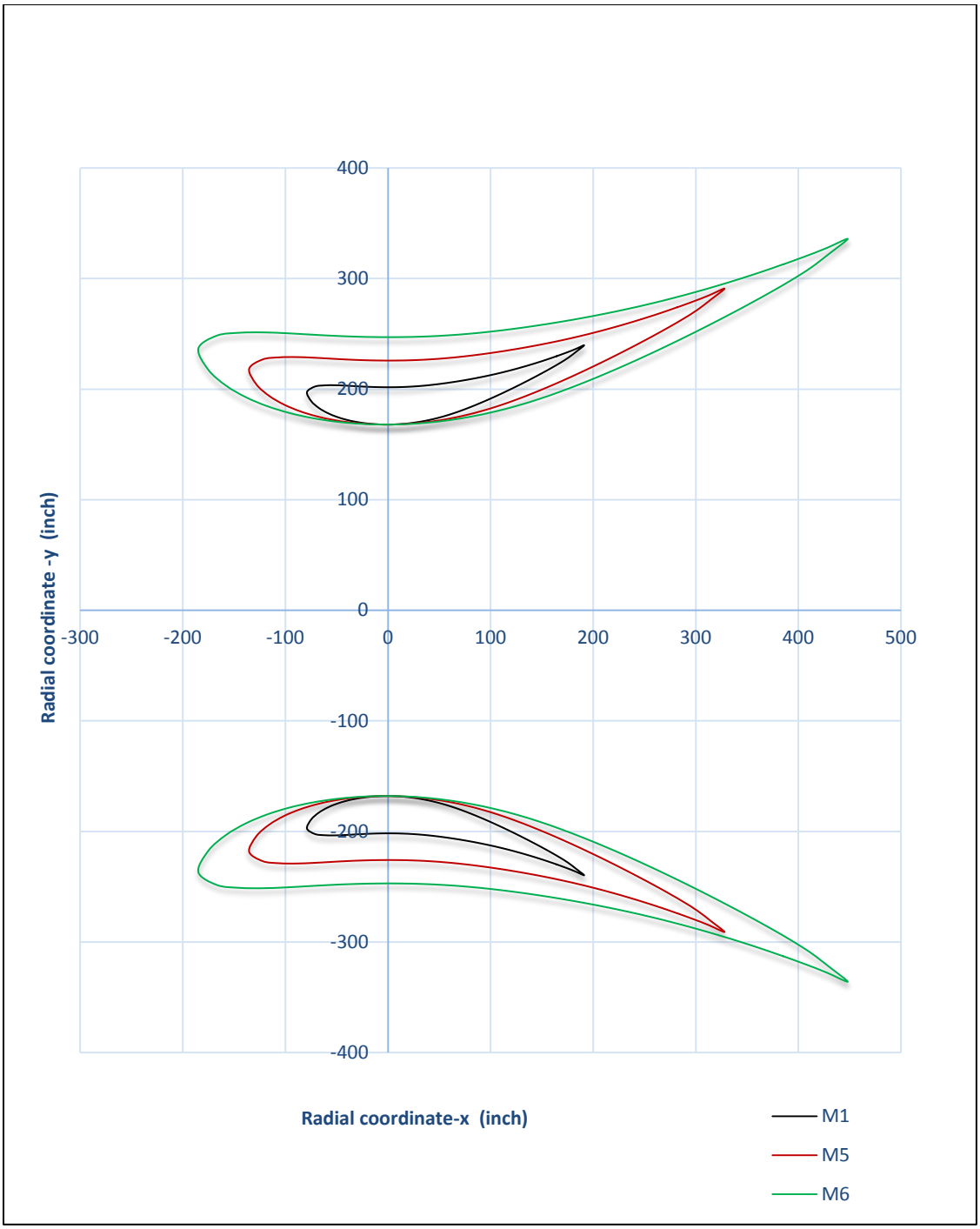

Figure B.6 shroud models (M1, M5, and M6) (changing the shroud length and keeping the angle of attack and throat radius constant)

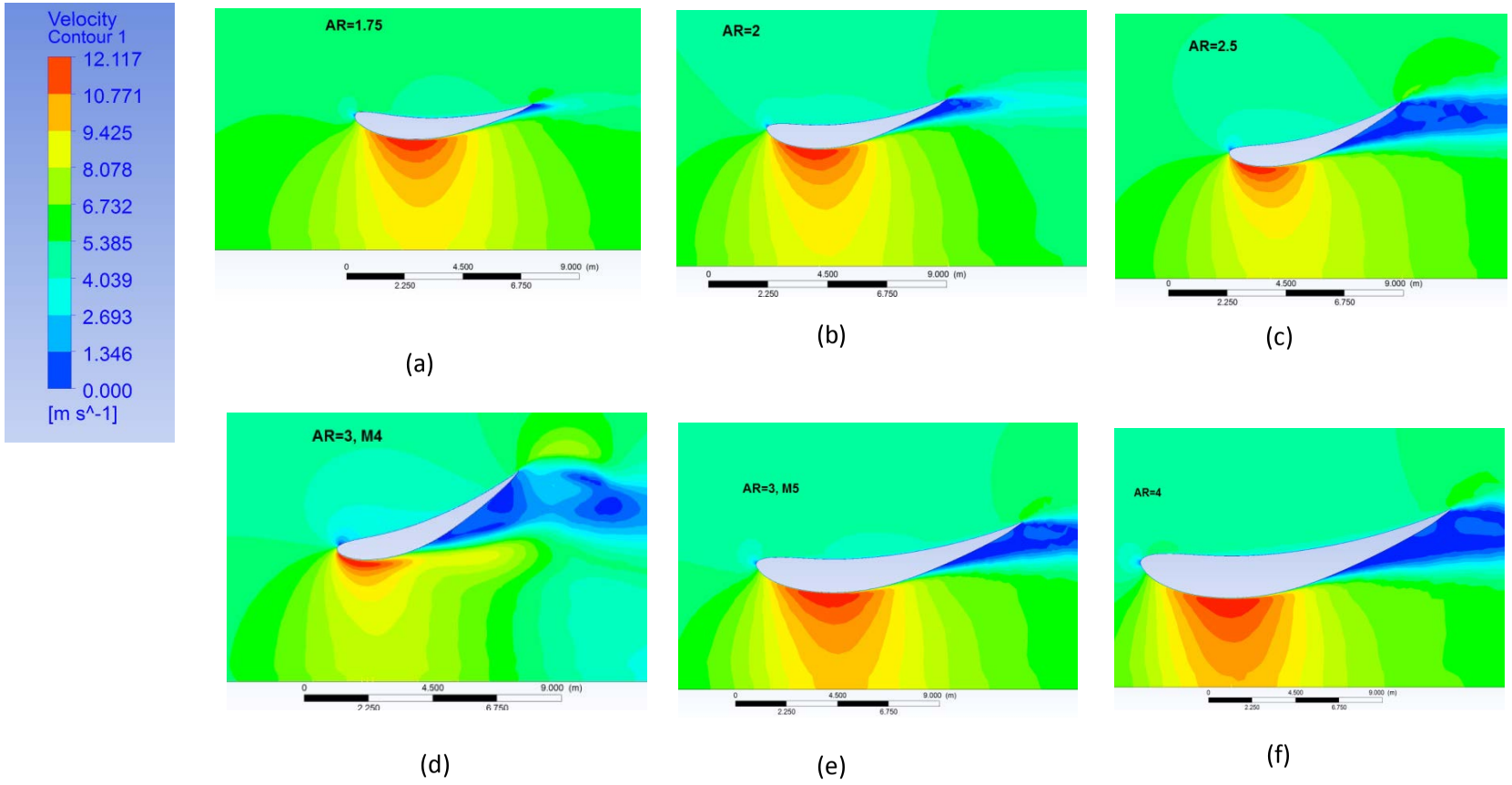

Figure C.7 Velocity contours for the models: (a)M2, Area ratio (AR=1.75), (b) M1,AR=2 , (c) M3,AR=2.5, (d) M4, AR=3, (e) M5, AR=3, (f) M6, AR=4

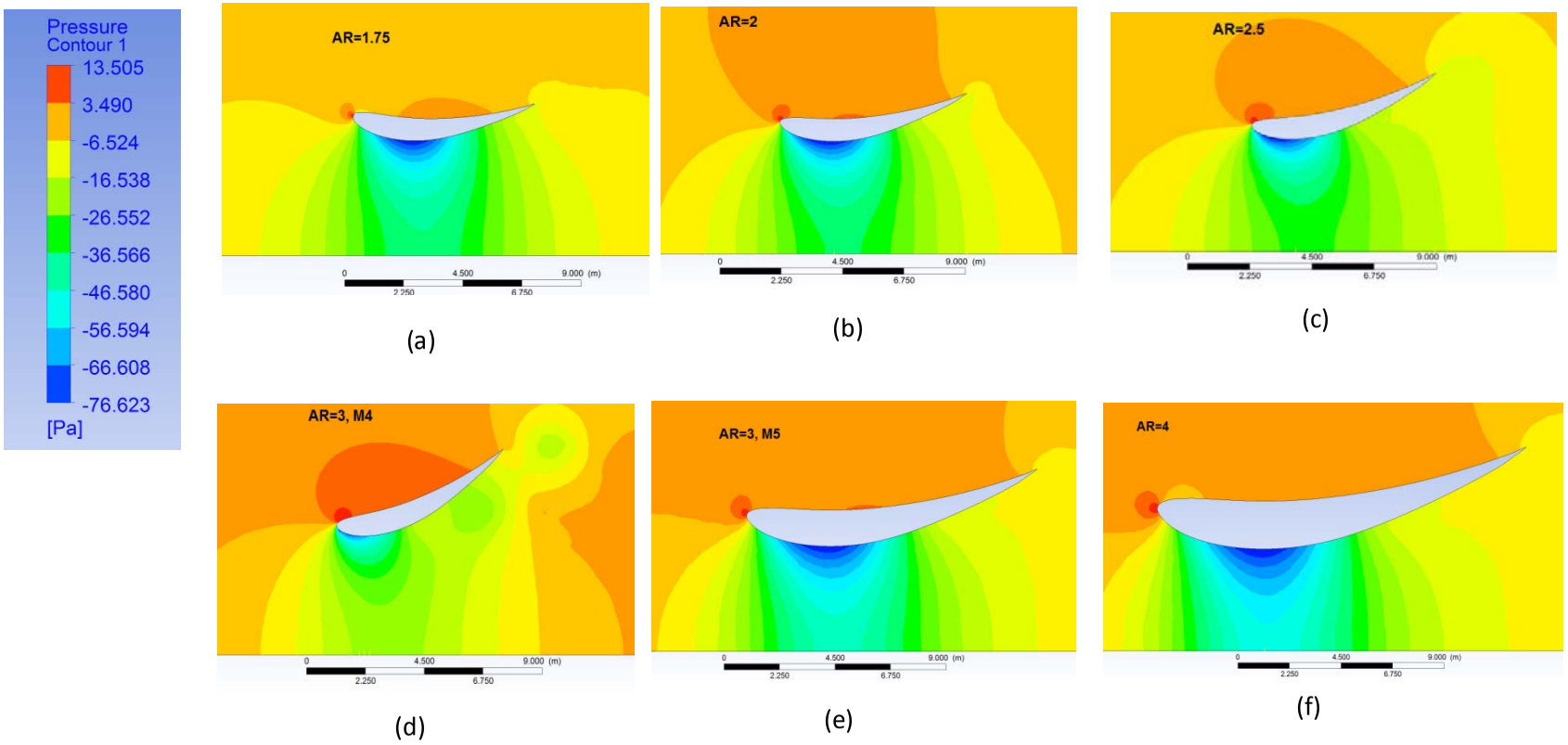

Figure C.8 Pressure contours for the models: (a)M2, Area ratio (AR=1.75), (b) M1,AR=2 , (c) M3,AR=2.5, (d) M4, AR=3, (e) M5, AR=3, (f) M6, AR=4

Appendix D Numerical Analysis Comparison for Grid Convergence

Table D.3 Grid convergence of model M1

			Grid1	Grid2	Grid3
Model M1	Final Gridding	# of Nodes	51584	58432	58705
		# of Elements	100021	113698	114244
		Run Time (min)	22	14.28	18.65
		# of Iterations	2000	1472	2000
	Results Comparison Numerical results	AF0	1.91 (1.57%)	1.9 (1.058%)	1.88
		γ	1.16 (1.301%)	1.13 (1.318%)	1.145
		C_d	0.35 (0.85%)	0.34 (2.05%)	0.347

Table D.4 Grid convergence of model M2

			Grid1	Grid2	Grid3
Model M2	Final Gridding	# of Nodes	51141	52757	69676
		# of Elements	99834	101704	135072
		Run Time (min)	>12	9.1	16.86
		# of Iterations	>2000	1423	1822
	Results Comparison Numerical results	AF0	1.83 (1.09%)	1.82 (1.105%)	1.81
		γ	1.194 (0.33%)	1.1996 (0.803%)	1.194
		C_d	0.235 (8.34%)	0.2319 (%7.115)	0.2154

Table D.5 Grid convergence of model M3

			Grid1	Grid2	Grid3
Model M3	Final Gridding	# of Nodes	48556	51624	58463
		# of Elements	99880	100100	113760
		Run Time (min)	>20	17	>32
		# of Iterations	>2000	1083	>2000
	Results Comparison	AF0	1.785 (0.279%)	1.78 (0.56%)	1.79

	Numerical results	γ	1.06 (1.9%)	1.03 (0.966%)	1.04
		C_d	0.57 (1.59%)	0.5588 (0.392%)	0.561

Table D.6 Grid convergence of model M4

			Grid1	Grid2	Grid3
Model M4	Final Gridding	# of Nodes	63815	67675	73650
		# of Elements	125630	130868	145301
		Run Time (min)	>17	19	>24
		# of Iterations	>2500	2153	>2500
	Results Comparison Numerical results	AF0	1.77 (1.709%)	1.742 (0.114%)	1.74
		γ	0.94 (2.15%)	0.9077 (1.34%)	0.92
		C_d	0.61 (1.154%)	0.6 (0.4988%)	0.603

Table D.7 Grid convergence of model M5

			Grid1	Grid2	Grid3
Model M5	Final Gridding	# of Nodes	59989	71265	75325
		# of Elements	128008	139385	140210
		Run Time (min)	>25	20	>30
		# of Iterations	>2000	2008	>2500
	Results Comparison Numerical results	AF0	2.15 (2.83%)	2.11 (0.95%)	2.09
		γ	1.01 (2%)	1 (1.005%)	0.99
		C_d	0.51 (3.468%)	0.539 (2.06%)	0.528

Table D.8 Grid convergence of model M6

			Grid1	Grid2	Grid3
Model M6	Final Gridding	# of Nodes	69991	73863	77725
		# of Elements	139390	144603	153450
		Run Time (min)	>25	22	>30
		# of Iterations	>2500	2100	>2500
	Results Comparison Numerical results	AF0	2.175 (1.15%)	2.16 (0.46%)	2.15
		γ	0.88 (1.6%)	0.868 (0.23%)	0.866
		C_d	0.6028 (1.85%)	0.5908 (0.152%)	0.5917